



TECHNISCHE
UNIVERSITÄT
WIEN

DISSERTATION

Sub-cycle control of light waves

ausgeführt zum Zwecke der Erlangung des akademischen Grades

eines Doktors der technischen Wissenschaften

unter der Anleitung von

Univ. Prof. Ph. D. Andrius Baltuška

Wien, 27. Juli 2015

am Institut für Photonik der Technischen Universität Wien

Eingereicht an der Technischen Universität Wien

Fakultät für Elektrotechnik und Informationstechnik

von

Mag. Tadas Balčiūnas (1128229)

Wien, Juli 2015

Abstract

Attosecond physics is becoming an established methodology for directly probing the fastest processes in nature. Attosecond optics is enabled by strong field phenomena and relies on ionization and control of electron wave-packets in a very rapidly oscillating optical field. Consequently, strong field ionization is the starting point of all typically studied strong field phenomena, such as above threshold ionization (ATI), coherent and incoherent Xray generation and THz emission from laser plasmas. When a strong periodic driving field suppresses the binding potential of an electron in an atom, molecule or crystal, the electron can tunnel out to become a quasi-free particle within a tiny fraction of the driving optical cycle of the laser pulse twice per optical cycle near the peak of each prominent half cycle. This thesis describes novel tools and methods for controlling the ionization via shaping of the light waveforms on a sub-cycle level. For the measurement of the ionization dynamics optical methods are developed that rely on the detection of secondary radiation emitted in the THz and XUV spectral ranges. As suggested by Brunel two decades ago, the sharp bursts of electrons ejected into the continuum at the peaks of optical half cycles correspond to many orders of optical harmonics of the driver frequency. For a symmetric optical cycle, the ionization bursts of equal strength occur twice per optical cycle leading to the emission of odd-numbered harmonics spaced at twice the driver frequency. By adding a field that is twice or half the frequency of the fundamental field it is possible to break the symmetry of the positive and negative field crests enabling the emission of even harmonics. A particularly interesting is the lowest-frequency emission peak that can be interpreted as a “zeroth” order harmonic sideband corresponding to the THz wave emission. In this thesis a novel scheme is described where incommensurate frequency two-color field can generate temporally modulated electric micro-currents in plasma which allow tuning of the central frequency of the THz sideband.

The Brunel model was initially proposed to explain the high-order harmonic generation (HHG) in the XUV spectral range. However, the key process behind the emission of these very high order harmonics, well above the

ionization potential of an atom, is the recollision with the parent ion. In the so-called simple man's model, the electron ejected into the continuum is accelerated by the laser field and upon its return to the parent ion a high energy photon is emitted. Optimization of HHG is a very active field of research, as it is a promising table-top source of coherent XUV and soft X-Ray radiation packed in extremely short pulses. However the main issue is low generation efficiency. The extremely short time window of this process that takes place within a fraction of half-cycle of the optical field, makes it difficult to control and tailor HHG process. We describe a method for the generation of intense waveforms that allows controlling the electric field on the attosecond time scale and it is based on Fourier synthesis of the light wave composed from several infrared color pulses. These cycle-sculpted waveforms are used for controlling the ionization bursts and subsequent trajectory of the electrons that are emitted in the continuum in a way that they are most efficiently accelerated and return to the ion therefore improving the efficiency of HHG and extending the cut-off toward higher photon energies.

These multi-color waveform shaped pulses allow high degree of control over the HHG process, but it is repetitive and the attosecond pulse emission occurs many times per laser pulse. In order to limit the attosecond XUV bursts to just one per laser pulse and still be able to control the field of the pulse, a single cycle ultrashort pulses are necessary for driving HHG. We describe a novel pulse self-compression scheme that allows 20-fold shortening of pulses in the IR spectral range down to sub-cycle duration. The scheme is based on a Kagome lattice hollow core photonic crystal fiber. Upon nonlinear propagation of the pulse in the fibre due to anomalous dispersion of the waveguide that compensates the positive chirp induced by the self phase modulation, the pulse shortens by itself in a very compact setup and allows high degree of integration into a HHG setup.

The main results presented in this thesis can be summarized as follows:

A concept of multicolor driver pulse synthesis based on spatial and temporal superposition of waves from an optical parametric amplifier is proposed and demonstrated. Both the absolute (CEP) and relative phase of the constituent pulses at every carrier frequency is controlled. To this end, both an active phase-locking of the femtosecond pump laser and the passive phase lock resulting from the operation of a white-light-seeded OPA are employed.

Continuous tunability of THz emission from a two-color-driven laser plasma is theoretically predicted and experimentally verified by means of a CEP-locked parametric generator of two incommensurate optical driver frequencies.

A unified view on the generation of low-order sideband (THz emission) and higher-order optical sidebands (low-order harmonics emission) from a

laser-driven plasma is developed based on a fully quantum-mechanical description of continuum-continuum transitions for ionized electrons as an extension of the earlier semi-classical Brunel model.

Active CEP stabilization is realized for the first time on a multi-millijoule femtosecond Yb-doped amplifier. A new forward CEP stabilization technique is proposed and demonstrated on a multi-kHz repetition-rate Yb-doped amplifier.

A possibility to optimize the HHG average spectral brightness and extend the spectral cut-off by means of engineering the electron trajectory in a multicolor-shaped optical cycle of a linearly-polarized driver pulse has been demonstrated experimentally and confirmed theoretically. Substantial increase of the peak intensity of the corresponding attosecond XUV bursts in the time domain is predicted.

An efficiency and bandwidth improving concept for femtosecond OPA driving with shaped femtosecond Yb-pulses is proposed and demonstrated. Based on the phase-only pulse shaping, the technique yields a chirped top-hat pulse for OPA pumping while enabling, simultaneously, a fully compressed pulse required for efficient generation of the white-light seed for the OPA.

Generation of externally and self-compressed pulses from a novel type of a gas-filled hollow waveguide – a Kagome-lattice photonic-crystal fiber – was explored as a means of increasing the pulse intensity and reducing the number of optical cycles of the driver laser. A sub-single-cycle transient was generated at the wavelength of $1.7 \mu\text{m}$, which enabled XUV emission in a single isolated attosecond burst regime as evidenced by the observation of a continuous XUV spectrum free of harmonic modulation.

Contents

1	Introduction	1
1.1	Outline of the thesis	1
1.2	Introduction	2
1.2.1	Strong-field ionization	3
1.3	Scope of this thesis	4
2	Optical and electron detection of ionization	8
2.1	Introduction	8
2.1.1	Semiclassical model of electron emission and sideband generation in a two-color field	10
2.1.2	Quantum mechanical treatment of Brunel emission	11
2.2	THz sideband generation from gas	12
2.3	Mapping of electric current with ATI spectroscopy	13
2.4	Summary	16
3	High-order harmonic generation with cycle-sculpted pulses	17
3.1	Introduction	17
3.2	Experimental setup	21
3.3	Results	22
3.4	Summary	23
4	Carrier-envelope phase control of laser pulses	26
4.1	Stabilization of the Yb:KGW amplifier	26
4.2	Direct amplifier stabilization	32
4.2.1	Feed-back scheme for direct amplifier stabilization	39
4.3	Summary	41
5	Improving parametric amplifier efficiency via pulse shaping	42
5.1	Experimental setup	44
5.2	Results	44
5.3	Pulse recompression for seed generation	47

5.4	Summary and Outlook	48
6	Frequency tunable THz emission from laser-driven plasma	49
6.1	Introduction	49
6.2	Quantum mechanical transient electron-current model for THz emission	51
6.3	Experimental implementation	57
6.3.1	Observation of directional electron current	58
6.3.2	CEP-locked, tunable THz emission	58
6.4	Summary	62
7	Pulse post-compression using Kagome lattice fibres	63
7.1	Nonlinear propagation calculation	64
7.1.1	Waveguide dispersion of the Kagome fibre	65
7.1.2	Short fibre case	65
7.1.3	Long fibre case	67
7.2	Experimental results	69
7.2.1	Spectral broadening results in Argon	70
7.2.2	Spectral broadening results in Krypton	73
7.3	Solitonic self-compression	76
7.4	Summary	77
8	Sub-Cycle Gigawatt Peak Power Pulses Self-Compressed by Optical Shock Waves	78
8.1	Experimental setup	85
8.2	Pulse propagation dynamics	91
8.3	Numerical simulation of nonlinear pulse propagation	92
8.4	Characterization of the self-compressed pulses with stereo-ATI electron spectrometry	96
8.5	Optimization of self-compression and energy scalability	98
8.6	Configurations of the strong-field source	100
8.7	Fibre properties	102
8.8	An integrated self-compression and XUV-generation scheme	103
8.9	Spectral broadening in a positive dispersion regime	108
8.10	Summary	111
	List of Publications	112
	Abbreviations	118
	Bibliography	118

Chapter 1

Introduction

1.1 Outline of the thesis

The thesis consists of eight chapters that describe mainly experimental work on ultrashort pulse generation in a wide range of electromagnetic radiation spectrum ranging from very low frequency THz pulses up to XUV pulse trains generated via High order Harmonic Generation (HHG). A key element behind these experiments is the source that can generate intense waveforms synthesized from several infrared femtosecond pulses. A substantial effort was dedicated to the development of such a source, various aspects of which are detailed in this thesis. The thesis is organized as follows. First chapter serves as a basic introduction to the main processes in high field physics and describes one particular experiment that was done as part of this thesis. One of the key parts of the work is the demonstration of waveform shaping on the sub-cycle time scale. The intense (reaching 10^{14} W/cm²) waveforms were applied for driving THz generation in the ionizing regime and coherent control of electron trajectories in HHG. All the experiments are based on two underlying laser technologies: carrier envelope phase (CEP) control of the pulses and optical parametric amplification (OPA). The work presented in this thesis describes several new schemes for efficient CEP control of high power Yb based laser systems and improvements of OPAs by a novel rectangular pulse shaping scheme. The concept of sub-cycle control of the light fields is extended to THz spectral range allowing the generation of tunable frequency THz emission in plasma driven by incommensurate frequency fields. Finally the generation of very short light transients in a specialty photonic crystal fiber (PCF) down to less than a cycle of a period of the light oscillation is described.

1.2 Introduction

Advances in ultrafast laser technology allowed generation of pulses with intensities that reach electric field strengths comparable to the Coulomb field in atoms. Because the field occurs twice per optical cycle and response of matter to such intensities is extremely fast and nonlinear with respect to the instantaneous field strength, direct observation of attosecond dynamics became possible, giving rise to the new research field of attophysics [1]. An electric field competing in its strength with binding forces can significantly modify the binding potential seen by outer valence electrons, allowing their release into the continuum. Liberation of an electron by the laser field from its bound state is the primary step in strong field – matter interaction [2]. Tunnel ionization and subsequent acceleration of the liberated electron lead to prominent phenomena like above threshold ionization (ATI) [3] or THz field generation [4]. Some trajectories allow the electron to return to the parent ion where it can recombine to the ground state emitting high energy photons, the process known as high order harmonic generation (HHG) [5].

Traditionally, the required field strengths are achieved by using ultrashort laser pulses with a sinusoidal carrier wave. The shape of the waveform determines the instances of ionization and the trajectories of released electron. For a sinusoidal carrier wave, this dependence famously results in the $3.17 U_p$ maximum kinetic energy of a rescattered electron being converted into the highest HHG photon energy [5, 6] as a direct consequence of controlling a returning electron wave packet trajectory with a harmonically oscillating electric field.

The highest peak power of an ultrashort laser pulse is achieved through pulse compression, i.e. elimination of group delay for all colors comprising the pulse [7]. Field evolution control, performed either through tailoring the pulse envelope or through shaping the optical cycles, provides access to changing the outcome of complex strong field matter interactions. Control on the femtosecond time scale can be achieved by tuning the envelope of the driving laser pulse [8]. Control on the attosecond, or, sub-cycle time scale requires shaping the optical cycle of the carrier wave. Basic field shaping methods, without mentioning polarization coding methods are the chirping of the carrier wave [9], control of its phase under a few-cycle envelope [10], or coherent addition of low-order harmonics [11]. The latter method corresponds to Fourier synthesis of an optical waveform. The capacity of the lower harmonic superposition method, a steep decrease in the generation efficiency and the fact that harmonics quickly reach the UV region which is undesirable for driving strong field phenomena. An important improvement of this multicolor method will be to efficiently generate Fourier components

down-converted rather than upconverted from the laser frequency. Optical parametric amplification [12, 13] is an efficient and well-developed technology to realize such synthesis.

In this thesis multi-color sub-cycle shaping of intense laser fields is described that allows direct control of strong-field dynamics. Firstly, the tunnel ionization is reviewed which is the initial step behind most of the strong field processes and attosecond dynamics [14]. The direct observation of the ionization is shown to be possible using optical and THz range detection schemes. The final part of this chapter describes the control of the trajectories of the ionized electrons for tailoring HHG which is applied for improving the efficiency and extending the cut-off of the generated XUV radiation.

1.2.1 Strong-field ionization

The ionization rate and timing can be controlled via sub-cycle shaping of the waveform. As suggested by Keldysh in his theoretical work [2], a valence electron can tunnel through the binding potential barrier, modified by a strong laser field. Since the probability of ionization reaches its maximum near the peaks of the electric field, ionization is predicted to be confined to short intervals of time, lasting a fraction of a half cycle of the light field oscillation. Typically, the tunneling ionization (TI) regime is defined to occur when the Keldysh parameter

$$\gamma = \frac{\omega_L \sqrt{2m_e I_p}}{|q_e| E_0} \quad (1.1)$$

is much less than unity $\gamma \ll 1$ (ω_L – laser carrier frequency, E_0 – amplitude of the electric component of the light field, I_p – ionization potential of an atom, m_e and q_e – electron mass and charge respectively). Corrections due to Coulomb effects that are neglected in the original theory of Keldysh were introduced by Perlemov et al. in the so-called PPT model [15, 16]. In the limit when γ approaches zero, the PPT model corresponds to tunneling through a static barrier described by ADK model [17]. Yudin and Ivanov suggested that tunneling remains significant even for γ greater than one [18]. More recently the sub-cycle ionization theory was later extended to solids [19]. The case, when $\gamma \approx 1$ corresponds to the non-adiabatic tunneling regime. Since in this regime the corresponding tunneling time is on the order of the optical half-cycle, the binding potential formed by the atomic field and oscillating laser field varies during tunneling in this regime. In the regime of TI, the probability of ionization is extremely sensitive to the amplitude of the electric field since only a sufficiently strong field can cause substantial

modification of the binding atomic potential. Consequently, the ionization rate becomes strongly sensitive to the absolute phase of the light pulse, which leads to the expectation that the ionization yield reveals a step-wise profile on a sub-femtosecond time scale where each step is locked to a half-cycle of the laser field. Such a behavior of the ionization yield has been recently visualized in an elegant time-of-flight spectrometry measurement [20] where the attosecond steps in the ion yield were detected using an isolated soft X-ray attosecond pump pulse and a few-cycle optical probe. It also demonstrates that the tunneling regime of ionization remains significant even at γ values greater than unity (as it was predicted in [18]) since $\gamma \approx 3$ was used in the experiment.

1.3 Scope of this thesis

The main motivation of this thesis is the control the light waves on the time scale of a fraction of a cycle. In general, atoms, molecules and solids can be ionized in many different ways and the ionization process can vary greatly on the time scale. For example, laser induced optical breakdown can take place on the time scale of nanoseconds (10^{-9} s) in case of long laser pulses [21]. Such ionization has been extensively studied since the advent of a laser, however, the mechanism behind it is hardly controllable due to probabilistic nature of avalanche ionization. This thesis is focused on controlling motion of electrons in atomic and molecular systems - some of the fastest processes in physics. Unlike in perturbative nonlinear optics where dynamics are driven by the envelope of femtosecond pulses, strong-field physics and attosecond optics rely on ionization and charged particle control in the continuum driven by the optical field oscillating at PHz frequency. Novel tools, sources and methods that allow studying dynamics taking place on a sub-cycle time scale are required in order to study and control these ultrafast processes. Shaping of the optical single cycle pulse within a contiguous bandwidth spanning more than an octave is very challenging. We adopted a Fourier synthesis approach for synthesizing an intense optical waveform with highly controllable shape of the field on a very short time scale.

Firstly, ionization detection using optical and electron methods is introduced in chapter 2. This involves detection of new frequencies due to TI induced stepwise increase of electron density and directional electron current. A more sophisticated scheme based on high order harmonic generation described in chapter 3 allows probing the electron wavepacket upon its recollision with the parent ion and provides additional information about the kinetic energy of the EWP which can be mapped onto the emitted high order

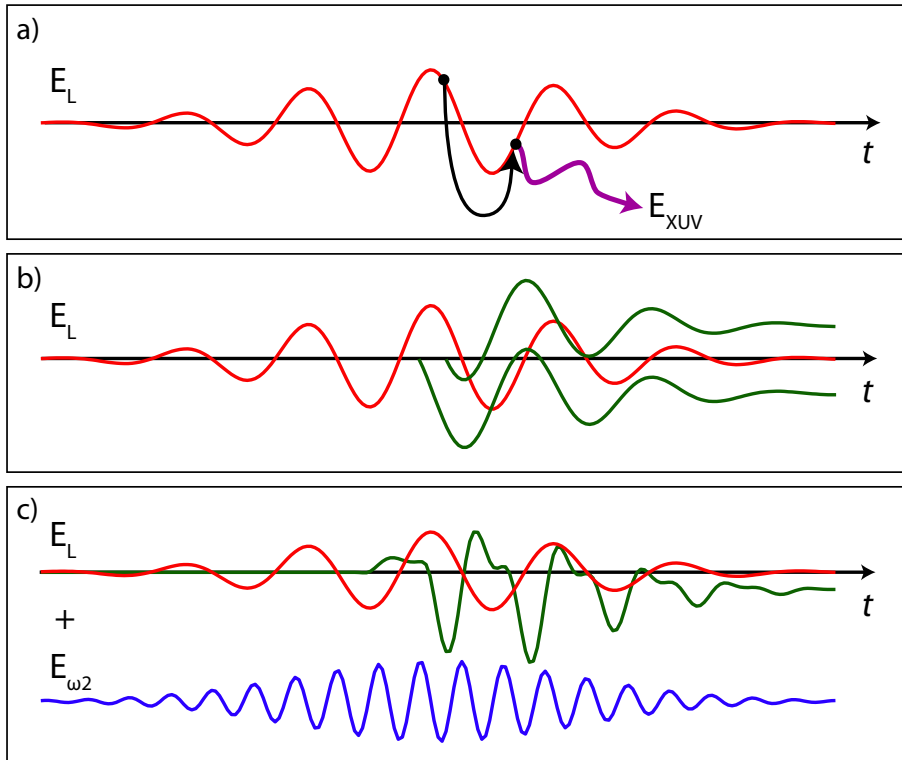


Figure 1.1: An illustration of ionization in a strong laser field that can be viewed as tunneling through a barrier formed by the addition of potential slope caused the laser electric field (shown as the red curves) and the atom's Coulomb potential. After ionization, the motion of the freed electron (black line denotes electron trajectory in panel (a)) is forced by the laser's electric field, and thus the freed electron can come back to its parent ion with a high kinetic energy and recombine. Upon recombination a high energetic photon (shown as the purple arrow) is emitted (a). However, the recombination probability is low, and thus most freed electrons remain in the continuum and gain energy until the laser pulse has passed (b). Non-returning electron trajectories are shown as green lines in panels (b) and (c). Generally, the electron emission is symmetric with respect to the laser polarization direction. This symmetry can be broken by adding a second laser field with an appropriately chosen different color and phase (shown as blue line in panel (c)). The asymmetric electron emission can give rise to emission of a strong low-frequency (THz) pulse.

harmonic spectrum.

Since TI is sensitive to the field and not just intensity of the light field, these ionization and motion control methods require precise control of the electric field shape. In order to produce waveforms reproducible from one laser pulse to another, it is necessary to stabilize the CE phase of these pulses. Chapter 4 describes CEP stabilization of Yb laser systems. The Yb laser technology has attracted a lot of attention due to capacity to generate ultrashort pulses at high average power [22, 23]. This is a promising route toward development of high flux table-top XUV sources. In order to generate high order harmonics in the soft X-ray spectral range, one has to use longer wavelength pulses for driving HHG. Longer wavelength field allows more time for the electron to be accelerated and yields to higher kinetic energy upon recollision E_{max} which scales quadratically with the driving laser cycle period $E_{max} \propto \lambda^2$. Scaling of the driving laser field wavelength has been successfully used for pushing the cut-off toward high photon energies [24, 25], however, this comes at an expense of a severe drop in efficiency of the single atom. In chapter 3 a novel scheme is explored based on precise multi-color waveform synthesis, where the electron trajectory is manipulated in such a way that yields higher cut-off of the emitted high order harmonics without the loss of efficiency. On the contrary, unlike the single color driven HHG, in the multi-color optimized field case the efficiency is improved, because most of the electrons emitted at the peak of the field correspond to trajectories that return to the ion and produce useful emission in the form of high order harmonics. The generation of these multi-color waveform transients in the IR spectral range relies on the nonlinear frequency conversion and parametric amplification of light pulses. Parametric amplification of ultrashort pulses is a very powerful technique, however, it comes at a price of limited conversion efficiency. Chapter 5 describes a method for improving the conversion efficiency of the OPA via pulse shaping and production of temporally rectangular pulses for pumping of a parametric amplifier. Combined with the high power Yb laser technology this is a step toward improving the photon flux of HHG based XUV sources.

The multi-cycle repetitive waveforms allow studying sub-cycle dynamics and recovering the recolliding EWP or controlling the direction of the current induced directional current which yields THz emission. However, for studying processes that are longer than the cycle of the field, an isolated attosecond pulse is required. Production of these pulses relies on pulse post-compression. One novel scheme for the generation of sub-cycle pulses is described in chapter 8. It is based on pulse self-compression in a hollow core photonic crystal fiber. The key ingredient in this pulse compression scheme is Kagome lattice fibre that has optimal dispersion profile in the anomalous

dispersion regime and supports bandwidth spanning over one octave. Firstly, optimization of Yb laser amplifier pulse spectrum broadening in the positive dispersion regime in such fiber is presented chapter 7. Pulse post-compression in hollow core capillaries [26] in the positive dispersion regime is routinely used for the generation of few-cycle pulses. However, it requires compensation of chirp which is difficult to achieve over very wide bandwidth. Pulse self-compression in the anomalous dispersion regime is explored in chapter 8. In this case the positive chirp due to self-phase modulation is compensated by the anomalous dispersion of the waveguide and yields pulse that shortens by itself while propagating through the waveguide. We confirmed that this scheme is capable of producing pulses with sufficient peak power by demonstrating ATI electron steering and HHG experiments using these pulses.

Chapter 2

Optical and electron detection of ionization

2.1 Introduction

The direct observation of the ionization in gaseous media by few-cycle pulses was performed in [20] by means of a time-of-flight measurement. This method is currently successfully used in attosecond physics [27, 28] for investigation of different intra-atomic and intra-molecular process in gases [29] and solid surfaces [30]. This technique implies the detection of charged particles (electrons or ions) that have escaped from the interaction volume and is applicable for gaseous media or solid surfaces. However, it cannot be used for investigation of ionization processes in volume of bulk materials. Therefore, for such materials another method which is not based on direct detection of ionization products has to be developed.

Recently, an all-optical approach for investigation of ionization dynamics in transparent media has been devised, which is based on the detection of a time-resolved optical signal which uniquely originates from the electron tunneling [31]. This method utilizes a non-collinear optical pump-probe scheme, where ionization dynamics created by a few-cycle pump pulse is read out by a probe pulse in the form of new spectral components. The non-collinear pump-probe scheme allows discriminating between the delay-dependent signal in the direction of the probe pulse, originating from ionization, and all possible signals generated through the nonlinear response of the medium. From the nature of TI, one can obviously expect that new frequencies are generated spaced by twice the optical frequency of the ionizing field. This behavior was first proposed by F. Brunel in 1990 [32], as a mechanism to explain high harmonic generation (HHG). Although later it was shown by

P. Corkum [5] that HHG is better explained by recombination of accelerated electrons after TI (see also Figure 1.1), investigation of harmonic generation following the mechanism proposed by Brunel can offer more insights in the dynamics of TI in the adiabatic regime.

In the pump-probe scheme, it is not required that the pump and probe fields have the same frequency. Thus one may expect that the ionization profile read out by the probe field gives rise to sidebands separated by twice the optical frequency of the pump field with respect to the frequency of the probe field: $\omega_{sb} = \omega_{pr} \pm N \cdot 2\omega_p$, where N is an integer number. When the polarization of the probe field is the same as the polarization of the pump field, and the fields propagate together in the same direction, the modulation on the pump field caused by the probe causes a modulation of the ionization rate, which results in the generation of even more frequencies. The implications of this insight are reviewed in Figure 2.1.

In this chapter, experimental results are presented on the detection of ionization via measurement of optical signals induced by TI in different frequency ranges, and a theoretical model of the generation of new optical frequencies in media ionized by a high-intensity laser field. Firstly, a semi-classical framework is introduced that describes TI in a multicolor laser field and a quantum mechanical interpretation. Several experiments supporting our model are presented. The scheme consists of two pulses, one relatively strong (pump) and an additional weaker field (probe). When the probe beam has the same polarization as the pump, and has a frequency close to half the pump frequency, TI can be suppressed at every other half-cycle, similarly to when the probe frequency is close to the pump second harmonic. In such a case, a sideband close to zero frequency can be observed from gaseous media in the adiabatic TI regime [33]. Such a scheme offers great prospects for broadband and high peak amplitude THz-pulse generation. Here it is shown that the frequency of the THz sideband can be continuously tuned by tuning the frequency ratio of the two color field. More in-depth discussion on frequency tunability of THz pulses generated in plasma is provided in chapter 6. Our experimental observations are in good agreement with calculations of the optical response from the ionized medium using semiclassical two-step model. Finally, we show that the directional current in gases induced by incommensurate frequency fields can be directly detected using a so-called stereo-ATI electron spectrometer [34, 35, 36]. A classical description of the electron current following TI in a multi-color laser field can at the same time accurately describe the electron kinetic energy spectrum, and the generation of new frequencies from an ionized medium. We also show that the low energy electron spectrum may be used for a more robust carrier-envelope phase detection scheme, since the electron yield at low kinetic energies is orders of

magnitude higher than at high kinetic energies.

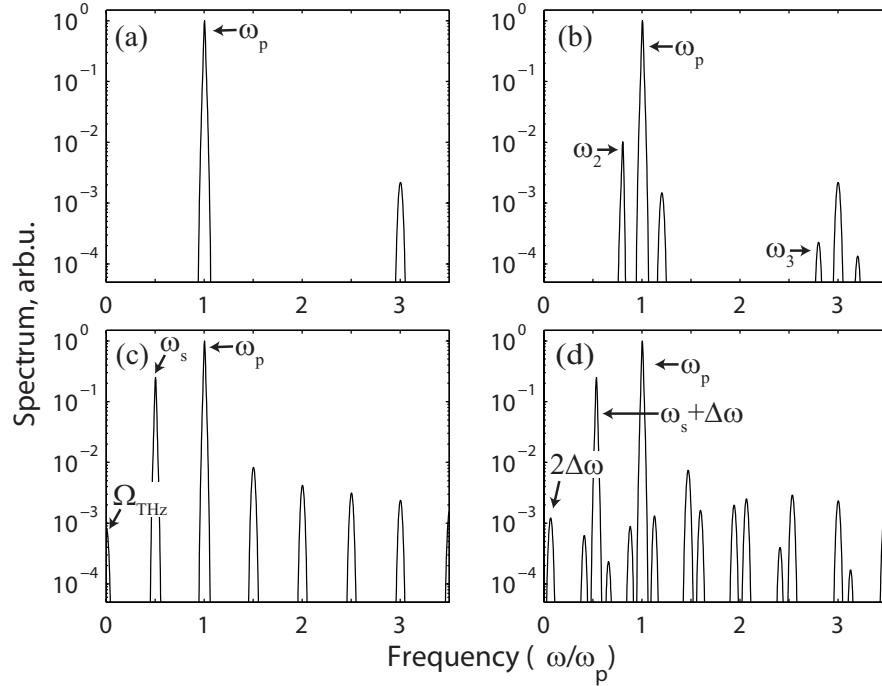


Figure 2.1: Sideband generation due to tunnel ionization effects. In a monochromatic laser field, due to tunnel ionization, odd-order harmonics are generated (a). When a weak second laser field is added with a slightly different frequency, sidebands spaced by twice the stronger laser field’s frequency are generated relative to the weak field’s frequency as well (b). When the weak laser field’s frequency is equal to half the frequency of the strong field, the tunnel ionization is enhanced every other half-cycle of the strong field. The induced asymmetric emission gives rise to sidebands spaced by exactly once the frequency of the strong field, and thus a field with almost zero frequency, i.e. THz emission can be observed as well (c). By tuning the weak field’s frequency away from $1/2$ the strong field frequency by $\Delta\omega$, the frequency of the generated THz sideband is shifted by $2\Delta\omega$ (d).

2.1.1 Semiclassical model of electron emission and sideband generation in a two-color field

The semiclassical model of Brunel harmonic emission [32] provides an intuitive description of the mechanism of the process. It is based on microscopic electron current production in a field. Brunel proposed a model initially

aiming to explain high order harmonic generation. More recently it was shown that the superposition of two colors, namely fundamental frequency and the second harmonic of the laser field, induces a directional current and the model is used to explain the strong THz pulse emission in plasma [37]. In the high-intensity regime, the ionization of atoms or molecules can be described as a tunneling of an electron through the barrier into the continuum. Quantitatively this is calculated using the ADK tunneling rate formula [17]. After the electron is released into a continuum, it is treated as a classical particle and is accelerated in a laser field. The velocity of an electron in a laser field $E(t)$ is given by

$$v(t) = \frac{q_e}{m_e} \int_{t_0}^t E(t') dt'. \quad (2.1)$$

The resulting laser-field induced electron current density is then calculated by integrating:

$$J(t) = \frac{q_e^2 \rho}{m_e} \int_{-\infty}^t dt_i \Gamma(t_i) \int_{t_i}^t dt' E(t'), \quad (2.2)$$

where Γ is the tunneling rate, ρ is the density of gas, q_e and m_e are the charge and mass of an electron. The emission of electromagnetic field is related to the acceleration of the charge and is therefore proportional to the derivative of the induced current density $J(t)$:

$$E_{THz} \propto \frac{dJ(t)}{dt}. \quad (2.3)$$

2.1.2 Quantum mechanical treatment of Brunel emission

The classical interpretation of the emission by the induced electron current although intuitive, is not rigorous and does have serious limitations. On the other hand full ab initio numerical integration of time-dependent Schrödinger equation was performed to calculate THz emission [38, 39] and shows a good agreement with the experimental data. Initial steps were done to apply a strong field approximation for the calculation of the THz emission using analytical quantum mechanical model [39]. Here we show that there is a bridge between the classical model of the emission due to strong field ionization and charge motion in the laser field and the free-free transitions in the quantum mechanical interpretation. The semiclassical treatment by Brunel is based on several approximations. First, only the interaction of the free electron with the laser field is considered, the Coulomb potential of the core is neglected.

The model describes the electromagnetic wave emission that arises from the current J induced by the laser field. The emitted electric field is proportional to the derivative which is can be expressed as a product of the ionization rate and the laser field:

$$\dot{J} \propto E_L(t) \cdot n(t), \quad (2.4)$$

where $E_L(t)$ is the laser electric field and is the time-dependent electron density. In the limit of small depletion and strong field regime the free electron density can be expressed as $n(t) = N \int^t \Gamma(t') dt'$, where N is the density of the atoms or molecules and $\Gamma(t)$ is the static ionization rate. From the quantum mechanical perspective, the induced dipole moment is:

$$d(t) = \langle \psi(t) | \hat{d}(t) | \psi(t) \rangle. \quad (2.5)$$

The wavefunction of the whole system can be separated into continuum and bound wavepacket parts $\psi = \psi_b + \psi_c$. Similar to the semiclassical model, let us consider only the free electrons and replace the full wavefunction with the continuum wavepacket ψ_c . The derivative of the current is associated with the second derivative of the dipole moment:

$$\ddot{d}(t) = \langle \psi_c(t) | F_{total} | \psi_c(t) \rangle, \quad (2.6)$$

where F_{total} is the total field acting on the electron wavepacket, which can be separated into two parts: $F_{total} = F_L + F_{core}$. The first term corresponds to the force acting on the electron by laser field and the second term is the force due to interaction with the core. By neglecting the latter term, the dipole acceleration becomes:

$$\ddot{d}(t) = F_L \langle \psi_c(t) | \psi_c(t) \rangle. \quad (2.7)$$

The right hand side of the equation is just a probability of ionization times the force of the laser field $F_L W_c(t)$. Since $n(t) \approx N W_c(t)$, we see that the expression (2.7) is essentially the same as the derivative of the electron current (2.4) in the semi-classical treatment, which means that the emission mechanism proposed by Brunel arises due to continuum-continuum transitions.

2.2 THz sideband generation from gas

The same ideas that were demonstrated for the odd-harmonic generation experiments in solids and gases [31, 40] can be seamlessly extended to explain the emission of low-frequency sidebands in the THz range. In fact, the

process can be treated as a special case of wavemixing based on transient nonlinearities and as suggested in Ref. [41] can lead to the emission of THz “Brunel sidebands”. Mixing the fundamental field with its second harmonic breaks the symmetry of the cycle and yields to the emission of even harmonics in addition to the odd harmonics. In addition to even high order harmonic generation, this was exploited for the generation of THz pulses in plasma by Cook and Hochstrasser [42]. There exist several interpretations of the process. Originally, the emission of the strong THz transients was attributed to a four wave mixing in air. Later, however, it was shown that the THz emission directly relies on the production of laser induced plasma [33]. In a semi-classical two-step model, the second color acts as an “AC bias” by breaking the symmetry of the optical cycle and yields production of directional electron current. This directional electron burst was directly observed by means of ATI spectroscopy [43]. This THz generation scheme serves not only as a tool for studying of ionization processes, but also as a practical tunable frequency THz source described in details in chapter 6.

2.3 Mapping of electric current with ATI spectroscopy

In addition to the optical detection described in the previous sections, the directional current induced by asymmetric field composed of incommensurate frequencies was also measured directly using electron spectrometry. Combination of several colors provides additional knobs to control the dynamics of sub-cycle ionization. This approach was successfully applied, for example, for the measurement of electron birth time in the HHG process [44] and isolated attosecond pulse generation [11, 45]. Here this approach was extended where incommensurate frequency infrared colors are combined to control the timing and the trajectory of the electron in a continuum.

In this section stereo-ATI electron spectroscopy measurements in xenon using intense two-color laser pulses are presented. A two color beam that is composed of a strong 1030 nm and a weaker 1545 nm signal wave is focused into a xenon gas cell. This incommensurate frequency field superposition yields asymmetric electric field. Since the horizontal polarization was used in the experiments, we denote the positive and negative directions of the E field and the resulting electron drift directions as “left” and “right”. The intensity of approximately 0.6×10^{14} W/cm² is reached in the focus which corresponds to the regime where TI is a dominant process ($\gamma \approx 0.8$). In the strong field regime the electron wave packet evolution in the continuum is

mainly determined by the shape of the laser field and the Coulomb interaction with the parent ion can be neglected.

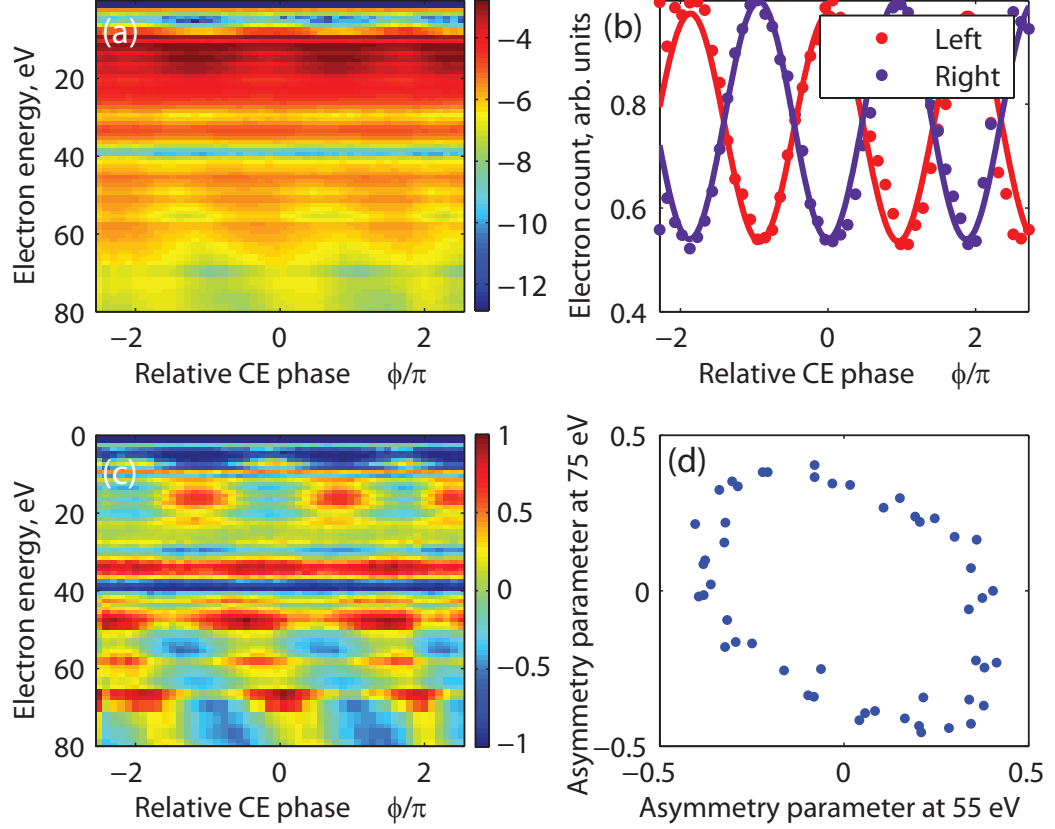


Figure 2.2: A stereo-ATI electron spectrum measurement. a) phase dependent spectrum of the electrons emitted to the right, b) lineout at 15 eV of the left and right energy spectra for different CEP phases, c) measured asymmetry parameter dependence on CE phase and electron energy, d) CEP phase ellipse obtained from asymmetry parameters at 55 and 75 eV energy.

The superposition of two colors leads to beating of the electric field and can be treated as a train of few-cycle pulses with a DC offset (if the amplitudes of the two fields are not equal) as illustrated in Figure 2.3. The beat period determines the envelope of these few-cycle pulses. In case of equal amplitudes of two colors $E_1 = f(t) \sin(\omega_1 t + \varphi_{\text{cep}})$ and $E_2 = f(t) \sin(\omega_2 t + \varphi_{\text{cep}} + \varphi_{\text{rel}})$ under a laser pulse envelope $f(t)$, the resulting field is:

$$E = f(t) 2 \sin\left(\frac{\omega_1 + \omega_2}{2} t + \varphi_{\text{cep}} + \frac{\varphi_{\text{rel}}}{2}\right) \cos\left(\frac{\omega_1 - \omega_2}{2} t - \frac{\varphi_{\text{rel}}}{2}\right). \quad (2.8)$$

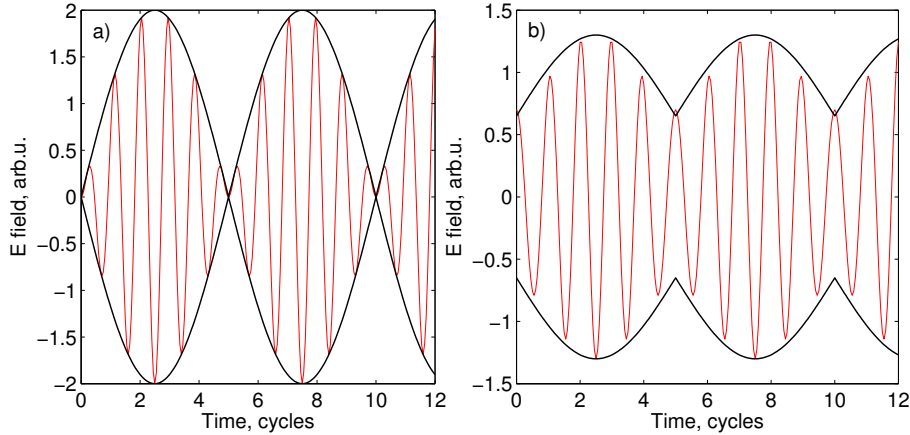


Figure 2.3: An illustration of two-frequency beating described by (2.8) a) in case of two equal amplitude fields and b) in case when the second field amplitude is only 30% (10% intensity). For clarity 20% frequency difference between the two fields was chosen.

In the case of combination of pulses with a wavelength of 1030 nm and 1545 nm, the synthesized field can be considered as a train of pulses with the corresponding carrier wavelength $\lambda = 4\pi c/(\omega_1 + \omega_2) = 1.2 \mu\text{m}$ and separated by $T = 2\pi/(\omega_1 - \omega_2) = 10$ fs in time.

The experimental results are summarized in Figure 2.2. The electron spectrum and a lineout at 15 eV shown in panels a) and b) are highly dependent on the CEP of the laser pulse. The electron asymmetry modulation depth at 15 eV exceeds 50%, which indicates good reproducibility of the generated waveforms. The calculated asymmetry map depicted in Figure 2.2 c) shows the value of the normalized asymmetry parameter $a = (L - R)/(L + R)$ versus energy and CEP of the laser pulse. From this data the phase ellipse is obtained by taking lineouts at two different energy windows [34, 36], which can be used for in-situ calibration of the actual produced waveform.

Usually for the measurement of the CEP value the high energy part of the spectrum corresponding to rescattered electrons is used. The low energy part of the spectrum which is dominated by direct electrons, is also sensitive to the CEP of the pulse. Here it is demonstrated that the CEP can be measured in-situ not only from the high energy part of the electron spectrum, but also the low energy direct electrons can be used to retrieve the CEP without π -ambiguity. From the experimental data in Figure 2.4 a low energy window can be observed where the phase of the retrieved asymmetry varies with electron energy allowing CEP retrieval without π ambiguity. The advantage of using low energy electrons over using high energy electrons is that

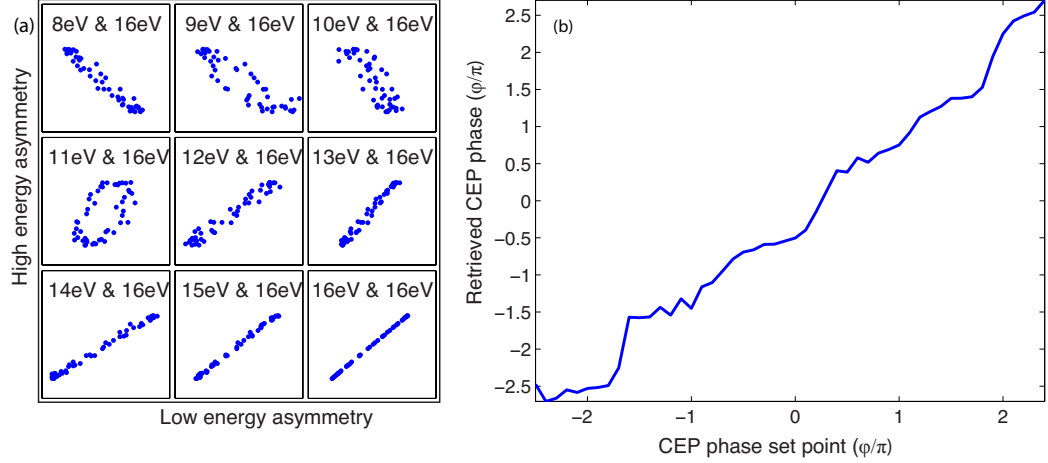


Figure 2.4: Phase ellipses obtained by taking lineouts at different positions of the spectrum in the low energy range that is dominated by the direct electrons. The retrieved phase on the right hand side is obtained using 11 eV and 16 eV energy windows.

the electron yield much higher allowing for low noise CEP detection without using very high gas densities. Another advantage of using low energy electrons is the better spectral resolution of time of flight spectrometers at lower energies.

2.4 Summary

Tunnel ionization is the starting point of most of the strong field interactions. In this chapter optical methods for the detection of tunnel ionization are described. Inspired by the work of Brunel [32], these methods rely on the detection of the generated new optical frequencies due to nearly step-wise increase of the density of the liberated electrons every half-cycle of the laser field. In case of ionization induced by a degenerate two-color field that yields directional current and THz emission, the direct detection of asymmetric electron current was detected using stereo-ATI electron spectrometer [46]. The ionization effects described in this chapter rely solely on the TI and the subsequent electron acceleration in the laser field. In the next chapter a high order harmonic generation process that involves recollision and the release of the EWP kinetic energy in the form of high energy XUV photon is discussed.

Chapter 3

High-order harmonic generation with cycle-sculpted pulses

3.1 Introduction

In chapter 2 the use of asymmetric waveforms was demonstrated for controlling ionization and steering of the liberated electrons. Here it is shown that these waveforms have a practical advantage for driving high-order harmonic generation [47]. Multicolor multi-cycle driver waveform allows modifying the returning electron trajectory and, simultaneously, accelerating the tunneled-out electron to a higher kinetic energy compared to the case of a single-color sinusoidal driver field [48]. Two-color high order harmonic generation has been extensively studied in the context of HHG spectroscopy [44, 49] and two-color gating for isolated attosecond pulse generation [45, 50, 51]. The attosecond HHG spectroscopy is a novel tool that has been shown to reconstruct molecular orbitals [52]. Using a two-color scheme for HHG where fundamental and second harmonic fields are cross-polarized, allows resolving the time when an electron exits a tunneling barrier [53]. Here we focus on the optimization of the HHG yield and extension of the cut-off toward the high photon energy.

HHG can be qualitatively described using a so-called semi-classical three step model [5] illustrated in Figure 3.1. The atom is exposed to a strong linearly polarized laser field. First, an electron from the outer shell tunnels through the barrier of the atomic Coulomb potential perturbed by the strong laser field. The quasi-free electron then follows the electrical field oscillations and subsequently acquires kinetic energy from it. In the case of a single-color driven HHG the maximum achievable photon energy is given by the well-known semi-classical cut-off law [6, 54]:

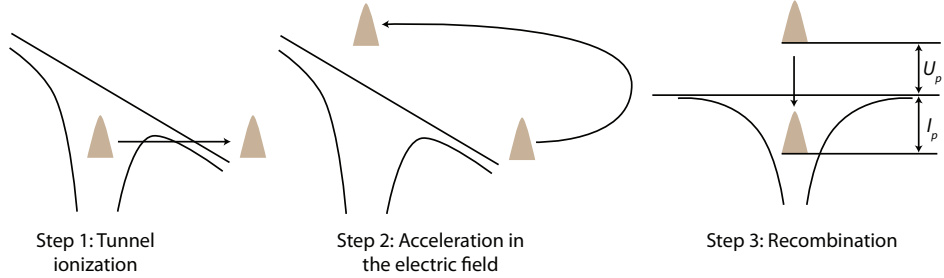


Figure 3.1: Three step model of high harmonic generation.

$$h\nu_{max} = I_p + 3.17U_p, \quad (3.1)$$

where I_p is the ionization potential of the atom and the ponderomotive energy U_p is the average electron quiver energy in the laser field:

$$U_p = \frac{q_e^2}{8c^3\epsilon_0 m_e \pi^2} \times \lambda^2 \times I, \quad (3.2)$$

here c is the speed of light, q_e and m_e are charge and mass of the electron, and λ and I are the wavelength and intensity of the driving laser field. In other words, the only available “knobs” for tuning the HHG cut-off (3.1) are the intensity and wavelength of the driving laser field and the ionization potential of the gas medium used for the generation. In the optimal conditions, the intensity of the driving laser field is limited to the order of 10^{14} W/cm² because of the rather low ionization fraction that still permits achieving phase matching [55, 56]. One can increase the cut-off by using high- I_p gases which allow using higher intensity before depleting the ground state of the generating medium [57], but highest I_p neutral gas available is Helium. HHG from ion targets [58] is severely limited by the plasma defocusing and strong phase mismatch effects. A much more promising route toward high photon energy coherent XUV radiation generation is the use of longer wavelength sources for driving the HHG [24]. Although the generation efficiency drops dramatically with increasing wavelength $\propto \lambda^{-6}$ [59], it has been shown that this scaling can be offset by a favorable phase matching properties at long wavelengths [25, 60].

Here we explore a different approach for increasing the cut-off by using multiple colors for shaping of the laser field cycle and controlling the electron wavepacket trajectory on the attosecond time scale. In a single color case the electrons that are ejected into continuum at the maximum of the field (maximum ionization rate) correspond to trajectories that do not return to the ion therefore most of the electrons that tunnel out do not contribute to

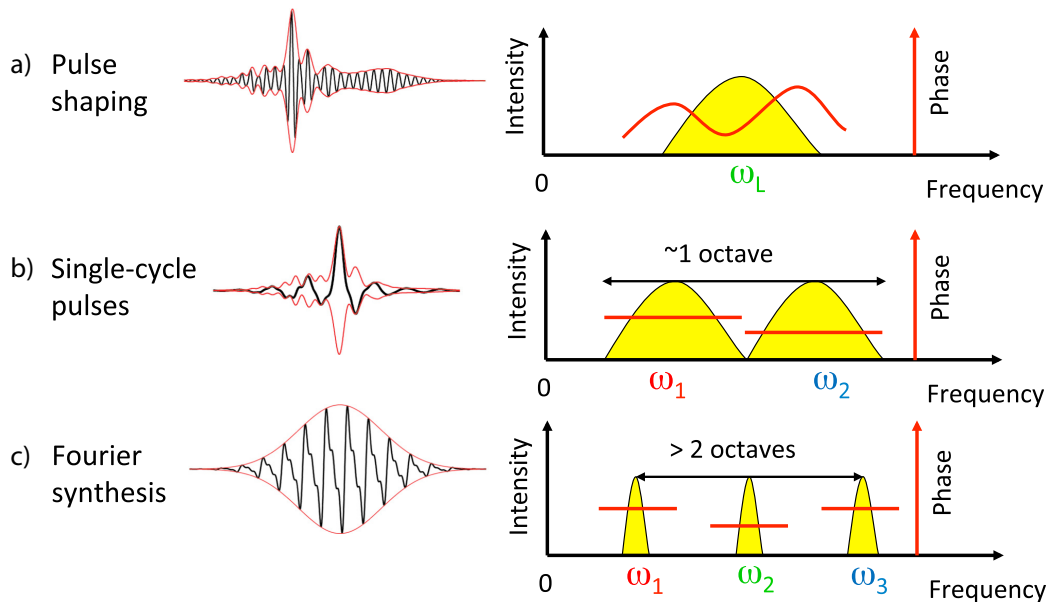


Figure 3.2: Different approaches for laser waveform shaping: a) shaping of a multi-cycle laser pulse via manipulation of spectral phase, b) control of the electric field of a single-cycle pulse, composed of broadband ultrashort “wavelets”, by varying the CE phase, c) multi-color Fourier synthesis approach.

the harmonic signal. Only those electrons that are born after the maximum of the field can return to the ion and generate useful HHG signal. In order to increase the efficiency of the HHG one can engineer the waveform of the electric field such that the electrons born at the peak of the laser field would be efficiently accelerated and return to the ion allowing it to recombine.

Initially a shaped waveform was suggested for optimized re-colliding electron steering dubbed “the perfect wave” composed of several color pulses. The perfect wave maximises the kinetic energy of the electron upon recollision, while keeping the corresponding excursion time short. The high kinetic energy of the electron wavepacket upon recollision allows generation of high harmonics with significantly higher cut-off. The efficiency is maintained by keeping the excursion time short, which prevents the continuum electron wavepacket from spreading. The optimum waveform or a so-called „perfect waveform“ resembles the saw-tooth shape and can be generated via shaping the waveform of the laser field.

An overview of different approaches for the control of a laser field is summarized in Figure 3.2. Pulse shaping has been successfully used for coherent control of chemical reactions [61]. These processes are relatively slow

and take place on the sub-picosecond time scale. Generally, the shortest time scale over which we can control processes is determined by the bandwidth of our control signal $\Delta\tau \propto \Delta\nu^{-1}$, which in our case is the bandwidth of a laser pulse. For example in order to control molecular motion that takes place on the picosecond time scale it is enough to shape the envelope of a pulse from a typical femtosecond laser amplifier as illustrated in Figure 3.2 a). However, when we want to control processes that take place on a time scale shorter than a cycle of the laser field, we need to have a bandwidth that spans over one octave. There are several ways to satisfy this condition. One way is to generate several broadband pulses so that the total spectrum covers nearly one octave or more and a single cycle or sub-cycle pulse transient is synthesized. Several groups are quite successfully using this approach, however, this is quite tricky to implement and still the control over the field shape on the sub-cycle time scale is rather limited [62, 63]. The main control parameter in this case is the control of the CEP of the laser pulse [64]. Varying the phase of the carrier wave under the envelope of an ultrashort few cycle pulse allows changing the field shape and controlling the ionization and electron trajectory a little bit. This allows controlling whether two or only a single XUV pulse is produced per one laser pulse [64]. A novel generation scheme of such very short phase-controlled sub-cycle pulses is described in chapter 8, however, here a different waveform control scheme based on multi-color pulse synthesis is analysed. Our approach is to use Fourier synthesis by synthesizing the field of discrete spectral components that individually are significantly narrower than the gap between them. Overall this covers a very broad bandwidth and allows high degree of control of the field cycle shape. Here it is shown that for repetitive processes like HHG this allows a high degree of control over the trajectory of the electron wavepacket on a sub-cycle time scale.

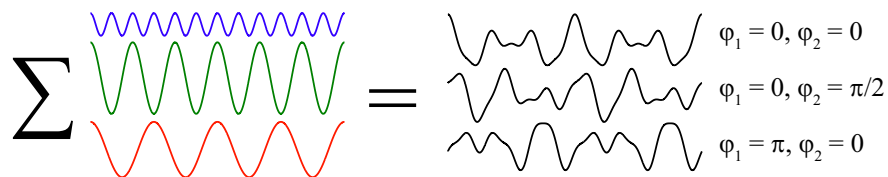


Figure 3.3: Three-color multi-cycle waveform synthesis concept with fixed amplitudes and tunable phases [48].

The initial suggestion for this optimized re-colliding electron steering assumed a combination of UV optical harmonics of a 800-nm laser and included a near-IR sub-harmonic (1600 nm) in the numerical analysis. Here an efficient and technically straightforward approach to adding Fourier components

at octave frequency spacing is implemented using a phase-locked parametric amplifier. Shaping of the waveform is achieved via delaying the phases of the different color components and allows controlling the HHG cut-off as illustrated in Figure 3.3.

3.2 Experimental setup

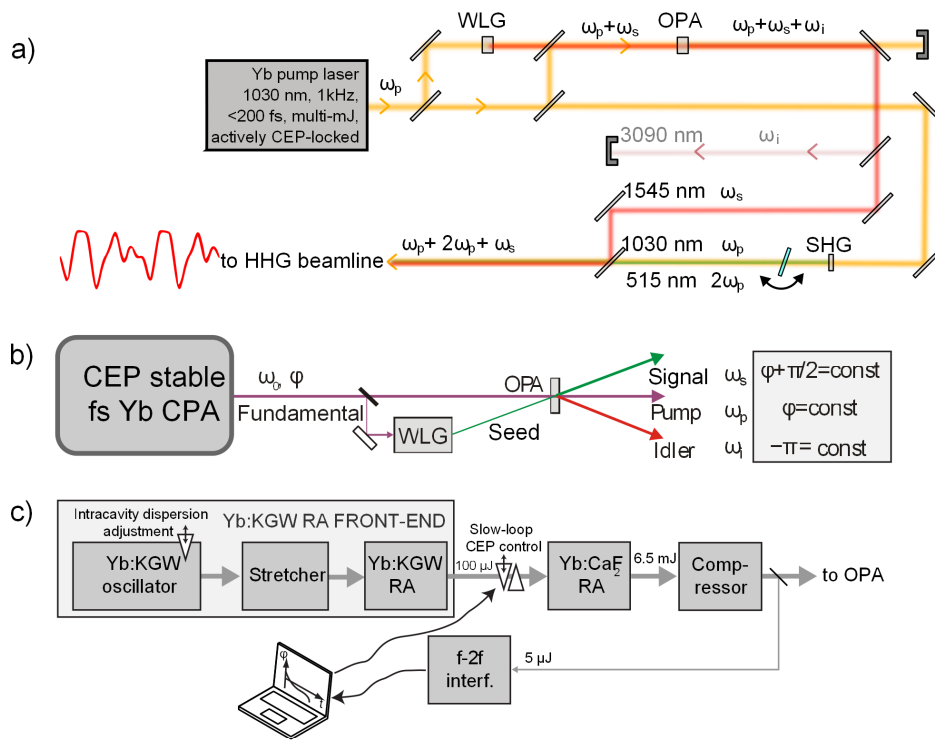


Figure 3.4: Concept of a three-wave CEP-stable synthesizer for HHG driving. a) general scheme of phase-locked multi-color OPA and dichroic beam combiner; b) collinear mid-IR CEP-stable OPA; c) a multi-mJ diode-pumped femtosecond 1- μ m CEP-stabilized pump laser.

The general scheme of the experimental setup is depicted in Figure 3.4. We coherently combine the output from a parametric amplifier to synthesize a multi-octave spanning Fourier components to synthesize a pulse with controlled waveform. The use of frequency down conversion allows extending the HHG cut-off to higher photon energy and avoiding multi-photon ionization. The parametric amplifier is seeded with a white light supercontinuum at 1545 nm which is then amplified in an OPA based on KTA crystal. We combine the output from the OPA with a pulse from the laser together with

its second harmonic. All these three colors are combined using dichroic optics and sent into the HHG beam-line. The polarizations of all color components are parallel, energies are ≈ 0.5 mJ, and the durations of all the pulses are comparable (170-200 fs).

In order to achieve a reproducible waveform for each laser pulse the phases of all individual colors have to be locked. For locking of the phases of the individual colors we combine the concepts of active CEP stabilization of the pump laser [10] and passive CEP locking in an OPA [65] illustrated in Figure 3.4 b). If the CE phase of the pump pulse is actively locked, at the output of the OPA we get three waves that are mutually phase locked. In the current state, idler wave is not used at the moment but potentially can be used to extend the concept of the multi-color synthesis to mid-IR spectral range.

An Yb:KGW CPA laser system is used as a front-end for a high energy Yb : CaF₂ regenerative amplifier (RA) [66]. Using an electronic phase-lock loop (PLL), the carrier-envelope-offset phase of the amplifier chain is actively stabilized [67]. A white-light seeded parametric amplifier is pumped with actively CEP stabilized pulses and yields phase locked signal, pump and idler waves that can be coherently combined. The results of the HHG driven by three incommensurate frequency fields are summarized Figure 3.5. Firstly, HHG was tested using 180-fs 1.03- μ m pulses directly from the Yb laser. Secondly, as a demonstration that the peak power of the system is sufficient for energy demanding applications such as HHG, we measure HHG in argon driven by two waves of our synthesizer individually: the signal wave at 1.545- μ m of a KTA OPA and the fundamental wave at 1.03- μ m, as shown in Figure 3.5a-b).

3.3 Results

Comparison of multi-color driven HHG to the case of individual color driver is summarized in Figure 3.6. A first obvious effect of coherently combining those two color components is the increase of harmonic peak density as it is apparent in Figure 3.5c. Due to a three times larger periodicity of the two-color field as compared to 1- μ m wave and asymmetric half-cycles, the density of the harmonic peaks increases six times. Since the amplitude of the individual peaks drops roughly only by a factor of 2, the total flux integrated over the spectrum of the denser-spaced harmonics increases dramatically. Moreover, the spectrum generated using the two-color driver extends beyond the transmission edge of aluminum filter, demonstrating that the cut-off can be pushed above the saturation limit of the 1030 nm 180 fs pulse.

When the third color pulse is added, the HHG spectrum becomes highly CEP-dependent and exhibits phase-dependent cut-off modulation. This CEP dependence signifies that sub-cycle shaping is a potential tool for controlling the dynamics of the electron in a strong laser field. The experimentally measured spectra for different waveforms are in good agreement with simulations based on strong field approximation (SFA) [68]. Also, another feature apparent in Figure 3.6 c) is the strong dependence of the cut-off on the carrier envelope phase of the driving laser pulse φ_{cep} . We keep the energies of all three color components the same and scan two phases. The relative delay between the 1545 nm and 1030 nm components is kept constant. Instead, we scan the CEP phase of the input laser pulse that runs through a complete set of waveforms. Another phase between the 515 nm and the 1030 nm fields is scanned by rotating a Brewster plate. After normalizing the spectra with recombination dipole spectrum we get the electron wave packet spectrum. The extensive trajectory analysis and absolute calibration of phases is described in Ref. [47]. Superposition of these different infrared colors with comparable amplitudes provides a route towards a source of high XUV photon energy and flux.

3.4 Summary

High order harmonic generation can be used as a tool for attosecond spectroscopy in the so-called *in-situ* or *ex-situ* configurations. In the *in-situ* spectroscopy, the high-order harmonic generation process encodes the attosecond dynamics in the emitted harmonic spectrum [44]. On the other hand, in *ex-situ* attosecond spectroscopy, the emitted attosecond pulses, typically synchronized with an IR pulse, are used to initiate and probe ultrafast dynamics [28]. Here a different scheme is explored based on multi-color waveform shaping that allows controlling and extracting information about continuum electron wavepacket. Also, the multi-color driven HHG can be used as an optimized source of XUV radiation for *ex-situ* spectroscopy. The key technological challenge behind the multi-color waveform synthesis is the locking of CE phase and is described in detail in the next chapter.

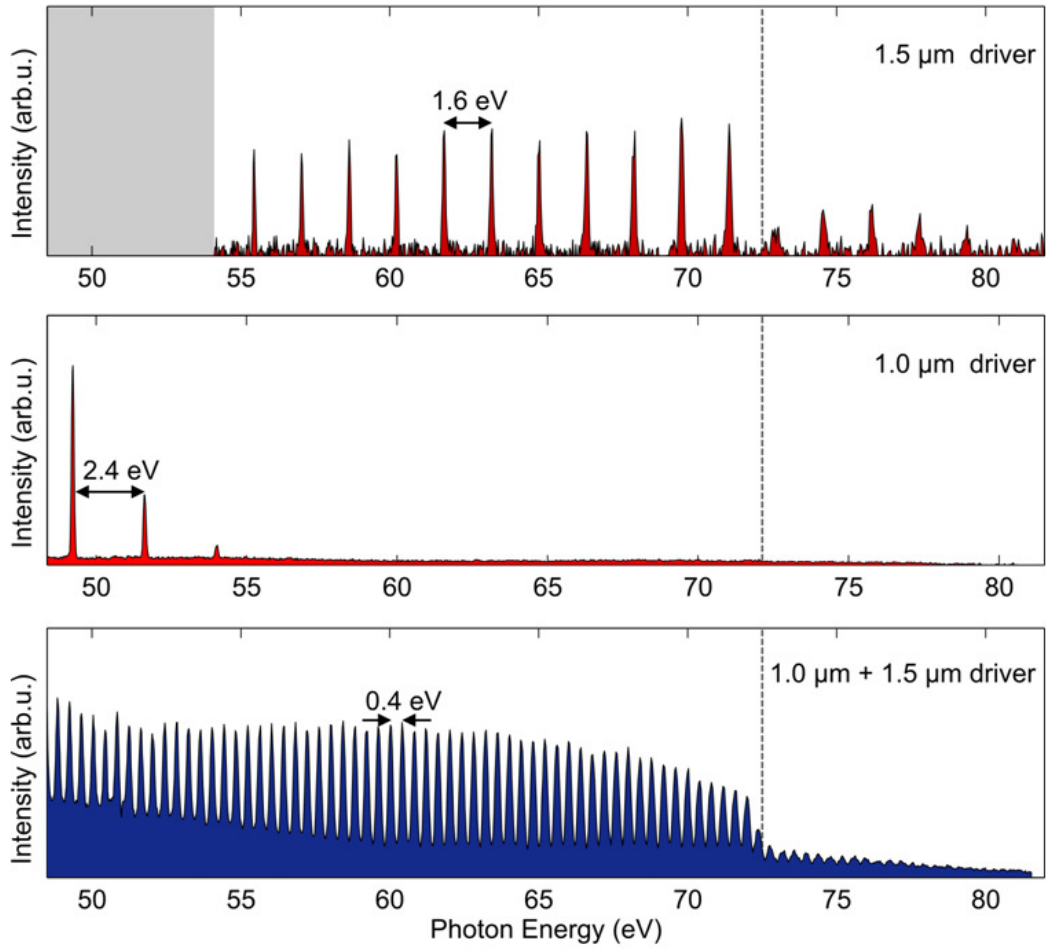


Figure 3.5: Multi-color HHG. Comparison of HHG spectrum generated in Argon using single color at a) 1.545 μm , b) 1.03 μm and c) Cut-off region of the HHG spectrum generated using two-color field composed of 1.03 μm (ω) and 1.545 μm ($\omega/1.5$) waves. The spectrum extends beyond the Al filter transmission edge at 72.5 eV.

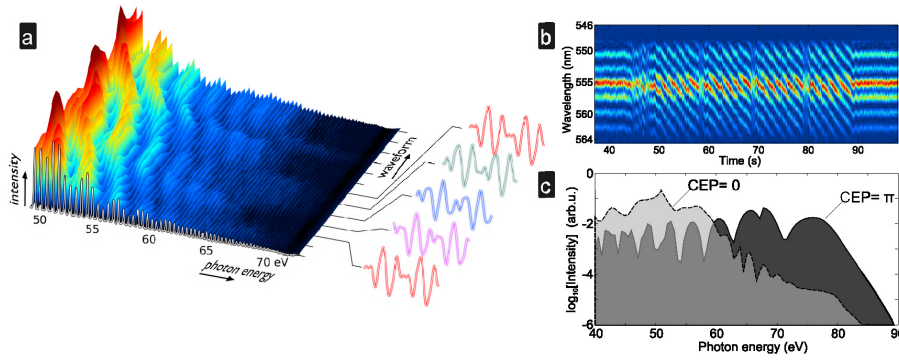


Figure 3.6: High order harmonic spectra generated with phase-locked multi-color pulses. a) a series of measured XUV high-order harmonic spectra generated using three colors, which depend upon the shape of the optical cycle of the generating intense infrared synthesized waveforms. The waveform is controlled by scanning the CEP of the driving laser pulse. b) $f-2f$ interference spectrum used for locking the CE phase. The region with slanted line pattern corresponds to the linear ramp of the phase which is used for the measurement of the HHG spectrum dependence vs phase. c) simulation of the three-color driven HHG spectra CEP dependence for different relative phases between the $1.545 \mu\text{m}$ ($\omega/1.5$) and $1.03 \mu\text{m}$ (ω) waves $\varphi_{rel} = 0$ and $\varphi_{rel} = \pi/2$.

Chapter 4

Carrier-envelope phase control of laser pulses

4.1 Stabilization of the Yb:KGW amplifier

Amplification of CEP stable pulses with a reproducible waveform under the pulse envelope is an enabling technology for a variety of strong-field control applications typified by the generation of isolated attosecond (10^{-18} s) pulses and directional electron emission in above-threshold ionization. Both actively stabilized laser CPA systems [69] and passively CEP stabilized parametric amplifiers [65] were reported. To date, amplified Ti:Sapphire based laser systems delivering actively CEP stabilized few-cycle sub-mJ pulses were successfully employed in numerous strong field experiments. Femtosecond diode pumped Ytterbium laser amplifiers present an interesting alternative to Ti:Sapphire because of the average power and repetition rate scalability [70]. The importance of CEP control is obvious for quasi-mono-cycle pulses and therefore is naturally linked to broadband Ti:Sapphire amplifiers. However, CEP control is also a prerequisite for the generation of reproducible multicolor fields comprised of carrier waves at arbitrary frequencies [43]. Although CEP-locked Yb fiber oscillators are widely used in frequency-comb metrology [71], such oscillators are not well suited for time-domain applications due to a significant phase jitter on the order of a few Hz. In precision frequency metrology, phase jitter does not play a dramatic role as the drift of CEP can be measured and taken into account during the measurement. An additional complication with dispersion managed Yb fiber systems is a relatively low attainable pulse energy insufficient for strong field applications. A solid-state Yb:KYW oscillator for metrology with CEP stabilization at a 160 MHz repetition rate was reported [72]. However, due to the difficulties

with pulse picking from a high repetition rate pulse train and reduced pulse energy, it is not suitable for seeding a kHz-repetition-rate amplifier.

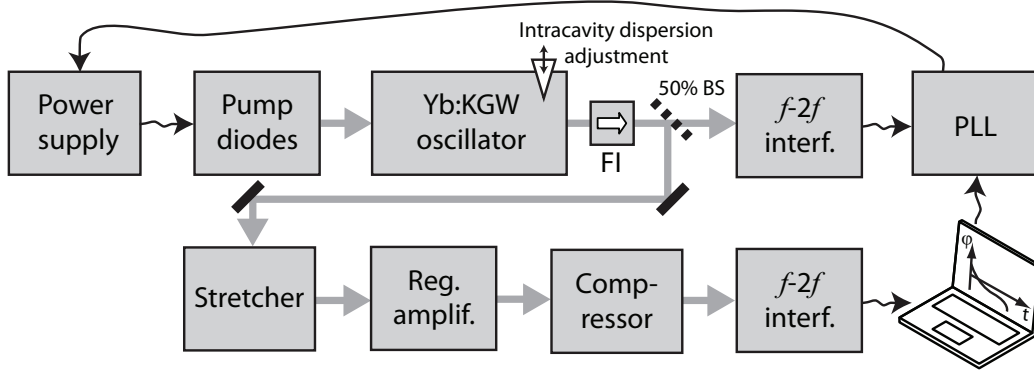


Figure 4.1: Scheme of CEP stabilization of the Yb:KGW CPA amplifier. FI - Faraday isolator, PLL - phase-lock-loop electronics, BS - beam splitter.

Here we describe the working of an all-solid-state CEP stable CPA laser system [67] that is based on an ytterbium-doped potassium gadolinium tungstate (Yb:KGW) oscillator and regenerative amplifier (RA). The energy of the high-repetition-rate pulses is sufficient to reach the 10^{14} W/cm² intensity level with soft focusing ($f=20$ cm), which is ideal for experiments like above-threshold ionization (ATI) and THz generation in plasma [43].

A general scheme of the amplified laser system and the CEP stabilization feedback loop is summarized in Figure 4.1. The Yb:KGW laser system is a CPA laser system based on a solid-state Kerr-lens mode-locked (KLM) Yb:KGW oscillator which is used as a seed for the Yb:KGW RA (Light Conversion Ltd.). The oscillator delivers 8-nJ pulses at a 75-MHz repetition rate. Both the oscillator and RA are longitudinally pumped by 980-nm laser-diode bars fitted with customized micro optics. Half of the oscillator output power is split off with a beam splitter and passed through a transmission grating pulse stretcher/compressor unit to extend the pulse duration to 250 ps before injecting it into the RA. The repetition rate of the amplifier can be continuously tuned in the 1-200 kHz range. The amplifier delivers an approximately constant average power of 6 W at 10-200 kHz repetition rate. The maximum energy of 1 mJ after a 80% efficient pulse compressor is reached at 1 kHz. Central wavelength of the amplified pulses is 1030 nm. The pulse duration is close to the transform limit and slightly varies in the range of 175-180 fs depending on the repetition rate (1-200 kHz) due to gain narrowing and saturation effects. The beam quality after amplification in RA is nearly Gaussian with beam quality parameter $M^2 < 1.1$.

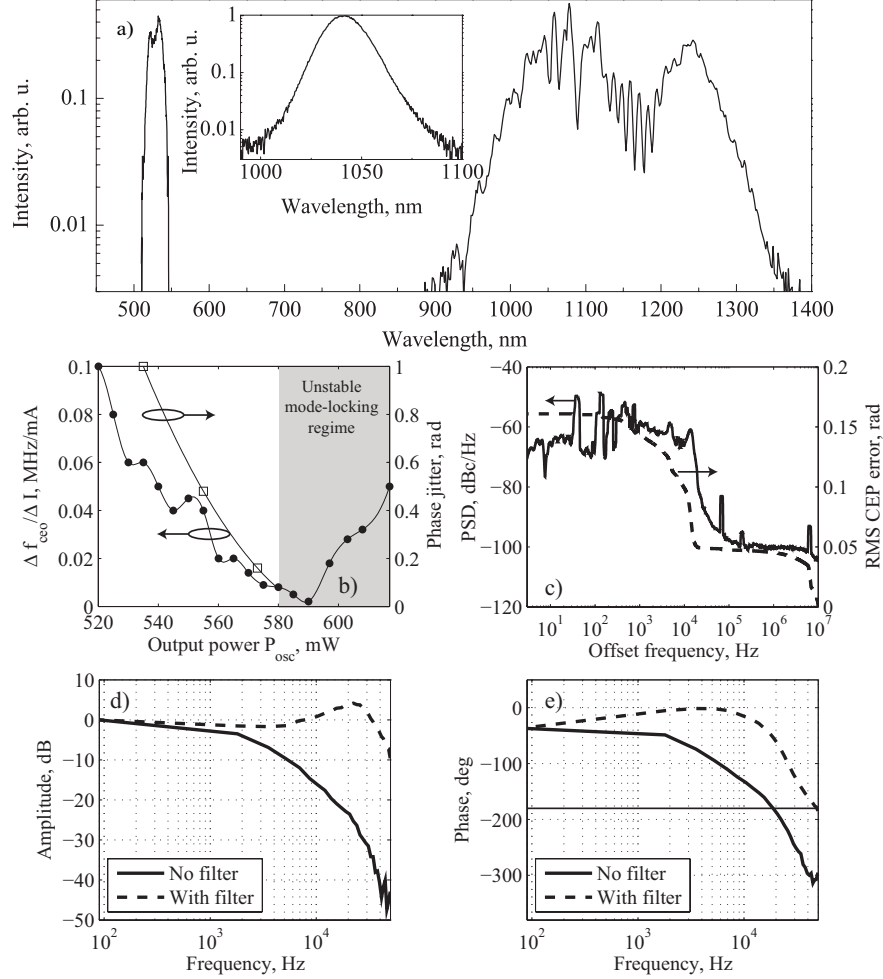


Figure 4.2: a) spectrum of the oscillator after broadening in a PCF. Inset: spectrum of the oscillator before the fiber, b) dependence of the f_{ceo} sensitivity on the output power of the oscillator (left) and corresponding measured integrated phase jitter (right), c) single side power spectral density of f_{ceo} phase noise. The right axis shows the integrated phase jitter calculated using (4.1), d) amplitude and e) phase transfer functions of the oscillator output power alone and with an active high-pass filter connected in series.

Since the stretcher and compressor are highly dispersive elements, beam pointing instability is sensitively reflected in the CEP noise. Due to a sufficiently large gain bandwidth of Yb:KGW that supports 180-fs amplified pulses with the spectral FWHM > 15 nm, the pulses can be stretched to a given pulse duration using a lower chirp rate, compared to the case of a robust but narrowband gain medium, such as Yb:YAG. Therefore, the broad-

band Yb:KGW system is potentially superior in terms of its CEP stability and susceptibility to external mechanical noise as a consequence of the short grating separation distances in the stretcher/compressor.

The oscillator output spectrum (see the inset of Figure 4.2(a)) supports FWHM 62-fs transform-limited pulses. The cavity dispersion is balanced by chirped mirrors and finely tuned with an intracavity prism pair, which is also used to adjust the f_{ceo} offset frequency. A Faraday isolator is installed at the oscillator output in order to suppress parasitic feedback from the nonlinear interferometer and the amplifier. Without the isolator, the feedback caused additional noise that disrupted the phase lock. The remaining half of the oscillator output power (approximately 250 mW) is directed into the nonlinear interferometer (MenloSystems GmbH) for f_{ceo} detection. The oscillator output is spectrally broadened in a 5-cm-long piece of photonic crystal fiber (PCF) that has a zero of group velocity dispersion at 850 nm. The resultant supercontinuum spectrum has two pronounced maxima at 1000-1300 nm and 520 nm as shown in Figure 4.2(a). The optical delay between the two spectral parts is adjusted and the infrared continuum part is frequency-doubled in a two-color Mach-Zehnder interferometer. The beat signal in the output of this nonlinear f - $2f$ interferometer is then detected with a fast avalanche photodiode. Beat note signal of the unlocked oscillator is > 50 dB above the noise floor in 20 kHz resolution bandwidth. Using a phase-lock-loop (PLL), the carrier-envelope-offset frequency f_{ceo} is locked to a reference signal which is a quarter of the pulse repetition rate $f_{rep}/4$. The feedback loop is closed by supplying the signal from the phase locking electronics to the oscillator laser diode driver (Newport, 5600 Series controller). A significant advantage of an Yb DPSS Kerr-lens mode-locked oscillator over its Ti:Sapphire counterpart is the possibility to control the CEP by modulating the laser diode current with up to a multi-megahertz modulation frequency, i.e. much faster than the system memory effect determined by the rather long 0.6 ms upper state lifetime. The oscillator was optimized to mode lock in a regime where the dependence of f_{ceo} on pump current is the weakest (0.01 MHz/mA). This greatly reduces amplitude-to-phase noise coupling from the pump source (the laser diode driver and the diode itself) [73]. The offset frequency sensitivity to the diode current $\Delta f_{ceo}/\Delta I$ is strongly dependent on the output power of the oscillator and in our case has a minimum at around 580 mW, as shown in Figure 4.2(b). Further increase of the output power leads to the appearance of a CW peak in the oscillator spectrum and makes the operation of the oscillator unstable. Due to power-to-phase coupling, the phase jitter σ increases with increasing sensitivity, which suggests that the noise of the oscillator can be further reduced by suppressing the noise of the power supply electronics.

Using a specially designed electronic second-order active high-pass filter

which improved the amplitude and phase transfer function of the oscillator, we extended the bandwidth of the feedback loop approximately fivefold to 50 kHz, which greatly reduced the jitter of the amplified pulses. The amplitude and phase of the laser power modulation were measured as a function of modulation frequency and the filter was tuned to compensate the decrease of amplitude and the phase lag at high frequencies. An approximate f_{ceo} transfer function of the unlocked oscillator can be determined from the oscillator output power transfer function which was measured by sweeping the modulation frequency of the pump current in the 1 Hz-50 kHz range and monitoring the oscillator output power modulation amplitude using a photodiode and a lock-in amplifier. With the filter included in the scheme, the bandwidth of the power modulation reaches 50 kHz at -10 dB as shown in Figure 4.2(d-e).

The phase stability of the oscillator was measured using a second out-of-loop f - $2f$ nonlinear interferometer (MenloSystems GmbH) with the goal to quantify the noise level induced during spectral broadening in the PCF. The measured power spectral density (PSD) of f_{ceo} [74] phase noise (Figure 4.2(c)) drops down rapidly at around 20 kHz, consistent with the slow response of the laser gain medium shown in Figure 4.2(d). The integrated phase jitter (4.1) from 10 MHz to 3 Hz corresponds to 0.16 rad.

$$\Delta\phi(f) = \left[2 \int_f^{10\text{MHz}} S(f') df' \right]^{1/2} \quad (4.1)$$

The fiber introduces approximately 30 mrad integrated phase jitter, as deduced from the comparison of the in-loop and out-of-loop measurement of PSD, while the main part of the noise comes from the residual noise of the pump diode power supply.

Phase stability of the amplified pulses was measured using a third out-of-loop interferometer where spectral broadening is performed in a bulk sapphire plate. The interference pattern and the reconstructed phase over time is shown in Figure 4.3(a-b). In addition to the (fast-loop) oscillator stabilization, the phase drift in the amplifier is compensated using an additional slow-loop stabilization. A personal computer is used to determine the CEP from an f - $2f$ spectral interferogram and to send a feedback signal to the oscillator PLL electronics. A single-shot measurement of CEP with and without slow loop is shown in Figure 4.3(c-d). To facilitate root-mean-square (r.m.s.) phase noise characterization, the pulse repetition rate of the amplifier was reduced to 10 kHz at which the spectrometer (Thorlabs Inc.) is still capable of capturing a nonlinear f - $2f$ spectral interferogram in each laser shot. The r.m.s. width σ of the CEP distribution (Figure 4.3(e)) is 0.45 rad, which corresponds to ≈ 250 attosecond timing jitter. The remaining phase jitter of

the amplified pulses is due to the residual phase jitter of the oscillator pulses and phase distortions accumulated during amplification. One important difference as compared to the typical CEP stabilized Ti:Sapphire systems in a multi-pass amplifier configuration, is that the gain of Yb:KGW laser medium is much lower (≈ 1.3 per pass), which implies a large number of round-trips in the RA cavity. This elongates the effective beam path of the injected pulse and increases the sensitivity to the acoustic vibrations of the Pockels-cell (PC) [75]. The number of roundtrips in 2.2 m long RA cavity was set to 20, which is optimal for the 10 kHz repetition rate used for the measurements.

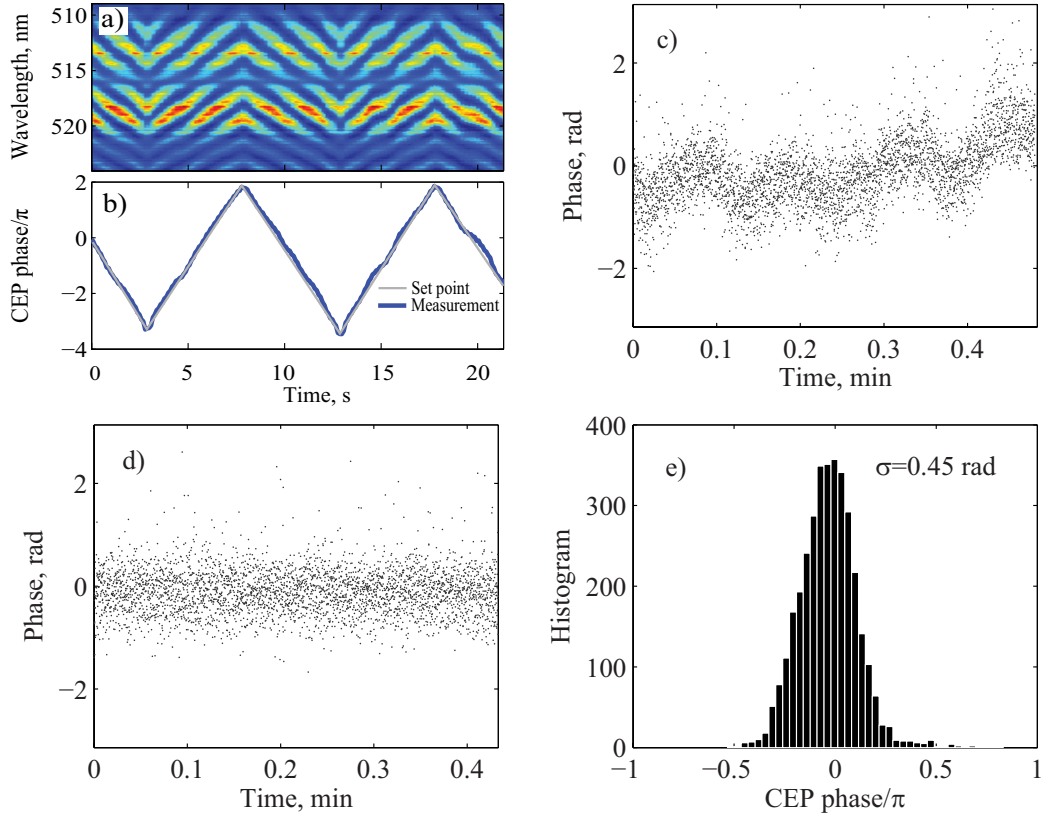


Figure 4.3: CEP stability after amplification in RA. a) interference pattern of the f - $2f$ spectrum of the amplified pulses measured using an out-of-loop f - $2f$ interferometer, b) comparison of the phase calculated from the interference pattern to the set-point of the phase. A saw-tooth modulation was applied to distinguish between the intrinsic modulation in the supercontinuum spectrum and the CEP-sensitive interference fringes, c) single-shot measurement of CEP of the amplified with oscillator stabilization only, d) CEP with compensation of drift with a slow-loop, e) distribution of the CEPs with slow-loop switched on. r.m.s width is $\sigma = 0.45$ rad.

4.2 Direct amplifier stabilization

Since its original demonstration over a decade ago, carrier-envelope phase (CEP) control [74, 76] of mode-locked lasers has come of age, with a recently demonstrated timing jitter between the carrier and the envelope pushed down to sub-10-attosecond range [77, 78]. Despite such impressive progress, CEP control is still limited to a rather narrow class of lasers, including Ti:sapphire and some other selected broadband solid-state materials as well as some mode-locked fiber lasers. Moreover, CEP control becomes increasingly complex for amplified laser sources with energies in the millijoule range [79]. Typically, stabilization of a CPA laser source relies on an intricate combination of two servo loops, a fast oscillator loop and a slow amplifier loop [10]. While the second loop is necessary to remove residual phase drift in the amplifier, unfortunately, it also corrupts the residual phase noise in the amplified pulse train due to the limited feedback bandwidth as a consequence of a low repetition rate of the amplifier and a slow readout of a nonlinear phase meter [80]. While oscillators can nowadays be stabilized down to ≈ 10 mrad residual CEP jitters [77], 100 mrad stability for an amplified laser source already appears to be a challenge. Here we demonstrate a direct and versatile method to stabilize the CEP of an Yb:KGW MOPA laser system, resulting in sub-100 mrad stability. To the best of our knowledge, this value surpasses most previously measured CEP jitter for Ti:sapphire CPA systems as well as previously reported stabilization of Yb-based laser systems [81, 82].

Analyzing the problems of the CEP control in amplified lasers, the measurement of CEP after amplification appears to be a major bottleneck [83]. Typically, a spectral-interferometry based scheme [84] is employed for the purpose, which requires averaging over > 10 laser shots to avoid detrimental feedback from detection shot noise contributions. The bottleneck in this detection process is the number of useful photons in the narrow SHG conversion bandwidth of the f - $2f$ interferometer [85, 86]. As shot-noise limited CEP detection appears much less challenging [84] for the oscillator heterodyning scheme [86] than for the spectral interferometry scheme used with amplifiers [85], we chose to combine the virtues of both approaches, detecting the CEP of a high-repetition-rate amplifier with the heterodyne scheme that has only been applied to oscillators so far.

In our experiments, we employed a commercial Yb:KGW regenerative CPA system (Light Conversion Ltd.) seeded by a solid-state Yb:KGW Kerr-lens mode-locked oscillator [67], see Figure 4.4 for the general set-up. The oscillator operates at a repetition rate of $f_{\text{rep}} = 75$ MHz; the amplifier repetition rate f_{amp} can be freely tuned up to 1 MHz. With the latter settings, the amplifier delivers average power of 6 W and a pulse duration < 190 fs. Our

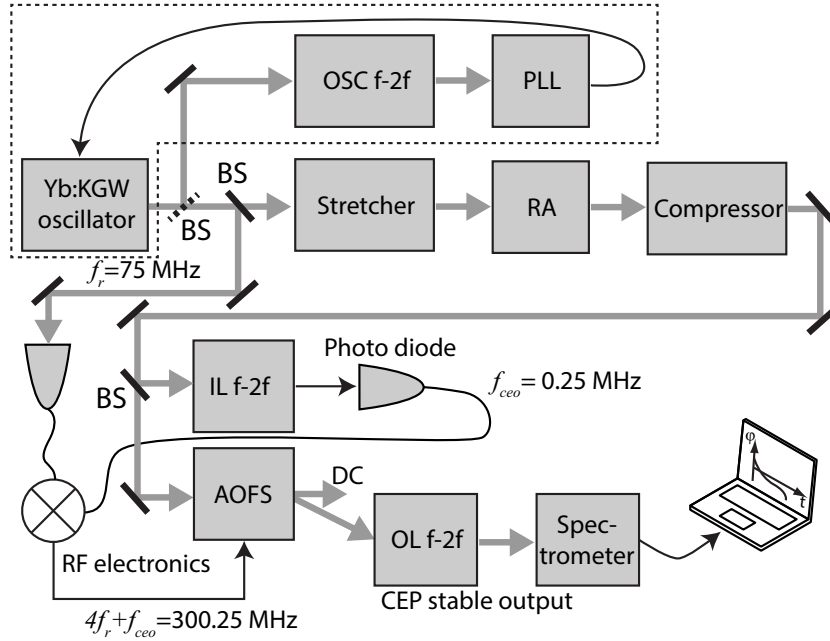


Figure 4.4: General scheme of the frequency synthesis for the stabilization of a sub-MHz frequency comb from a regenerative amplifier (RA). The dashed box indicates a part of the setup that is only necessary for an in-depth characterization of amplifier noise.

CEP detection scheme is based on in-line interferometers as they are customarily used for amplifier measurements, but have also been approved for use with oscillators [87]. The optical layout of our in-loop (IL) interferometer is shown in Figure 4.5. Supercontinuum is generated in bulk sapphire with μJ input energy from the amplifier. The resulting white light is collimated using a spherical mirror. A pair of wedges allows for adjustment of the relative group delay of the f and $2f$ components. The light is then refocused into a BBO crystal for second harmonic generation, phase-matched at 530 nm. This results in orthogonally polarized f and $2f$ components. The group delay between these components is then equalized in a 10 mm long birefringent quartz block. Finally, a polarizer heterodynes both polarizations and the beam is spectrally filtered before photo detection. A third $f-2f$ interferometer after the oscillator was used together with a phase-locked loop (PLL) for characterization of the amplifier noise discussed below. This interferometer is not part of the direct amplifier CEP stabilization scheme.

The measured CEP beat note frequency f_{CEO} at the output of the interferometer lies in the range between 0 and 500 kHz. For CEP stabilization, the feed-forward scheme [84] is employed. This scheme is based on an acousto-

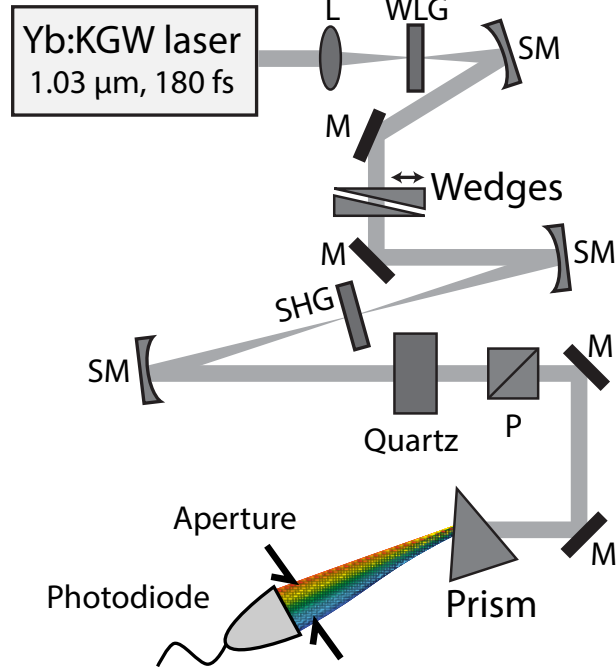


Figure 4.5: Optical scheme of the in-line f - $2f$ interferometer based on white light generation (WLKG) in a bulk sapphire crystal for beat-note detection, here P - polarizer, SM - spherical mirror.

optic frequency shifter (AOFS), which is normally directly driven at the fundamental beat note f_{CEO} . Given that our AOFS has a center frequency of 300 MHz, a higher-order beat note is used $f_{\text{AOFS}} = Nf_{\text{amp}} + f_{\text{CEO}}$, with an integer number $N \sim 300$. In this case, direct filtering of the AOFS driver signal becomes very challenging. Detecting the interferometer output with a > 300 MHz bandwidth leads to a tightly spaced comb. Compared to a comb signal with f_{rep} spacing, the energy of the individual beat note is about 2 orders of magnitude lower, which leads to a reduction of the electronic signal-to-noise ratio by 40 dB. The solution here is to use a slow photodiode with large detection area and synthesize f_{AOFS} by mixing the fundamental beat with a suitable harmonic of the amplifier repetition rate. The photodiode used in the experiments exhibits a 13 mm^2 active area (Thorlabs PDA36A, used at $75 \text{ k}\Omega$ trans-impedance). The capacity of the diode in combination with the high gain act as a lowpass filter and limit the bandwidth to $\approx 150 \text{ kHz}$. This bandwidth is sufficient for measuring the fundamental beat over a significant part of the free spectral range. The noise-equivalent power (NEP) of our photodetector is specified as $\approx 1 \text{ pW}/\sqrt{\text{Hz}}$. With a mea-

sured power of $35 \mu\text{W}$ on the detector, we therefore expect that shot noise ($\sim 4 \text{ pW}/\sqrt{\text{Hz}}$) dominates the noise floor. Identical signal strength of the f and $2f$ signal provided and assuming the absence of out-of-band contaminations, these settings should readily enable a beat note visibility of more than 60 dB in a 100 kHz bandwidth, which clearly illustrates the potential of our method.

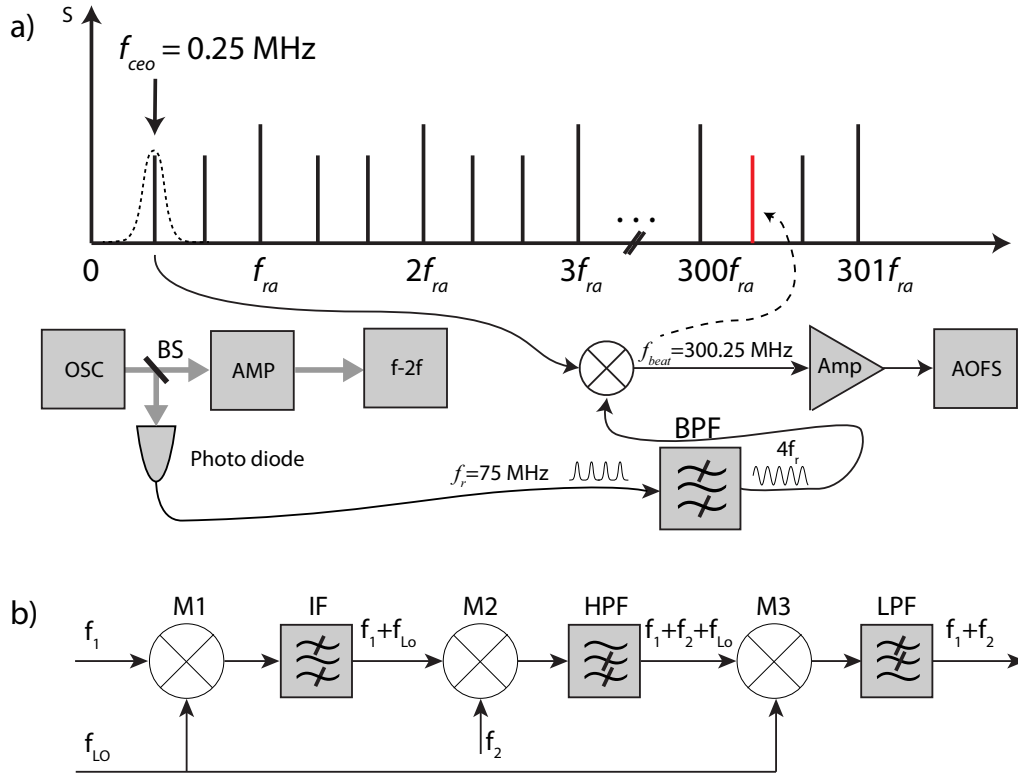


Figure 4.6: a) A general scheme of the frequency synthesis for the stabilization of a sub-MHz frequency comb from a regenerative amplifier (RA), b) narrowband tunable frequency filter scheme.

The driver signal is synthesized from the fourth harmonic of the oscillator repetition rate and the amplifier carrier-envelope frequency, i.e., $f_{\text{AOFS}} = 4f_{\text{rep}} + f_{\text{CEO}}$. An intermediate frequency scheme is employed to suppress mirror frequencies and other spurious contributions, see Figure 4.6. This scheme uses a narrow bandpass filter (RF Monolithics, PX1004-1, 82.2 MHz center frequency, 80 kHz 3 dB bandwidth). In a first mixing step, the fundamental beat is up-converted to the center frequency of the filter using a local oscillator at $\approx 82 \text{ MHz}$. Figure 4.7 shows the measured rf spectrum prior to narrow bandpass filtering. For comparison, Figure 4.7 also shows the signal

that is obtained when the interference is disabled by inserting a glass plate into the beam path of the f - $2f$ interferometer. The observed visibility of the beat note indicates that residual phase jitters well below 100 mrad are possible [88].

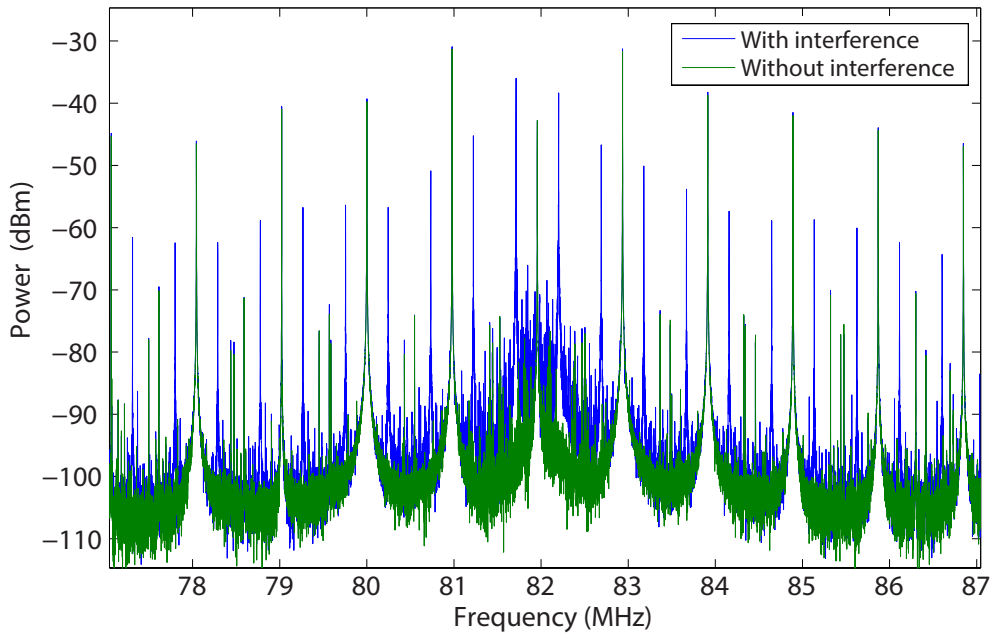


Figure 4.7: Radio frequency spectrum after mixer M1 where the signal from the photodetector is upconverted by mixing it with a local oscillator. For comparison, a reference spectrum is shown where the f and $2f$ components are delayed, and the beat note is suppressed. Beat note visibility is 55 dB in a resolution bandwidth of 6 Hz.

Using out-of-loop (OL) characterization with a second inline interferometer, the performance of the CEP stabilization scheme was analyzed, see Figure 4.8. This analysis indicates a residual rms jitter of $\sigma = 87$ mrad. The inset of Figure 4.8 shows a histogram representation of raw spectral interference patterns to further illustrate the surprisingly low phase jitters obtained with our scheme. It should be noted that the bandwidth of this scheme relies on the narrowest filter (80 kHz bandwidth) in the frequency synthesis scheme shown in Figure 4.6. Moreover, the acoustic travel time in the AOFS is on the order of a microsecond and certainly did not limit the obtained performance.

Generally, CEP noise in an amplified laser system may originate from the oscillator or from the stretcher/compressor pair and the regenerative amplifier itself. These two contributions, $\Delta\varphi_{\text{osc}}$ and $\Delta\varphi_{\text{cpa}}$, respectively, are

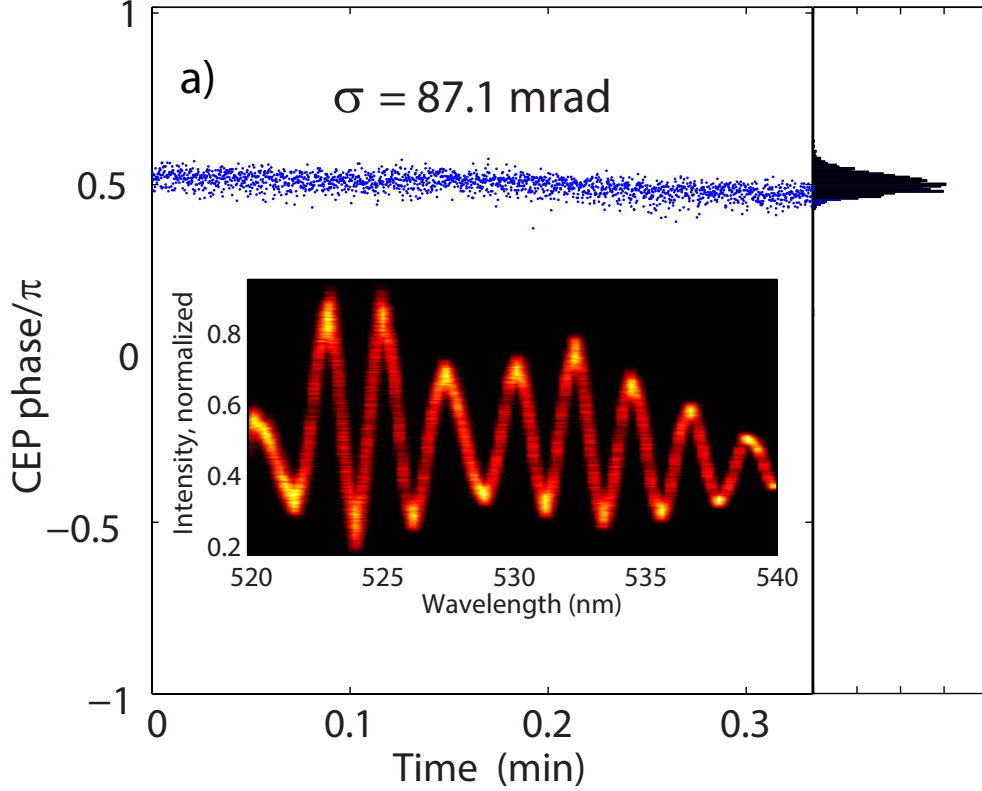


Figure 4.8: Out-of-loop CEP jitter measurement after the amplifier, inset: $f-2f$ interferogram fringes. The spectrometer integration time was kept minimum and averaging is done over 6 laser pulses. b) measured amplifier phase noise spectrum when the oscillator CEP was locked with a feed-back loop.

non-correlated. The total resulting phase jitter amounts to

$$\Delta\varphi_{\text{total}} = \sqrt{\Delta\varphi_{\text{osc}}^2 + \Delta\varphi_{\text{cpa}}^2}. \quad (4.2)$$

In order to evaluate the relative strength of these two contributions and for analysis of the requirements for the feed-back loop bandwidth, the amplifier phase noise contributions $\Delta\varphi_{\text{cpa}}$ was isolated by locking the oscillator offset frequency using a conventional feedback PLL, similar to Ref. [67]. In this configuration, a third $f-2f$ interferometer is used after the oscillator (dashed box in Figure 4.4) for CEP locking, and the $f-2f$ interferometer after the amplifier (cf. Figure 4.5) acts as out-of-loop interferometer for amplifier and stretcher/compressor induced noise characterization. The resulting phase noise spectrum of the CEP beat note ($f_{\text{CEO}} = 150$ kHz, $f_{\text{amp}} = 600$ kHz) is shown in Figure 4.9. The sensitivity of the measurement apparatus was

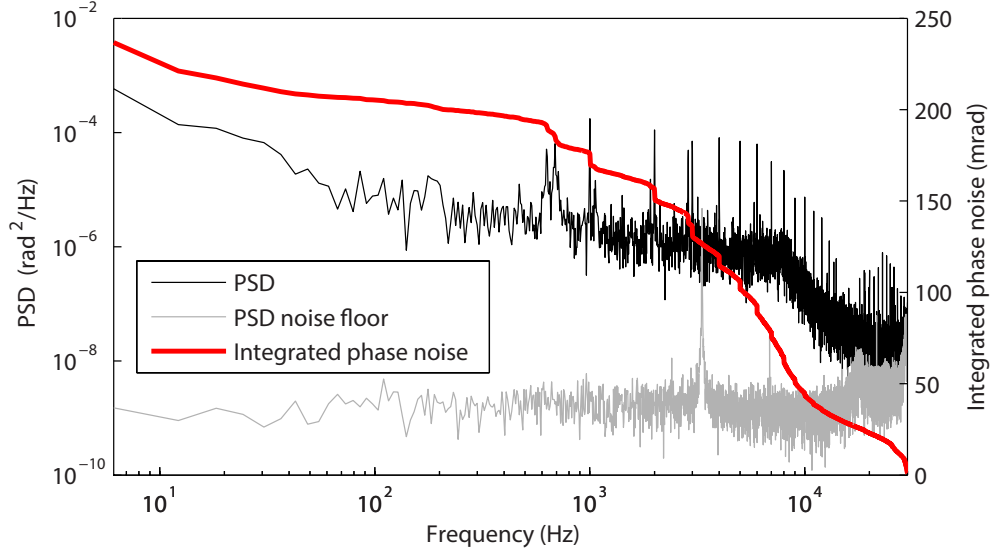


Figure 4.9: Phase noise spectrum density (PSD) and integrated phase noise measurement of an amplifier running at repetition rate $f_{\text{amp}} = 600$ kHz. The noise floor (gray line) is obtained by delaying the two colors in the f - $2f$ interferometer and represents the measurement sensitivity.

checked by inserting an ≈ 10 mm thick glass plate into the beam after white light generation in order to delay the f and the $2f$ component, thereby suppressing their interference. With the exception of a single artifact at 3.3 kHz, this setup provides a phase signal-to-noise ratio in excess of 30 dB for frequencies up to 10 kHz. The measured phase jitter corresponds to ≈ 230 mrad, which is about three times larger than the value deduced from Figure 4.8. Despite the slightly different measurement methods, this finding clearly corroborates the superior noise performance of this novel direct amplifier stabilization approach. In principle, the origin of this noise may either be the low sensitivity of the oscillator f - $2f$ interferometer or a large amount of excess noise in the amplifier. If the latter were true, one would expect to see a structured noise spectrum rather than a flat plateau [88]. In any case, it appears challenging to reduce this broadband 230 mrad noise signature with the traditional slow spectral interferometry approach [85] typically employed for amplifier stabilization.

To summarize, in this section an amplified ytterbium-based amplifier system with sub-100 mrad CEP jitter using feed-forward scheme is described. The scheme is currently applicable for intermediate laser pulse energy in the μJ range, essentially limited by self-phase modulation and optical damage in the AOFS. Investigations are underway to remove the acousto-optic

component from the unattenuated amplifier output, which will eliminate the corresponding power limitations. A further constraint arises due to the bandwidth of the noise spectrum of the oscillator [80]. The current scheme enables phase noise removal at frequency components up to 1/2 of the amplifier repetition rate. Given the advantage of rf heterodyning, the scheme is most effective in the laser amplifiers operating at a higher repetition rate, 10 kHz or above. This scheme significantly widens the scope of feed-forward stabilization. High pulse energy ≈ 200 -fs Yb amplifiers offer an efficient way to attain few-cycle pulses through nonlinear pulse compression schemes and optical parametric amplifiers - with the latter being seeded and pumped by a single Yb laser source. Demonstration of a sub-100-mrad CEP jitter at the Yb amplifier output, therefore, radically simplifies the task of deriving usable CEP-stable few-cycle waveforms from Yb driver lasers. This novel scheme paves a way to combine the efficiency and output power scalability of ytterbium-based materials with the precision previously only obtained with Ti:sapphire based approaches.

4.2.1 Feed-back scheme for direct amplifier stabilization

The laser amplifier stabilization of CEP scheme based on the feed-forward approach presented in Section 4.2 is directly applicable for moderate pulse energies. The useful CEP stable part of the beam is the diffracted beam, and one has to send the full pulse energy into the AOFS. In order to overcome this limitation, a modified scheme for direct CPA amplifier CEP stabilization based on feed-back approach was tested. In this scheme, the diffracted and the direct beams are effectively exchanged, and the diffracted beam is only used for the detection of the beat note, resulting in a CEP stable output of the amplifier itself. This allows splitting off a fraction of the laser pulse energy that is just sufficient for beat note detection, enabling use of the remainder of the pulse energy for applications. Consequently, this approach greatly reduces the intensity on the AOFS makes the scheme scaleable to high pulse energies.

The experimental and the electronic scheme of the laser amplifier stabilization using feed-back approach is shown in Figure 4.10 a). The beat-note is detected after the amplifier, filtered, upconverted by the repetition rate of the oscillator, and finally sent to a phase-lock loop, which locks a local oscillator (f_{LO}) centered at 75 MHz (close to the repetition rate of the oscillator) to the synthesized signal ($f_{rep} + f_{CEO}$) as shown in the rf synthesis electronic scheme depicted in Figure 4.11. The AOFS is driven by a signal that is synthesized from the f_{LO} frequency generator and the third harmonic of the oscillator repetition rate, such that the final driver signal of 300 MHz

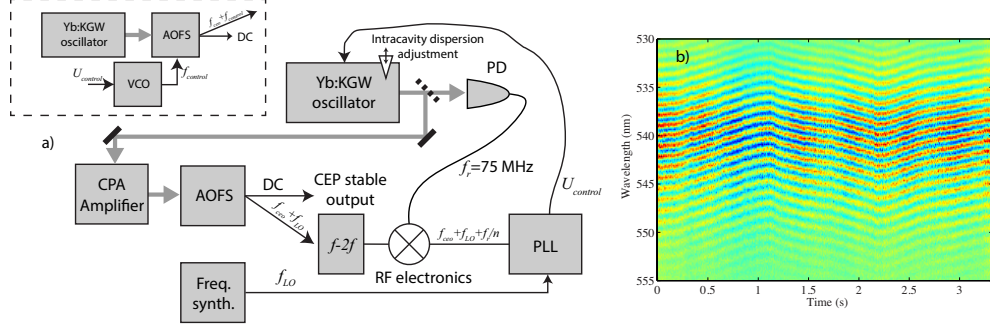


Figure 4.10: a) Scheme for direct CEP stabilization of a sub-MHz laser amplifier using feed-back loop. Inset: alternative control of the offset frequency via an additional AOFS. b) $f - 2f$ interference fringes modulated with saw-tooth offset phase.

frequency lies in the working range of the AOFS. The AOFS before the beat note detection in the $f-2f$ interferometer is necessary in order to ensure that every pulse in the amplified pulse train has constant CEP. This is accomplished by first shifting the offset frequency to a non-zero frequency via f_{LO} and then locking the detected beat-note by sending the feed-back to the oscillator pump source. Since $f_{rep} + f_{CEO} = f_{LO}$ due to PLL lock and because the AOFS subtracts a $4f_{rep} + f_{CEO}$ frequency from the original pulse train, the output directly from the laser becomes CEP stable. Figure 4.10 b) shows the interference fringes when the CEP locking is done using the PLL scheme. The phase is modulated supplying a saw-tooth modulation to the phase offset input of the lockbox. The resulting phase patterns illustrate that the CEP is stable and controllable.

This advanced scheme is more scalable in terms of pulse energy. The phase noise of oscillator and amplifier are measured in a single $f-2f$ interferometer and compensated by the fast feed-back loop. However, some of the merits of the feed-forward approach are lost. Namely, the feed-back bandwidth is limited by the slow response of the laser gain medium, and amplitude-to-phase coupling is introduced in the oscillator. This issue can be resolved using a modified feed-back scheme where a second AOFS is placed right after the oscillator and where a voltage controlled oscillator (VCO) is used for the control of the offset frequency by the PLL, as shown in the inset of Figure 4.10 a). In this case the bandwidth of the feed-back loop is determined by the bandwidth of the AOFS and is not limited by the excited state lifetime of the Yb oscillator.

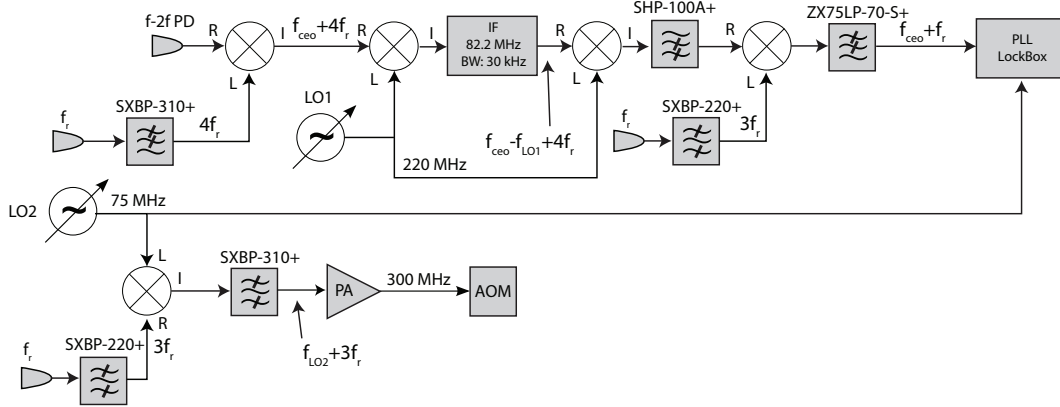


Figure 4.11: Electronic scheme for CEP stabilization using feed-back scheme.

4.3 Summary

To summarize, in section 4.1 an all-solid-state actively CEP stabilized amplified Yb CPA laser system is described that delivers 180 fs mJ level pulses with r.m.s phase jitter of approximately 0.45 rad, which is close to the established Ti:Sapphire laser systems despite the orders of magnitude longer upper lasing state lifetime in the Yb medium. This development opens a way to up-scale the repetition rate and the average power of amplified CEP stable systems. Direct locking of the high repetition rate amplifier is demonstrated using feed-forward scheme allows reduction of the CEP jitter below 200 mrad as described in section 4.2.

Chapter 5

Improving parametric amplifier efficiency via pulse shaping

Optical parametric chirped pulse amplification (OPCPA) is rapidly gaining ground as an approach to generate intense few-cycle pulses [89] and reach IR wavelength ranges [90] where there are no suitable laser gain media for high-energy operation. Parametric amplification permits extraordinarily broad phase-matching bandwidths and a huge single-pass gain, thus dismissing the concern for spectral gain narrowing which is a perennial problem in laser amplifiers. However, the high OPA gain has its negative side: for a bell-shaped intensity profile of the pump pulse/beam the unsaturated gain varies exponentially with intensity, resulting in an effective temporal/spatial filter. The obvious remedy would be a top-hat pump pulse and a top-hat pump beam.

Here the advantage of a relatively large bandwidth of a DPSS Yb:CaF₂ amplifier are demonstrated which allows us to implement a straightforward inline shaping technique and obtain a pulse profile optimized for OPA pumping. Whereas the described technique requires minimal changes of the pump laser source, it brings by significant advantages, which include: 1) a substantial increase in the OPA conversion efficiency, 2) avoidance of OPCPA gain roll-off in the pump pulse wings, i.e. the temporal equivalent of spectral gain narrowing, 3) increase of the OPA signal and idler pulse contrast as compared to the standard use of bell-shaped pump pulses whereby the chirped seed pulse is purposely overlapped only with a narrow temporal section of the pump around the pulse peak and the temporal wings of the pump pulse are responsible for raising the ASE (superfluorescence) background outside the temporal overlap with the seed pulse. Top-hat spatial profile beams can only be obtained at a specific distance from the laser source[91], because the beam profile is not an eigenmode of the diffraction equation and beam profile

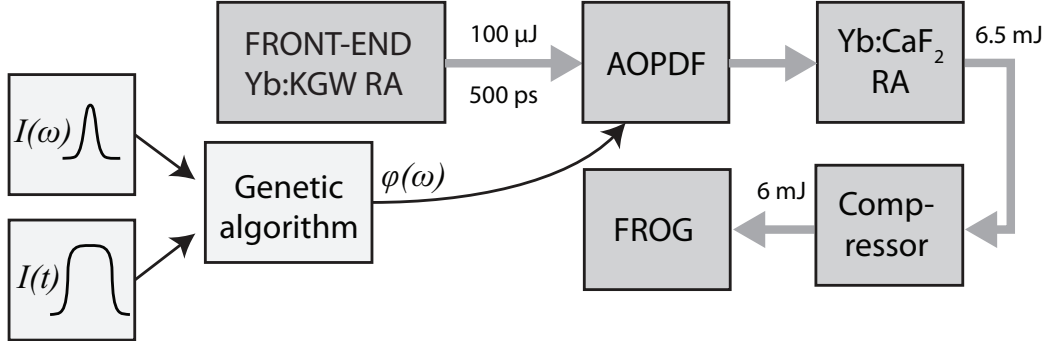


Figure 5.1: A general layout of the laser amplifier for the generation of top-hat temporal profile pulses.

changes significantly with propagation as a result. The situation is very different in the time domain. Unlike the spatial counterparts, top-hat temporal profile pulses can propagate arbitrarily long distances without changing the pulse profile in a dispersionless medium.

The method of choice relies on phase-only shaping, or chirping, of the pump pulse. Notably, the resultant carrier frequency variation in time is comparatively small and allows us to safely disregard any resultant temporal modulation of the phase mismatch in the OPA process. Crucially, the chirped pump pulses emitted by the femtosecond Yb amplifier can still be used for seeding the OPA/OPCPA system. This is achieved by splitting-off a micro-Joule-level 1030-nm pulse and passing it through a block of glass in order to recompress the pulse to a level sufficient for the generation of supercontinuum (OPA seed) radiation in a bulk crystal.

Previously, temporal gain flattening and energy extraction optimization in OPA [92] was demonstrated with electro-optically sliced nanosecond pump pulses and multiple staggered picosecond pulses shifted with respect to each other by controlled time delays [93]. Broadband Yb media, especially Yb:CaF₂ [94] which is suitable for high-energy operation with ≈ 200 -fs pulses and > 10 nm FWHM of bandwidth, are suitable for a simple phase shaping that can be implemented in a CPA scheme before the amplifier. Here a novel scheme for the generation of top-hat pulses is described. It is based on an acousto-optic programmable dispersion filter (AOPDF, DAZZLER) [95] included in an Yb:CaF₂ MOPA chain. We also demonstrate the seed generation for an OPCPA using recompressed pulses in a glass block.

5.1 Experimental setup

The general scheme of the laser system is shown in Figure 5.1. The laser system is a cascaded regenerative amplifier with a Yb:KGW MOPA as a front-end and Yb:CaF₂ regenerative amplifier (RA) as a power amplifier. The Yb:KGW RA is seeded by a Kerr-lens mode-locked oscillator based on the same gain medium and delivers $\approx 100 \mu\text{J}$ pulses at a tunable repetition rate. The pre-amplified pulses are then sent into another stretcher that additionally stretches the pulses so that the pulse duration in the final amplification stage is > 500 ps in order to reduce self-phase modulation in the amplifier. A very low quantum defect ($\approx 5\%$) allows reducing the thermal load on the crystal. The laser crystal is cryogenically cooled, which increases gain cross-section as well as improves thermal properties of the crystal leading to reduced thermal effects, such as thermal lensing and depolarization losses. The stretched pulses from the front-end are then sent through an AOPDF (DAZZLER, FastLite Ltd.) before amplification in the second amplifier. The length of the dazzler crystal is 25 mm, which allows applying approximately 3 ps variable group delay and supports pulse rep. rates up to several 10 kHz. Pulses are compressed in a reflection grating compressor in order to avoid self-phase modulation. The stretcher and compressor are matched so that when the AOPDF is removed, the pulses are compressed nearly to the Fourier limit. The bandwidth of the final pulses supports 150 fs pulse duration. The output energy of the amplified pulses is over 6 mJ. Noteworthy, the AOPDF phase-only shaping of the CPA seed pulses has virtually no effect on the amplification in Yb:CaF₂ because the seed introduced additional pulse chirping is negligible in comparison with the overall 500 ps pulse stretch imposed by the CPA system. Due to large chirp of the pulse in the CPA, amplitude modulation of the spectrum results in temporal intensity modulation of the pulse during the amplification and therefore the nonlinearities. The phase-only filtering allows efficient use of the laser gain medium bandwidth without changing operation regime of an existing CPA laser system.

5.2 Results

The top-hat pulse is obtained by imprinting a calculated spectral phase by an AOPDF. The spectral phase that transforms the initial pulse with given spectral intensity $I(\omega)$ into top-hat temporal profile $I(t)$ pulse is calculated using a genetic algorithm. The algorithm optimizes the spectral phase $\varphi(\omega)$ using provided measured spectral intensity $I(\omega)$ and target pulse shape $I(t)$ so that the r.m.s. difference between the target pulse shape $I(t)$ and the

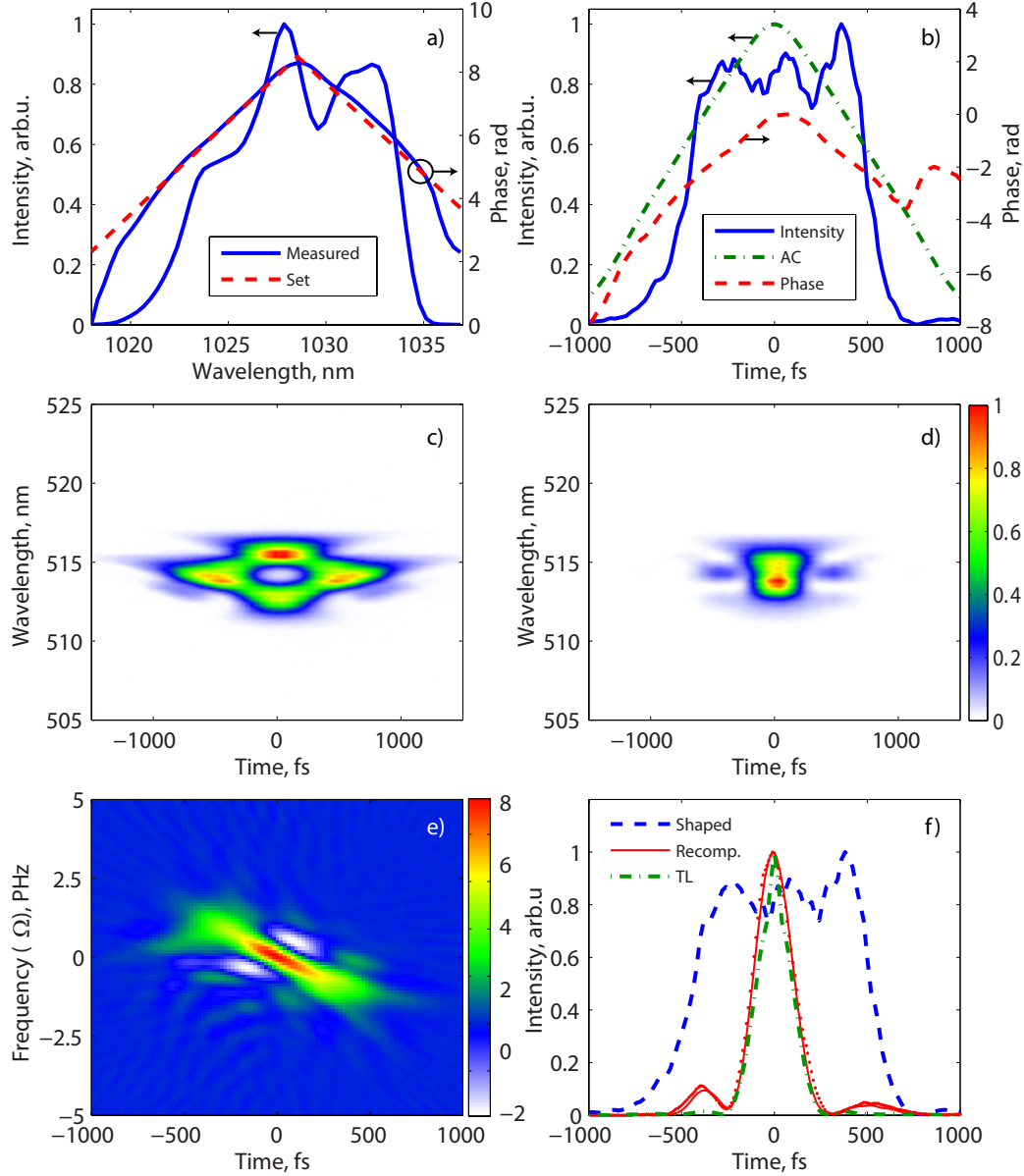


Figure 5.2: Temporal characterization of shaped pulses: a) spectral intensity and reconstructed phase. Dashed line shows the phase setting for the AOPDF shaper, b) reconstructed temporal profile of the pulse and temporal phase. For reference a second-order autocorrelation function of the rectangular pulse, c) and d) FROG traces of the shaped pulse and a recompressed pulse in a 30-cm long SF57 glass block respectively, e) calculated Wigner distribution of the measured rectangular pulse, f) measurement (red dots) and calculation (red line) of the recompression of the rectangular pulse in a bulk dispersive material. A 30 cm long SF57 block of glass was used. Green line shows the transform limited pulse shape and blue line is the initial rectangular pulse.

calculated temporal profile $\mathcal{F}\{I(\omega) \exp(\varphi(\omega))\}$ is minimal, here $\mathcal{F}\{\}$ denotes Fourier transformation. The target top-hat pulse shape $I(t)$ is approximated using a 6th-order super-Gaussian function $I(t) = \exp(-(t/\tau)^6)$. If the spectrum of the amplified laser pulse is symmetric, the optimal spectral phase is also symmetric and can be expressed as an even-order polynomial. However, for an arbitrary spectral shape, the spectral phase is asymmetric.

In order to check the concept and understand the optimal spectral phase shape better, a pulse splitting concept can be adopted similarly to the one that was used with picosecond pulses [93]. The transform limited pulse can be split into two replicas by setting different group delays for different spectral portions. A linear variation of spectral phase causes a group delay $\tau = d\phi/d\omega$. By splitting the spectrum into two parts with approximately equal total energy and setting the linear phase variation of the two parts with opposite signs of the slopes so that the pulse is split into two replicas separated by 2τ . For an appropriately chosen delay, the two pulses overlap to produce an approximately top-hat pulse shape. The idea was previously demonstrated using ultrabroadband pulses and a deformable mirror pulse shaper [96]. Here we show that even for much less broadband pulses from Yb:CaF₂ amplifier the similar method can be used with a compact AOPDF shaper.

The temporal profiles of the shaped and initial pulses were measured using SHG FROG (Figure 5.2 c) and d)). First a residual phase had to be measured and compensated with the AOPDF. Due to imperfect matching of the stretcher and compressor gratings (the groove densities were 1700 and 1750 lpmm respectively) and a rather large cumulative optical path in the RA amplifiers, there is some uncompensated high order spectral phase left after the compressor which distorts the temporal pulse profile. The measured residual phase was later taken into account for the optimal pulse shape calculation simply by subtracting the residual phase from the target phase profile. The measurement results are summarized in Figure 5.2. The applied spectral phase and the one retrieved from FROG match rather well as shown in panel a). The spectrum at the time of the measurement was rather modulated which causes modulation of the temporal profile of the shaped pulse as shown in Figure 5.2 b). The duration of the rectangular pulse at half intensity level is 1 ps. The reconstructed saw-tooth temporal phase exhibits two linear phase ramps with opposite sign. The slope of the temporal phase corresponds to instantaneous frequency $\omega(t) = d\phi/dt$, meaning that there is an abrupt jump of instantaneous frequency approximately in the center of the pulse. The rise and fall time of the rectangular pulse is mainly determined by the bandwidth of the laser pulse. Note that the chirp of the pump pulse has little effect on the phase of the amplified signal wave, although it can be

used to adjust the amplification bandwidth [97].

5.3 Pulse recompression for seed generation

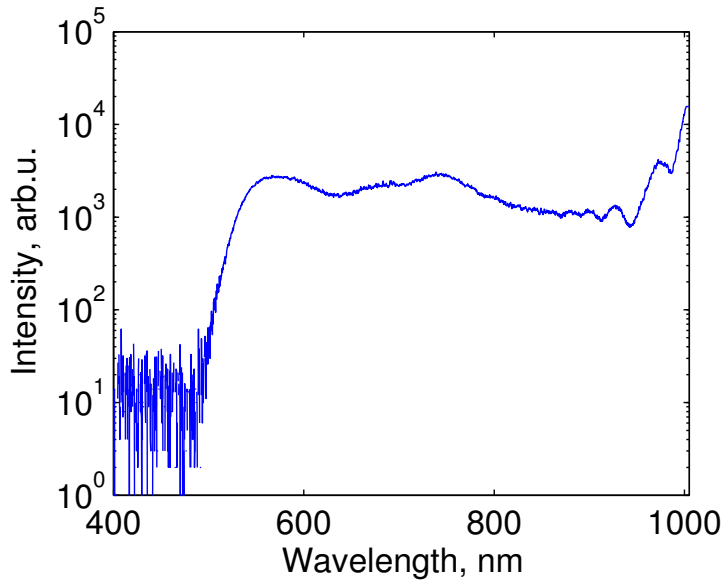


Figure 5.3: Supercontinuum spectrum generated using 1030 nm recompressed pulses. Only the short wavelength side of the spectrum is measured due to limitations of a silicon detector.

Another aspect in the context of OPA driving is the ability to seed it. The most attractive property of an OPA pumped by a femtosecond laser is the possibility to directly seed it with a spectrally broadened pulse obtained by supercontinuum generation using the same laser pulse [12]. In order to achieve efficient supercontinuum generation, a steep temporal intensity gradient $dI(t)/dt$ is needed. The top-hat pulses are not efficient for such spectral broadening, because the intensity is constant during the pulse therefore the frequency change is zero due to constant nonlinear phase $\phi_{nl} = n_2 I(t)$. The long exposure of the material to the high intensity tends to induce optical damage before reaching the intensity level required for spectral broadening [98]. We show that the shaped rectangular pulses can be transformed to a shorter pulse that is more efficient for the supercontinuum generation using just a simple block of material provided that the sign of the spectral phase is chosen correctly. The shaped top-hat pulses have the property that the pulses are chirped. If the spectral phase is chosen such that the spectral part

with higher frequency precedes the part with the lower frequency, as is the case shown in Figure 5.2, the negative chirp can be very well compensated by a positive dispersion glass block.

The shaped top-hat pulse was recompressed to 230 fs in a 30-cm long SF57 glass block which induces $\approx 4.4 \times 10^4$ fs² chirp. The calculated pulse profile from the initial top-hat pulse is in a good agreement with the FROG measurement. Despite some wings of the recompressed pulse that are due to residual uncompensated high-order phase, the pulse duration is very close to the transform limit and has a sharp peak. The white light supercontinuum generated in a bulk sapphire plate using the recompressed pulse spans beyond 500 nm as shown in Figure 5.3.

5.4 Summary and Outlook

In conclusion, the generation of top-hat pulses from Yb:CaF₂ MOPA amplifier were demonstrated. The system delivers up to 6.5 mJ pulses at 1 kHz and is scalable to a high average power due to the availability of high power laser diodes at 976 nm for direct diode pumping. The system is especially attractive for efficient amplification of ultrabroadband pulses in OPCPA. The idler can also be applied; however, in that case additional phase compensation should be used. The recompression of shaped top-hat pulses was demonstrated using a 30-cm long SF57 glass block which greatly simplifies the seeding of an OPCPA. When combined with a spatial top-hat profile, the scheme can greatly improve conversion efficiency of an OPCPA or second harmonic generation.

Chapter 6

Frequency tunable THz emission from laser-driven plasma

6.1 Introduction

Since the demonstration a decade earlier by Cook and Hochstrasser [42] of intense THz emission from air ionized with a two-colour ($\omega + 2\omega$) laser field, this phenomenon remains in the focus of attention. This is motivated by its potential as a source of intense single-cycle THz pulses, enabled by the high generated THz-field strength and large bandwidth and facilitated by the absence of material damage. The THz-range covers a wealth of fundamental resonances (in molecules: vibrational and rotational resonances, in solids: phonon and plasmon resonances, impurity transitions), which opens a wide field of possibilities for fundamental material and device research [99, 100] as well as possible sensor applications, including the identification of atmospheric pollutants and use in food quality-control, atmospheric and astrophysical remote sensing, and (medical) imaging with unique contrast mechanisms [101].

Another motivation is the complex underlying plasma dynamics leading to the THz emission. Both an $\omega - (2\omega - \omega)$ four-wave mixing mechanism based on stationary or nonstationary third-order susceptibilities [102], as well as a tunnel-ionization-induced micro-current mechanism [37, 103] have been considered. According to the electron current model, the THz emission from plasma originates from sharp quasi-periodic changes of free electron density occurring at the peaks of optical field ionization in the tunneling regime. The induced electron current rapidly varies on the sub-cycle time scale and yields generation of many harmonics, also known as Brunel harmonics [31, 32]. Similarly to HHG where the mixing of the laser driving field with its second

harmonic allows breaking the symmetry between the two quantum paths and yields generation of even harmonics [44], the THz emission can be considered an even (0^{th} -order) harmonic. This particular mechanism of THz emission is thus closely related to two prominent phenomena, Above Threshold Ionization (ATI) and High-order Harmonic Generation (HHG), also based on quasi-periodic sub-cycle ionization followed by electron acceleration in the driving laser field. High-order harmonics are generated via transitions of the electron between a continuum state and the ground state, which can be efficiently controlled on the single-atom and sub-cycle level [47, 48].

Here it is shown that the low-frequency THz emission corresponds to transitions between continuum states and can also be controlled by shaping the laser field. The semi-classical interpretation in terms of transient electron currents by Brunel [32] and Kim et al. [37] is recovered from quantum-mechanical continuum-continuum transition matrix elements using the Strong Field Approximation (SFA) with a stationary phase analysis. Furthermore, control over the timing of sub-cycle optical field ionization relative to the sign and value of the vector potential of the pulse [104] is experimentally demonstrated. This is achieved by fixing the carrier envelope phases (CEP) and detuning the frequencies of the two optical driving fields away from commensurability [105]. This results in a very wide continuous tunability of the THz frequency emitted by the laser-generated plasma.

This frequency dependence of THz emission received little attention as mostly the commensurate $\omega + 2\omega$ schemes have been used so far. Incommensurate frequency combinations have been realized by superimposing a broadband 20-fs pulse with its narrowband second harmonic; however the tunability range in this case is limited to the bandwidth of the fundamental [105]. Employing the relatively broad tuning range of the OPA, the initial evidence for the wide frequency-tunability of the THz-emission [40, 43] was obtained. Also, a scheme similar to our experimental setup based on a near-degenerate optical parametric amplifier (OPA) superimposed with the fundamental laser pulse has been implemented [106]. However, due to lack of CEP stabilization of the driving laser, field-resolved detection of the generated THz pulse was impossible. Furthermore, in that work only the lowest THz-frequencies (< 3 THz) and only very small detunings from the exact degenerate case have been considered.

Here, an incommensurate-two-colour scheme for THz generation is demonstrated, where the ratio ω_1/ω_2 is not an integer, based on a nearly degenerate OPA pumped by a CEP-stable Ytterbium-based laser emitting at 1030-nm wavelength. Inspired by our initial experiments [40, 43], we present extensive experimental data, theory and calculations that agree with the measurement data. The spectral properties of the generated THz emission is analyzed

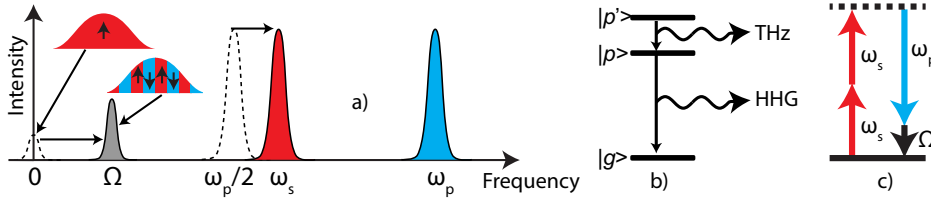


Figure 6.1: (a) Scheme of mixing two incommensurate frequencies for generating tunable THz emission. (b) Scheme of the atomic transitions in a strong laser field: transitions between a continuum and a ground state yield HHG, while transitions between continuum states yield low order harmonic generation (including THz). (c) Perturbative four-wave mixing scheme for THz generation.

over a wide range of detuning frequencies from the exact commensurate case. With the CEP stabilised input pulses we are able to generate CEP-locked THz pulses and detect them in a field-resolved measurement, thus demonstrating their applicability for time-domain spectroscopy probing the amplitude and phase response of a material. Due to the long wavelengths of the constituent colours (1030 nm and 1800–2060 nm), our scheme is a promising route for a high-efficiency [107], CEP-locked, broadband and widely tunable mid-IR/THz source.

6.2 Quantum mechanical transient electron-current model for THz emission

A proper quantum mechanical treatment of THz emission is desirable to support the commonly used semi-classical two-step model by Brunel [32] and Kim et al. [37]. A very successful fully quantum mechanical model that describes emission of an atom exposed to a strong laser field is based on the SFA [68], where the influence of the atomic potential on the electron in the continuum, as well as the influence of all bound states except the ground state are neglected. Recently full ab-initio quantum TDSE calculations were performed to calculate THz emission [38, 39], but the drawback is that the physical nature of the underlying dynamics is difficult to interpret. Here we use an analytical SFA model to calculate the atomic emission and derive the expressions that are identical to those previously attained in a classical description by Brunel of recollision-free harmonic emission.

An electron in a continuum interacting with the strong laser field can be described as a wavepacket, which propagates in phase space:

$$\Psi_c(t) = -i \int_0^t \hat{U}(t, t_b) \hat{V}_L(t_b) \hat{U}_0(t_b, 0) \Psi_0 dt', \quad (6.1)$$

where $\hat{U}_0(t_1, t_0)$ and $\hat{U}(t_1, t_0)$ are the field-free and full propagators between times t_0 and t_1 and the operator $V_L(t)$ describes the interaction with the laser field. Here the velocity gauge is used. The interpretation of Eq. 6.1, which has proven both very fruitful and accurate, is that t_b are the instants of strong-field ionization and $\Psi_c(t)$ is a superposition of many wavepackets emitted into continuum at times t_b . Calculations based on semi-classical wavepacket propagators or quantum-trajectories explicitly utilize this picture by representing quantum mechanical amplitudes as sums over contributions of wavepackets moving along classical trajectories [108]. Therefore, we express Eq. 6.1 as a sum over such wavepackets $\psi(r(t, t_b), t)$, emitted by the parent neutral system at times t_b and propagated to t :

$$\Psi_c = \sum_{t_b} \psi_{t_b} [r(t, t_b), t]. \quad (6.2)$$

Note that these equations are formulated for a linearly polarized laser field, so the electron dynamics are limited to a single dimension along that polarization direction.

The emission of electromagnetic radiation is proportional to the dipole acceleration, i.e. the time-derivative of the dipole velocity $\dot{d}_{cc}(t) \equiv \langle \Psi_c | \hat{p} | \Psi_c \rangle$, where $\hat{p} = i\nabla$ is the momentum operator (atomic units are used throughout the paper). With Eq. 6.2, the dipole velocity of the whole wavepacket is given by the sum of dipole velocities for all birth times: $\dot{d}_{cc}(t) = \sum_{t_{b1}, t_{b2}} \langle \psi_{t_{b2}} | \hat{p} | \psi_{t_{b1}} \rangle$. Expressing the wavefunction of the free electron born at instant t_b as a plane wave, $\psi_{t_b} [r(t, t_b), t] = \sqrt{\rho(t_b, t, r)} e^{iS(t_b, t, r)}$, where $S = pr - E(t - t_b)$ is the action and ρ is the electron density, it can be shown (see Appendix), that the diagonal terms ($t_{b1} = t_{b2}$) are the stationary points in phase space and thus dominate this sum. Wavepackets emitted at different times, $t_{b1} \neq t_{b2}$, are separated in space, i.e. have a reduced overlap and lead to rapid phase oscillations. We can thus simplify the dipole velocity to a single sum over birth instants:

$$\dot{d}_{cc}(t) = \sum_{t_b} \langle \psi_{t_b} | \hat{p} | \psi_{t_b} \rangle, \quad (6.3)$$

and express the continuum-continuum transition dipole velocity matrix elements as:

$$\langle \psi_{t_b} | \hat{p} | \psi_{t_b} \rangle = \int dr \rho(t_b, t, r) v(r, t, t_b) + \delta \dot{d}(t), \quad (6.4)$$

with the velocity $v = \partial S / \partial r$. Here, the first term describes the case when the wavepacket overlaps with itself and $\delta \dot{d}(t)$ provides corrections. These may arise if some wavepackets emitted at different times have met at some place in the phase space later.

This is an important difference as compared to HHG, where the continuum and bound parts of the two wavepackets evolve differently and accumulate a phase difference that depends on frequency and ultimately leads to chirped emission of attosecond pulses. In C-C transitions, however, the requirement for the wavepackets to overlap yields the Brunel harmonic radiation which is unchirped.

We now concentrate on the first term in Eq. 6.4 and rewrite:

$$\dot{d}_{cc}(t) = \sum_{t_b} \underbrace{\int \rho(t_b, t, r) dr}_{W(t, t_b)} \underbrace{\frac{\int \rho(t_b, t, r) v(r, t_b, t) dr}{\int \rho(t_b, t, r) dr}}_{\bar{v}(t, t_b)} = \sum_{t_b} W(t, t_b) \bar{v}(t, t_b) \quad (6.5)$$

as a sum over all ionization instants t_b of the product of $W(t, t_b)$, the norm of the wavepacket created at time t_b , and $\bar{v}(t, t_b)$, the average velocity of the wavepacket.

The wavepacket norm is time-independent and is given by the ionization probability at t_b : $W(t, t_b) = \Gamma(t_b) \delta t_b$, where δt_b is the saddle point region and Γ the instantaneous ionization rate. Thus we have:

$$\dot{d}_{cc}(t) = \sum_{t_b} \Gamma(t_b) \delta t_b \bar{v}(t, t_b) = \int^{t_b} \Gamma(t_b) \bar{v}(t, t_b) dt_b. \quad (6.6)$$

Here we see that $\dot{d}_{cc}(t)$ is the driving term for the Brunel harmonics [32] and would correspond to the current density in the quasi-classical model of Kim et al. [37] if multiplied by the atomic density in the generating medium. The emitted electromagnetic field is proportional to the dipole acceleration

$$\ddot{d}_{cc}(t) = \Gamma(t) \bar{v}(t_b = t; t) + \int^{t_b} \Gamma(t_b) \dot{\bar{v}}(t_b, t) dt_b. \quad (6.7)$$

The first term of this equation is proportional to the small initial velocity after tunneling: $\bar{v}(t_b = t; t) \approx 0$, which is neglected in the usual three-step picture, and the second one is the force $F[t, r(t, t_b)] = \dot{\bar{v}}(t_b, t)$ acting at time t on the wavepacket at the position $r(t, t_b)$ (center of mass of the wavepacket). The force is given mainly by the laser field and the Coulomb potential of the ion $F[t, r(t, t_b)] = F_{\text{las}}(t) + F_{\text{Coul}}[r(t, t_b)]$. In practice, the laser field usually dominates for electrons ionized in the strong-field regime, so the

dipole acceleration is simply given by:

$$\ddot{d}_{cc}(t) = F_{las}(t) \int^t \Gamma(t_b) dt_b. \quad (6.8)$$

The emission is simply proportional to the driving laser field multiplied by the ionization steps $\int^t \Gamma(t_b) dt_b$. The spectrum of the emission is obtained by Fourier transforming Eq. 6.8

$$\ddot{d}_{cc}(\omega) = F_{las}(\omega) \star \mathcal{F} \left[\int^t \Gamma(t_b) dt_b \right] (\omega), \quad (6.9)$$

which results in the convolution of the laser field spectrum and the spectrum of the ionization steps.

Now we apply the formalism derived above to the calculation of the emission spectrum in the case of a two-colour mixing scheme, which allows generation of even harmonics, including the THz sideband. Simulating our experimental conditions, the field in the calculation is composed of a strong fundamental wave at the frequency ω_p and a weaker signal wave at around half the frequency of the fundamental wave $E(t) = E_p(t)e^{i\omega_p t} + E_s(t)e^{i\omega_s t}$, where $E_p(t)$ and $E_s(t)$ are the envelopes of the pump and signal waves respectively. The direction in which the electron is emitted is given by the sign of the velocity $v_d(t_b) = \bar{v}(t \rightarrow \infty, t_b)$ at which the electron drifts after the laser pulse is over. Fig. 6.2 b) illustrates the asymmetric case of the two colour field where all of the electrons ultimately fly in one direction. The build-up of this directional electron current is responsible for the emission of the low-frequency-THz waves (see Fig. 6.2 c,d).

Tuning of the central frequency occurs when two incommensurate frequencies are mixed. This is illustrated in the right column of Fig. 6.2 for a $0.6\omega + \omega$ -combination, and compared to the commensurate case ($0.5\omega + \omega$) in the left column. While in the latter case, the growth of a directional net-current (Fig. 6.2b) leads to the emission of a low-THz-frequency field (Fig. 6.2c,d), the modulation of the current direction resulting from the detuning of the signal-frequency by $\Delta\omega$ leads to a $2\Delta\omega$ -shift of the center of the emitted THz-spectrum (Fig. 6.2g,h). The shift of lowest order sideband frequency is then compared to the experimentally measured THz-emission frequency. Higher order sidebands are beyond the EO sampling detection range and were not measured in this experiment.

This tunability is further analysed in Fig. 6.3 b). The THz-emission appears as a zeroth order sideband alongside higher-order sidebands [31]. The THz sideband starts close to zero frequency at degeneracy ($\omega_s = 0.5\omega_p$) and its frequency increases as the frequency of the signal wave is tuned. This effect

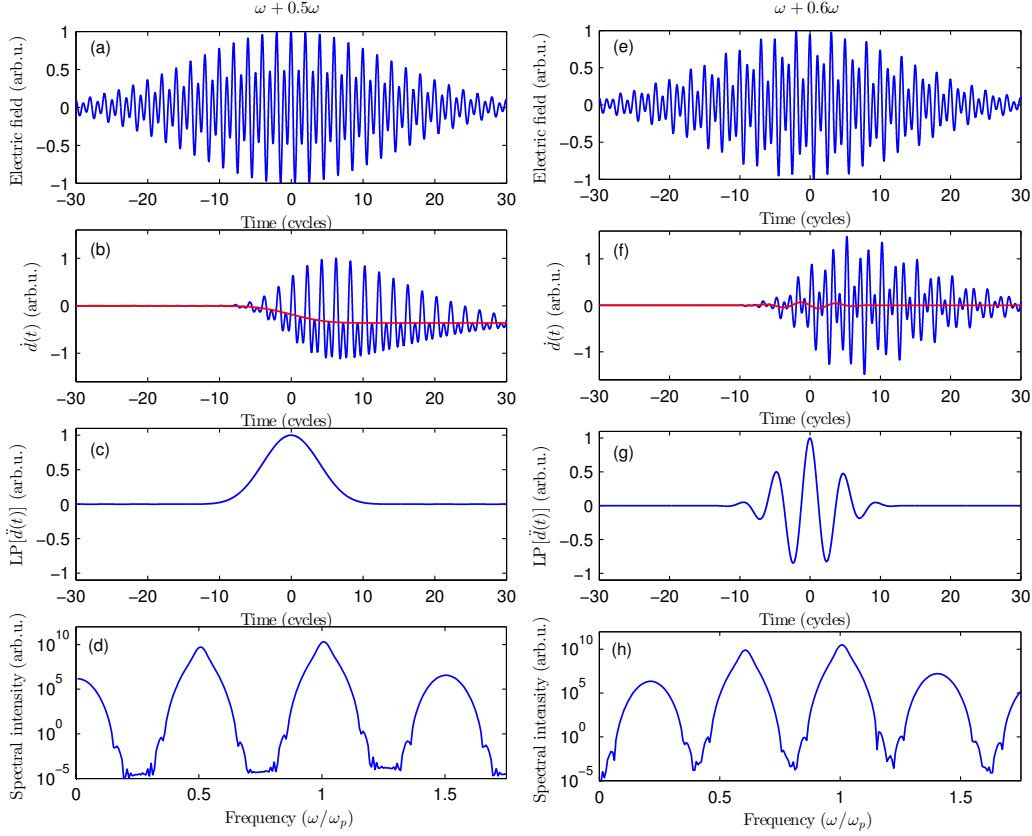


Figure 6.2: Simulation of the induced current, using Eqs. 6.6–6.9 with $\Gamma(t_b) = \exp[-2(2I_p)^{3/2}/(3|F_{\text{las}}(t_b)|)]$ and the classical expression $\bar{v}(t, t_b) = -\int_{t_b}^t F_{\text{las}}(t')dt'$, for two-colour fields with two frequency ratios: the left and right-hand sides correspond to the commensurate and incommensurate frequency case, respectively. Shown are the considered driving electric fields (first row), the dipole velocity (Eq. 6.6), corresponding to the induced current (second row, blue line; the red line shows a low-pass filtered version), the low-pass filtered (retaining only the THz-sideband) dipole acceleration (Eq. 6.8), corresponding to the emitted THz-field (third row), and the spectral intensity of the emitted radiation (square of Eq. 6.9) (fourth row). The considered ionization potential is that of nitrogen molecules, $I_p = 15.7$ eV. The ω_p -component of the driving field has a peak field strength of $F_{\text{max}} = 27$ GV/m (corresponding to 1×10^{14} W cm $^{-2}$), and the ω_s -component has $F_{\text{max}} = 13.5$ GV/m and a relative phase of $\pi/4$.

can be interpreted as a temporal phase modulation, shifting the THz sideband towards higher frequencies as illustrated in the inset of the Fig. 6.1a). Although the described THz emission mechanism is a phenomenon of intrinsically non-perturbative nonlinear optics, the resultant THz frequency tunability follows the law $\Omega = 2\omega_s - \omega_p$ (Fig. 6.3b), as is also the case in the perturbative four-wave mixing picture, illustrated in Fig 6.1c). We also predict the feasibility of generating weaker sidebands corresponding to 6, 8, etc. photon processes. This process clearly enables a tunability through the complete THz and mid-IR spectral regions [105].

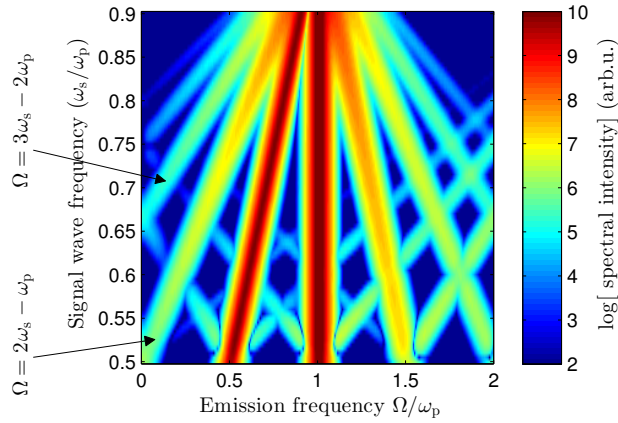


Figure 6.3: Simulated power spectrum of the emission (square of Eq. 6.9) as a function of the frequency ω_s of the tunable signal wave, for the same conditions as in figure 6.2.

6.3 Experimental implementation

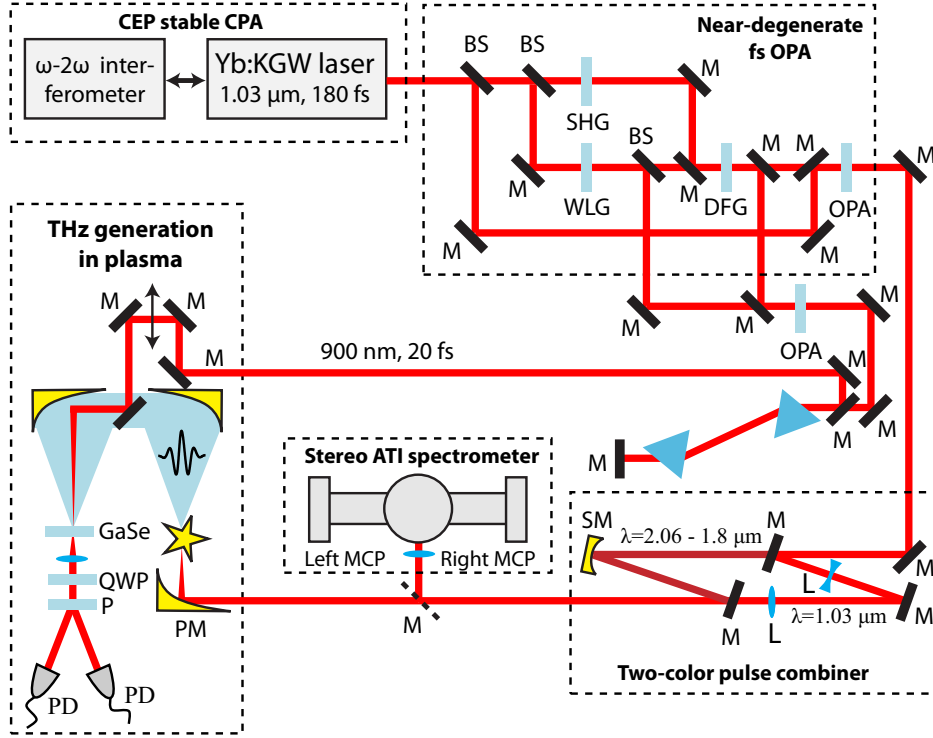


Figure 6.4: Scheme of the experimental setup. THz emission was detected via electrooptic (EO) sampling setup based on GaSe crystal. The probe pulses were generated in an additional OPA and compressed down to 20 fs in a prism compressor.

An Ytterbium-based laser amplifier and a near-degenerate OPA were used to generate two-colour pulses that were used for plasma excitation (Fig. 6.4). The Yb:KGW regenerative amplifier is actively CEP stabilized [67] and is used to pump a two-stage near-degenerate OPA. First, part of the laser energy is split into three parts. One part is used to generate a broadband super-continuum by focusing it in a sapphire plate. The part of the so-generated spectrum around 680–720 nm is used as a seed for the first OPA stage. The second part of the beam is frequency-doubled and serves as a pump for the first OPA stage. The resulting difference-frequency (idler) wave from the first stage (1800 nm to 2100 nm) is then amplified as a signal wave in the second OPA stage, pumped by the third part of the fundamental laser beam. The resulting CEP of the OPA output is thus equal to the pump laser pulse CEP phase [65], up to a constant: $\varphi_s = \varphi_p + \text{const.}$

At the output of the OPA, the pump wave at $\lambda_p = 1030$ nm and the signal wave at $\lambda_s = 1800$ – 2100 nm are separated using dichroic mirrors and then re-combined after adjusting the divergence of the beams and the relative delay. The polarization of each of the two colour-component pulses are linear and set parallel to each other. The phase delay between the two constituent colour waves is $\tau_\phi = \varphi_p(\lambda_s - \lambda_p)(2\pi c)^{-1} + \text{const.}$, and can thus be controlled via the fundamental laser CEP φ_p .

6.3.1 Observation of directional electron current

We verified that the two-colour pulses used for THz generation induce a directional electron drift by measuring the photoelectron spectra produced via above threshold ionization (ATI) with a stereo-ATI spectrometer [46, 36]. The electron spectrometer consists of a small xenon-filled gas cell (< 1 mbar) placed in a vacuum chamber with two identical time-of-flight (TOF) electron spectrometers oriented opposite each other in order to measure the photoelectron spectrum emitted in the opposite directions. The generated photo-electrons pass through small holes in the gas cell into the TOF arms. Each TOF arm consists of a field-free propagation tube (≈ 50 cm) and a micro-channel plate (MCP) electron detector. The linear polarization of each of the two-colour driving wave is in the direction of the TOF detectors. The signals from the two TOF detectors are then acquired with multi-scaler card and processed using a computer.

The ATI spectrum in one direction measured for different CEP phases of the laser pulse is shown in Fig. 6.5 a). This measurement is done with the OPA tuned at degeneracy ($\lambda_s = 2060$ nm) so that the maximum directional drift is produced, as illustrated in the left column of figure 6.2. The asymmetry of the low-energy direct electrons is opposite to that of high-energy rescattered electrons (not considered in figure 6.2) and partially reduces the asymmetry of the total electron yield. However, because the number of direct electrons is much higher than of the rescattered ones, the total yield still exhibits a modulation depth higher than 15%, as shown Fig. 6.5 b). These findings prove that in our experimental conditions, the induced electron current is highly directional and we are working in the tunneling regime, as assumed for the theoretical model.

6.3.2 CEP-locked, tunable THz emission

We now demonstrate the phase-locked temporal modulation of this induced electron current to achieve tunability of resulting CEP-locked THz emission.

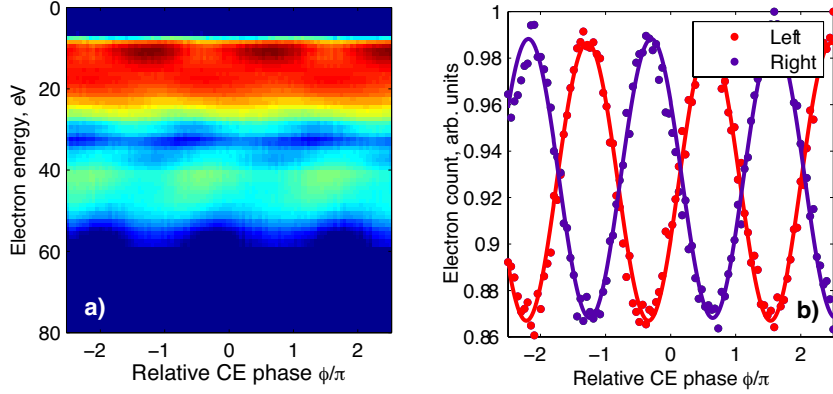


Figure 6.5: Stereo-ATI electron spectrometry measurement results obtained with two commensurate-frequency pulses: $\lambda_p = 1.03 \mu\text{m}$ and $\lambda_s = 2.06 \mu\text{m}$. (a) Electron energy spectrum (log scale) measured on one side of the stereo-ATI spectrometer as function of the fundamental laser CEP. (b) Total electron count in left and right directions of the stereo-ATI spectrometer obtained by integrating the electron spectrum of the left and right detectors.

For THz-generation, the combined two-colour driving waveform is focused using an $f = 7.5 \text{ cm}$ parabolic mirror into ambient air. The field of the generated THz radiation is detected using electro-optic (EO) sampling. In general, the bandwidth f_{max} in the EO sampling detection scheme depends on the probe pulse duration $f_{\text{max}} \approx 1/(2\tau_{\text{probe}})$ and it is the main limitation in our setup. The probe pulse of $\tau_{\text{probe}} \approx 20 \text{ fs}$ duration was generated by amplifying the spectral portion at around 900 nm of the white-light super continuum in a separate OPA stage and then compressing the pulse in a prism compressor near transform limit (see figure 6.4). The probe pulse was characterised using SHG Frequency Resolved Optical Gating (FROG) with the result shown in Fig. 6.6.

The phase of the THz wave according to the frequency dependence is $\varphi_{\text{THz}} = 2\varphi_s - \varphi_p$. Therefore, the degenerate scheme where fundamental and frequency-doubled pulses are mixed (with CEPs $\varphi_{2\omega} = 2\varphi_\omega + \text{const.}$) provides a passive stabilization of the THz-pulse's CEP, ($\varphi_{\text{THz}} = 2\varphi_\omega - \varphi_{2\omega} = \text{const.}$), similar to difference-frequency generation based on a second-order nonlinearity (χ^2) [65]. Since in our case, $\varphi_s = \varphi_p + \text{const.}$, the CEP of the THz-pulse is the same as that of the fundamental laser pulse: $\varphi_{\text{THz}} = \varphi_p + \text{const.}$ Because of the field-sensitive EO sampling of the THz emission, active stabilization of the laser CEP is thus mandatory. In other words, for non-CEP-stabilized driving pulses, the THz emission is still emitted, but their CEP is random from pulse to pulse.

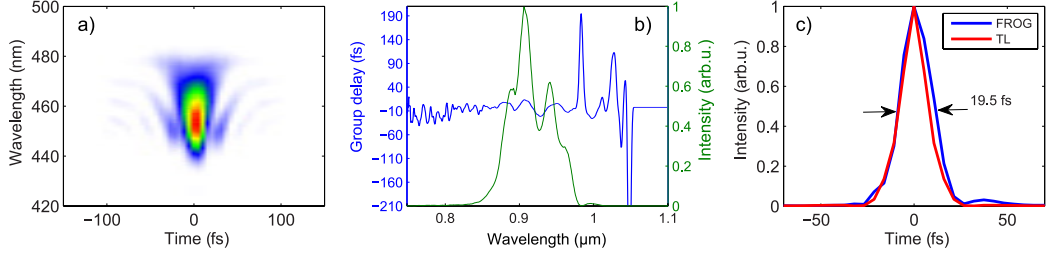


Figure 6.6: Temporal characterisation of EO sampling probe pulse using SHG FROG. a) measured FROG trace, b) reconstructed spectrum and group delay of the pulse c) measured temporal profile and calculated Fourier limit.

This is why, as shown in Fig. 6.7a), without active CEP stabilization of the laser pulse, the emitted THz waveforms for each laser pulse are averaged out in our EO sampling. By locking the laser CEP, we create reproducible THz fields that let us study the two-colour-driven plasma dynamics.

The detected THz emission spectra as function of the signal wavelength $\lambda_s \leq 2\lambda_p$ are shown in Fig. 6.7 b). Despite the rather narrow bandwidth of our 180-fs pulses that were used to excite the plasma, mid-IR emission frequencies up to ≈ 40 THz were measured as the result of detuning the OPA from degeneracy. The frequency of the THz-sideband shifts towards higher frequencies due to temporal current modulation when the OPA is detuned from degeneracy, as illustrated by the numerical simulations shown in figure 6.2. We can detect only the lowest THz-sideband in the spectrum due to the limited bandwidth of the THz detection apparatus. At higher frequencies, the probe pulse duration is significantly longer than the half-cycle of the field to be measured. The decreasing sensitivity of the THz detection setup at higher frequencies also contributes to the broadening of the spectrum for higher frequency detuning. The experimentally obtained frequency dependence agrees well with the semi-classical transient electron-current model simulations in figures 6.2 and 6.3: we observe a shift by $\approx \Delta\nu$ for a signal wavelength tuned to $\omega_s = (\omega_p + \Delta\nu)/2$.

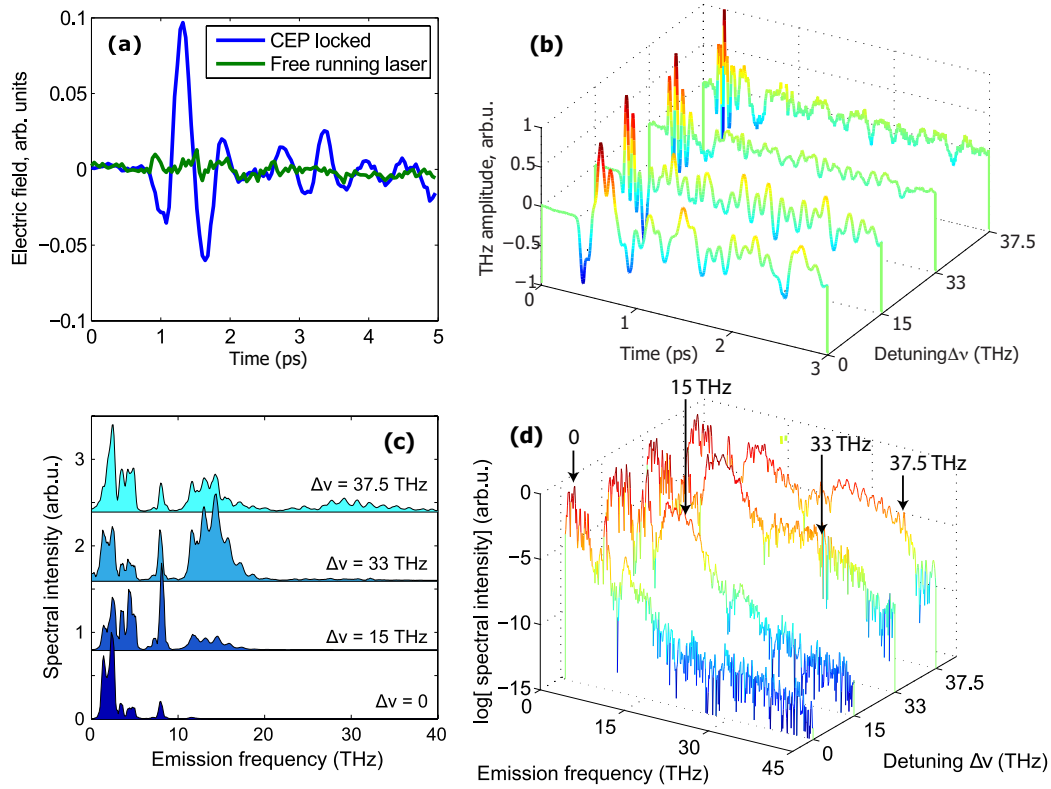


Figure 6.7: Experimental THz-generation results with $\omega_p + \omega_s$ two-colour driving fields ($\omega_s = (\omega_p + \Delta\nu)/2$), for various detunings $\Delta\nu$, created by combining the fundamental wave ($\lambda_p = 1.03 \mu\text{m}$, $250 \mu\text{J}$) with the tunable signal wave ($\lambda_s = [2.06, 1.96, 1.84, 1.80] \mu\text{m}$, $20 \mu\text{J}$). (a) Electric field of the THz transient measured using EO sampling in case of locked CEP or free running laser, for zero detuning, $\Delta\nu = 0$, i.e. exactly commensurate frequency ratio. (b) Temporal traces of the EO sampling signal for different detunings $\Delta\nu$, (c) THz emission spectra of plasma calculated from the EO signal, represented on linear scale. (d) The same spectra as in (c), represented on logarithmic scale. Each spectrum and temporal trace was normalised to its maximum. The arrows in panel (d) show the theoretically predicted central frequency of the emission.

6.4 Summary

The tunability and CEP-stability of the THz emission from a laser-induced plasma-spark is demonstrated by mixing two incommensurate CEP-stable optical driving fields, forming a parametric waveform synthesizer producing shot-to-shot reproducible strong-field multi-colour waveforms. The measured frequency dependence of the THz emission is consistent with the commonly used transient electron current model. We have derived this model here for the first time from continuum-continuum transition matrix elements in a fully quantum-mechanical treatment.

Chapter 7

Pulse post-compression using Kagome lattice fibres

Waveguide-based pulse post-compression is a traditional technique for broadening the bandwidth of injected pulses, enabling subsequent recompression to a few-cycle duration. Solid-core single-mode fibers are well suited for single-cycle pulse compression at nJ energy levels [109]. In the 1 – 10 mJ-level energy range, hollow-core gas-filled glass capillaries with a bore diameter of several hundred μm are routinely used for the generation of 3 – 5-fs pulses [110]. Despite the success of both the solid and hollow-core waveguides, there are no satisfactory solutions for 5 fs pulse compression at the intermediate, 1–50- μJ energy level, which is the regime of many modern high-repetition rate MHz laser systems serving a variety of applications in ultrafast spectroscopy, micro-fabrication, etc. The main problem lies in the scalability of the hollow-core technique as the reduction of the core diameter leads to rapidly mounting transmission losses that scale as $\alpha \propto a^{-3}$. Consequently, low power-handling capacity of small-core capillaries limits the pulse repetition rate to tens of kHz. Hollow-core photonic crystal fibers (HC-PCF) [111] offer an elegant way out to maintain an adequate pulse intensity at low energies to ensure efficient spectral broadening. However, due to a limited band gap size, band-gap guided HC-PCFs support a narrow bandwidth insufficient for few-cycle pulse generation. The bandwidth restriction was recently overcome by employing a Kagome lattice, which resulted in fibers with a very large guidance bandwidth, low dispersion [112], exceptionally low optical loss, and high damage threshold [113], see Figure 7.1. Here an efficient broadening of Yb laser amplifier pulses in a Kagome lattice HC-PCF is numerically modeled and experimentally demonstrated. The experiments validate the expectation that Kagome fibers are highly suited for converting rather long femtosecond pulses from various modern Yb DPSS and YDFA

sources into octave-spanning continua with the prospect of re-compressing them into single-digit femtosecond pulses.



Figure 7.1: A SEM image of Kagome lattice HC-PCF. The name “Kagome” is composed from the words *kago*, meaning "basket", and *me*, meaning "eye" and it comes from a traditional Japanese woven bamboo pattern that is used to make baskets.

7.1 Nonlinear propagation calculation

The estimations of dispersion profile and nonlinear pulse propagation simulations are presented here in order to better understand the regime of pulse compression in Kagome fibres and optimize the experimental parameters such as gas pressure, fibre length and input pulse energy. The goal is to check the limits of spectral broadening of 200-fs input pulses that is achievable using a simple model that includes SPM and an approximate dispersion profile of the waveguide. The simulations show that compression down to a few-cycle regime should be possible as described in the subsequent sections below.

Nonlinear pulse propagation was simulated by solving nonlinear Schrödinger equation using 1D split-step algorithm. The pulse propagation is described using the following equation:

$$\frac{\partial U}{\partial \xi} + \frac{i}{2} \frac{\partial^2 U}{\partial \tau^2} - \frac{L_D}{6L'_D} \frac{\partial^3 U}{\partial \tau^3} - i \frac{L_D}{L_{NL}} |U|^2 U = 0, \quad (7.1)$$

where $\tau = t/T_0$, $L_D = T_0^2/\beta_2$ and $L'_D = T_0^3/\beta_3$. The pulse duration parameter $T_0 = 77$ fs was chosen to match 200 fs FWHM Gaussian pulse centered at $\lambda = 1.03 \mu\text{m}$.

7.1.1 Waveguide dispersion of the Kagome fibre

First, the waveguide dispersion was estimated by approximating it with the dispersion of a corresponding diameter capillary and adding gas dispersion at different pressures. The second and third order dispersion terms as well as dispersion lengths for different Argon pressures are shown in Figure 7.2. The capillary inner hole diameter used in the simulations is $40 \mu\text{m}$ and the duration $\tau_{fwhm} = 200$ of the input laser pulse was chosen according to the experimental conditions. At these relatively high pressures that can be used in the experiments the dispersion of gas becomes comparable or even stronger than the waveguide dispersion allowing the tunability of zero-GVD wavelength towards longer wavelengths. Third order dispersion term contribution is important as well and increases with increasing wavelength.

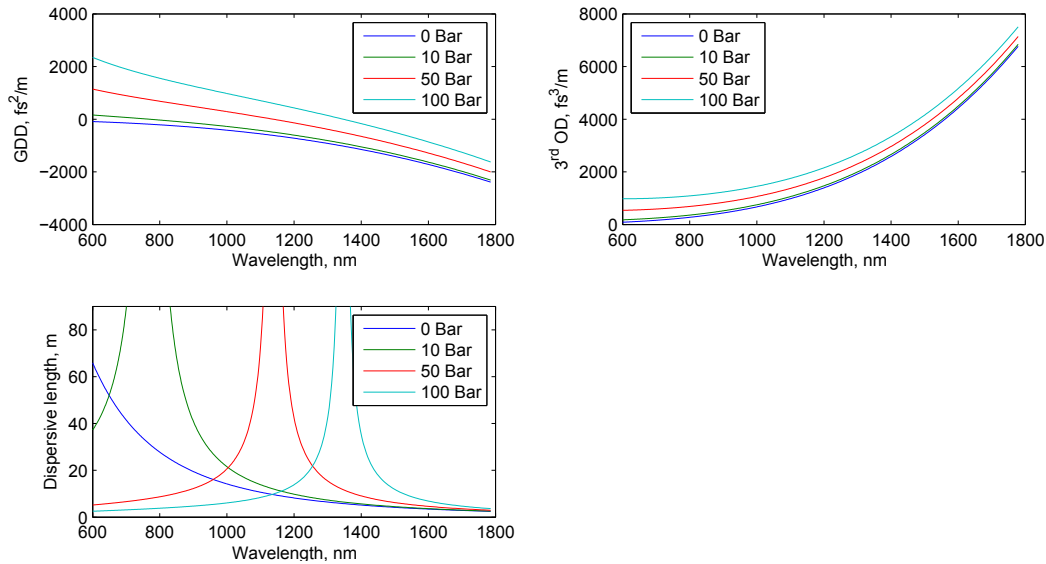


Figure 7.2: Calculation of second- and third-order dispersion of a Argon filled waveguides for different pressures.

7.1.2 Short fibre case

First, pulse spectrum broadening in a relatively short fibre (0.5m-long) was calculated for 100 bar Argon case. Since ionization effects on pulse propagation are neglected in these calculations, all the noble gases are comparable and only the dispersion is affected by the gas type and pressure. From the dispersion calculation data presented above, GVD $\beta_2 = 895 \text{ fs}^2/\text{m}$ and third order dispersion $\beta_3 = 1530 \text{ fs}^3/\text{m}$ values were used for pulse propagation sim-

ulations. Results are summarized in Figures 7.3 and 7.4. One notable trend is the red shifting of the broadened spectrum. This is most likely due to decreasing GVD of the combined fibre and gas dispersion at longer wavelength which keeps the longer wavelength part of the pulse short and allows further broadening. Such red-shift of the spectrum is consistent with the experimental data for high pressure of Krypton and Argon described in Section 7.2. Another notable effect is the transformation of a Gaussian input pulse into an approximately top-hat profile at higher input pulse energies.

These simplistic simulations indicate that clean SPM broadening down to few-cycle regime should be possible. Low, but non-negligible positive dispersion of the high-pressure filled fibre smoothens the spectrum of the broadened pulse.

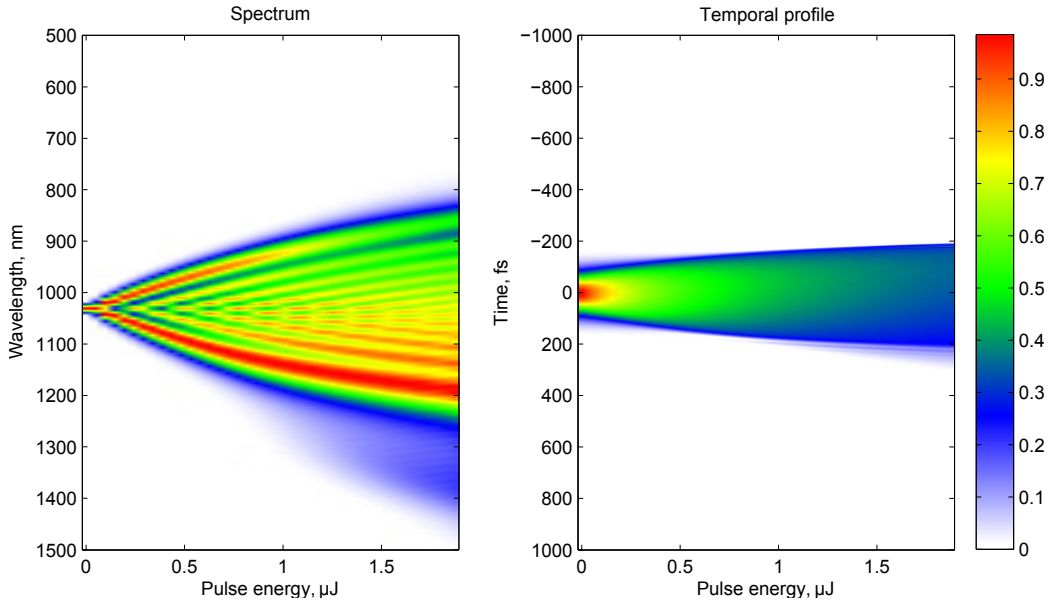


Figure 7.3: Calculated pulse spectrum and temporal profile as a function of input pulse energy at the output of 0.5 m long fiber filled with 100 bar Argon. Note that each spectra on the left graph are normalized to its maximum value for better visibility. The temporal profile graph on the right is not re-normalized because the intensity variation is not so strong.

Pulse spectrum and temporal profile evolution over the fiber length at 2 μJ input pulse energy is shown in Figure 7.4. The broadening slows down at $z \approx 25$ cm. After that the modulation of the spectrum becomes less pronounced, the center of the spectrum shifts towards red side and a weak wing at 1.3 – 1.4 μm starts appearing. Temporal profile also exhibits an increased rate of broadening at $z \approx 25$ cm.

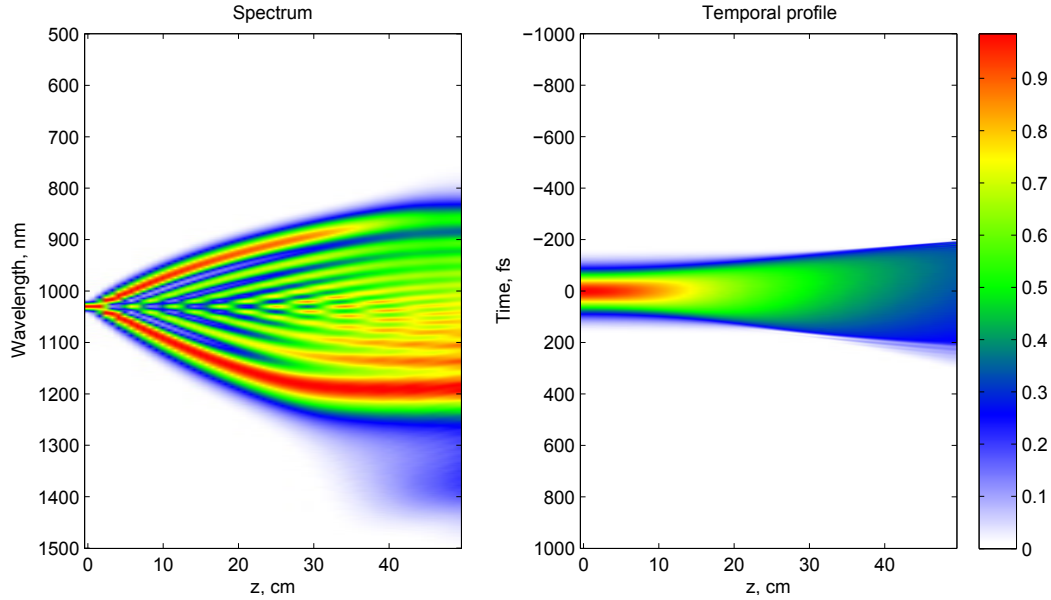


Figure 7.4: Spectral and temporal pulse profile evolution during propagation over 0.5 m long fibre. Input pulse energy $E_p = 2 \mu\text{J}$.

7.1.3 Long fibre case

The second set of calculations was done for a 2.5 m long fibre and lower input pulse energies, results are shown in Figures 7.5 and 7.6. The spectrum still exhibits a monotonic broadening with increasing input energy and the pulse energies are much lower as compared to 0.5m-long fibre case. The difference, however, is that the pulse duration is much longer and increases with increasing input pulse energy due to strong dispersive pulse broadening. The dynamics of the propagation over distance shown in Figure 7.6 is now more complex. In the first ≈ 0.5 m distance the spectral width increases nearly linearly, similarly to the short fibre case. Then broadening saturates because pulse duration gets longer due to increasing chirp. Finally, the infrared part of the spectrum which corresponds to nearly zero or negative dispersion regime continues to grow.

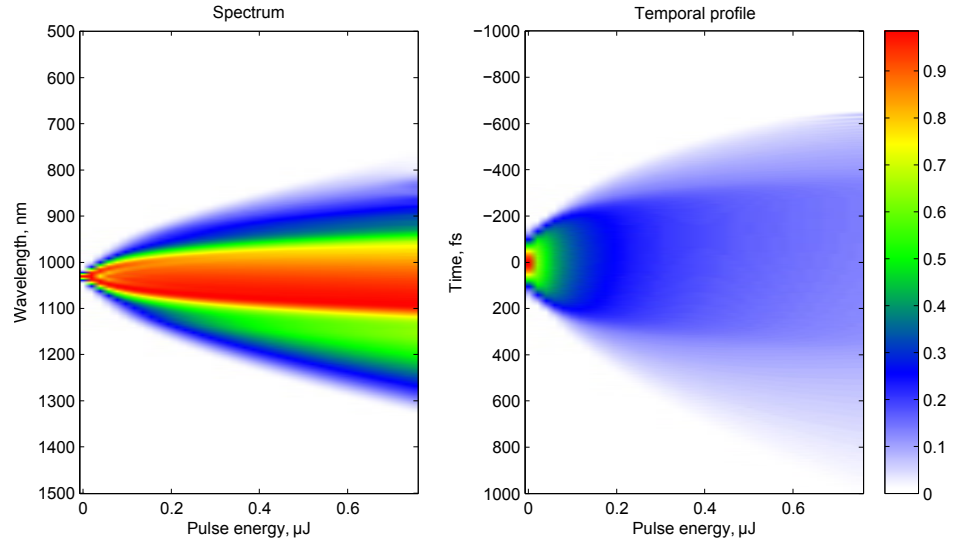


Figure 7.5: Pulse spectrum and temporal profile dependence on input pulse energy for 2.5 m long fiber, 100 bar Argon. Here also each spectra on the left graph are normalized to its maximum value for better visibility. The temporal profile graph on the right is not re-normalized.

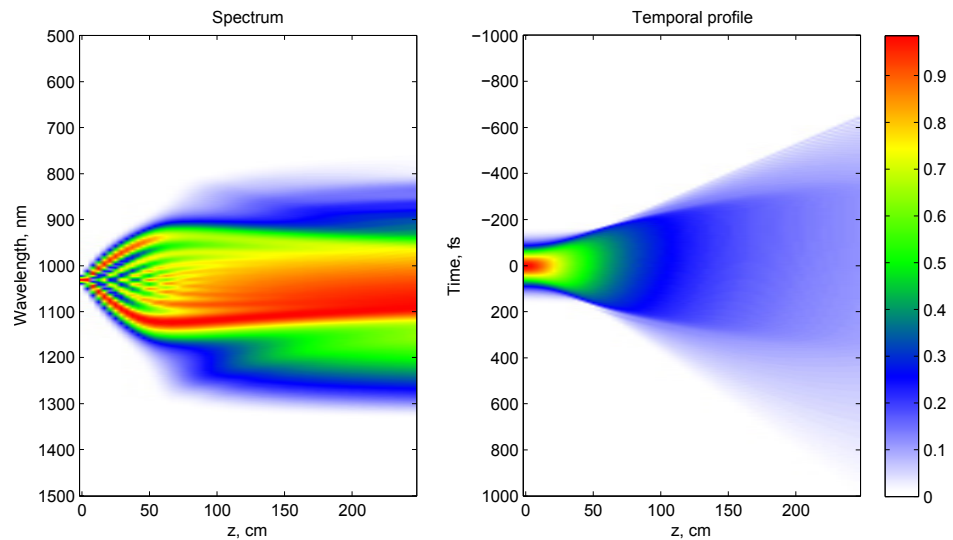


Figure 7.6: Spectral and temporal pulse profile evolution in a 2.5 m long fibre. Input pulse energy $E_p = 0.8 \mu\text{J}$. Each spectra on the left graph are normalized to its maximum value, while the temporal profile graph on the right is not re-normalized.

7.2 Experimental results

As a model source for testing pulse broadening, a sub-mJ 180-fs 10 kHz repetition rate Yb:CaF₂ CPA is used. The 75-cm-long fiber with inner core diameter of around 30 μm was filled with Krypton. Pulse energies up to 16 μJ were used in the experiment. The damage threshold of the fibre was observed at around 35 μJ . The spectrum measurements of the supercontinuum were done using optical spectrum analyzer which has approximately flat spectral response. In comparison to the previous experiments where longer pulses of energies up to 1 μJ were used [114], the laser source used in this experiment allows achieving a much higher peak power and enables generation of octave-spanning supercontinuum.

The the spectral measurements were done using optical spectrum analyzer (OSA) which has approximately flat spectral response. The pulse compression of the laser was optimized by installing an acousto-optic pulse shaper (DAZZLER), the retrieved pulse shape is shown in Fig. 7.7. The FWHM input pulse duration is 190 fs and the temporal profile is rather clean from high order phase.

However, input pulses contain some side pulses separated by a long delay of the order of several 10s of ps due to etalon effects in the amplifier. Due to these pre/post pulses the measured spectra of the broadened pulses have a strong peak which has approximately the shape of the fundamental spectrum of the pulse as it is described in section 7.2.2. Such structure should not be present in the case of pure SPM broadening. This peak in the spectrum can be related to the low pulse contrast of the system. Figure 7.7 d) shows the retrieved pulse from a FROG trace where a very wide time window was used for the measurement. One can see that the amount of energy outside the main peak is approximately 15%. Upon broadening the energy of the main peak is distributed in a broad spectrum, while the pre- and post-pulses have low intensity and are almost not broadened. This shows up in the spectrum as a sharp peak near the fundamental frequency which contain approximately the same amount of energy as these side pulses. These sidebands are due to etalon effects in the amplifier and in principle could be suppressed to some extent by optimizing the optical element quality in the regenerative amplifier cavity. An alternative source of high contrast femtosecond pulses is an OPA which generates pulses clean from these side pulses because of temporal cleaning due nonlinearity of the white-light supercontinuum seed and is a way to perform a very clean spectral broadening measurements. Spectral broadening results using IR OPA source are described in chapter 8.

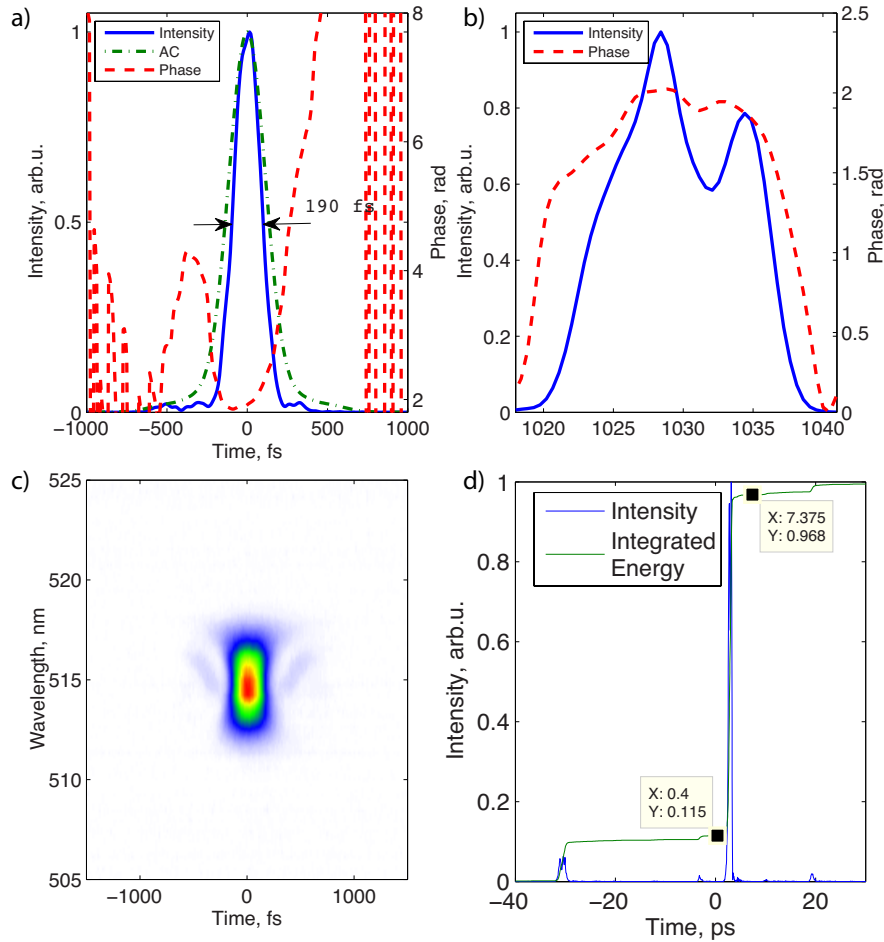


Figure 7.7: Input laser pulse FROG measurement. a) temporal profile, b) spectrum, c) FROG trace, d) retrieved pulse shape from a 100 ps wide time window FROG scan. The integrated energy in the sidebands is approximately 15%.

Below are shown the measured spectra for 0.75m fibre length, different gases (Argon and Krypton) at different pressures. The spectra are normalized to the total energy by dividing by the integral over the whole spectrum.

7.2.1 Spectral broadening results in Argon

Figures 7.8 and 7.9 show the pulse energy dependent spectra for different pressures of Argon. The general behavior can be roughly summarized as follows. First, for low pressures the spectrum simply broadens symmetrically toward long and short wavelength sides due to SPM. Second, after increasing

the pressure to 15 bar at approximately 12 μJ energy, a very broad spectral wing appears in the visible spectral range. This very broad spectral wing carries relatively low energy content of the pulse. Together with this short wavelength wing also a peak in the infrared side of the spectrum appears, approximately at 1300 nm, which is marked as (1) in Figure 7.8. With increasing pressure the generation threshold of the visible wing decreases. At around 20 bar pressure one can see that the intensity of the IR side-band decreases and the visible side becomes very weak. At 25 bar the central wavelength of the IR bump at 1.3 μm is increasing with increasing energy and at even higher pressures it totally disappears.

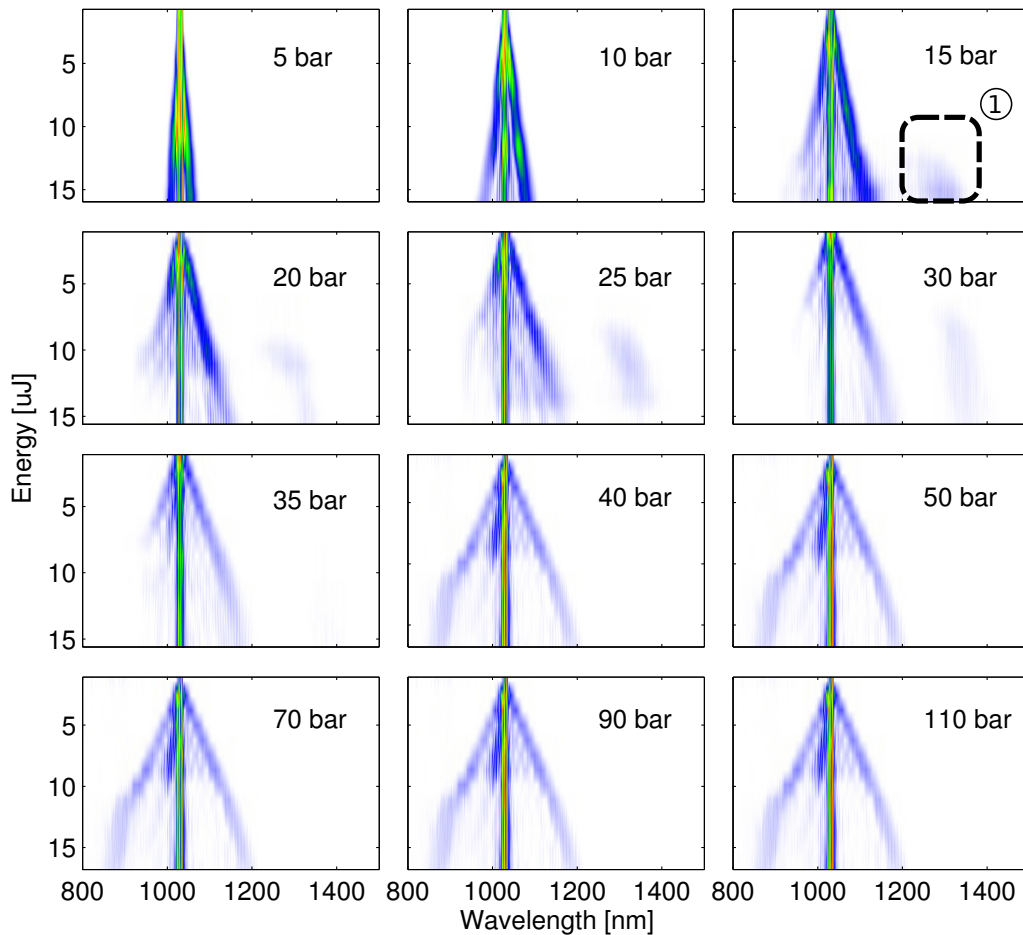


Figure 7.8: Spectral broadening in 0.75m long Kagome fiber filled with Argon at different pressures. Spectra are shown in linear intensity scale. (1) shows the appearance of a maximum in the long-wavelength range.

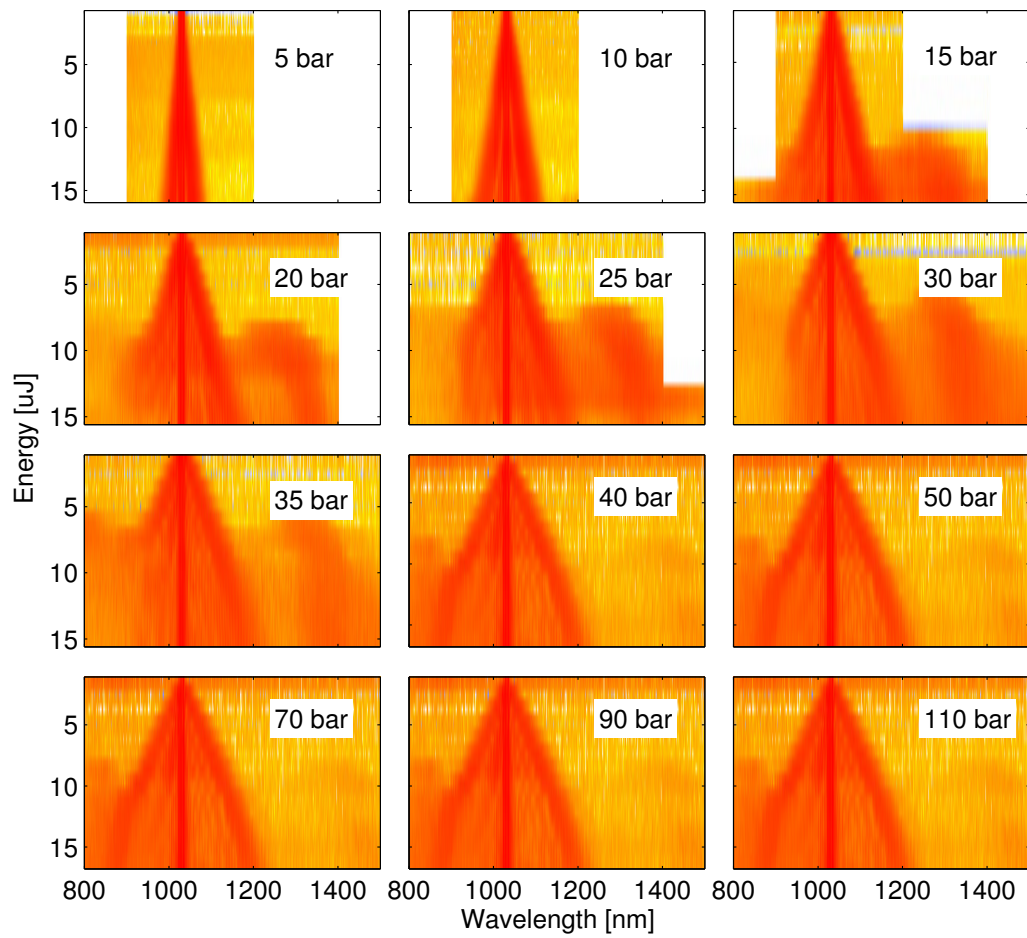


Figure 7.9: Pulse spectra shown in Figure 7.8 but displayed in logarithmic intensity scale. Fiber filled with argon, fibre length 0.75 m.

7.2.2 Spectral broadening results in Krypton

In order to obtain broad smooth spectrum of the pulse, a positive substantial dispersion is needed. This can be achieved using higher dispersion gas at high pressure. Figures 7.10 and 7.11 show energy-dependent supercontinuum spectra for different Krypton pressures and input pulse energies. First, for low pressures the spectrum simply broadens symmetrically around the input spectrum toward the long and short wavelength sides due to self-phase modulation [115]. At the gas pressure of 10 bar at approximately 12 μJ input pulse energy a broad spectral wing in the visible part of the spectrum appears. It spans down to the short wavelength side of the transmission band at around 500 nm, although the energy contained in this spectral wing is very low as compared to the total pulse energy. Simultaneously with the appearance of the short-wavelength wing, there also emerges an infrared sideband at approximately 1300 nm denoted by (4) in Figure 7.11 (a). With increasing the pressure, the threshold for the generation of the visible wing decreases. At around 20 bar pressure, the intensity of the IR side-band decreases and the visible side becomes very weak. At 25 bar, the central wavelength of the IR sideband around 1300 nm is progressively red-shifted with increasing energy. At even higher pressures, this band becomes unnoticeable.

Pulse broadening dynamics are mainly determined by the total group velocity dispersion of the waveguide and the gas. Figure 7.11 (b) shows the approximated GVD of the waveguide tunable by changing the Krypton pressure. For very low pressures, the driving laser wavelength falls into the weak negative dispersion regime. The optimal regime for the pulse post-compression is an SPM broadening in the positive dispersion regime with the dispersion length $L_D = \tau^2/|\beta_2|$ chosen to approximately fit the fiber length. Owing to a relatively strong polarizability of Krypton, the zero GVD point at 15 bar is shifted to the driving laser wavelength and at 35 bar pressure the dispersion is already strongly positive and favors efficient SPM spectral broadening. Due to higher polarizability of Krypton as compared to Argon, similar broadening regime is achieved at lower gas pressures. For example 30 bar of Krypton somewhat resembles the regime of 110 bar in Argon. Figure 7.11 (b) shows the spectrum corresponding to the maximum extent of the spectral broadening obtained. The bandwidth supports pulses as short as 2 fs assuming that the phase is compressible. The energy in the main pulse is over 80%, the long pedestal that contains the remaining energy can be attributed to the input pulse contrast. Upon spectral broadening, the energy of the main peak is distributed in a broad spectrum, while the pre- and post-pulses have low intensity and are almost not broadened. This shows up in the spectrum as a sharp peak near the fundamental frequency

which contain approximately the same amount of energy as these side pulses.

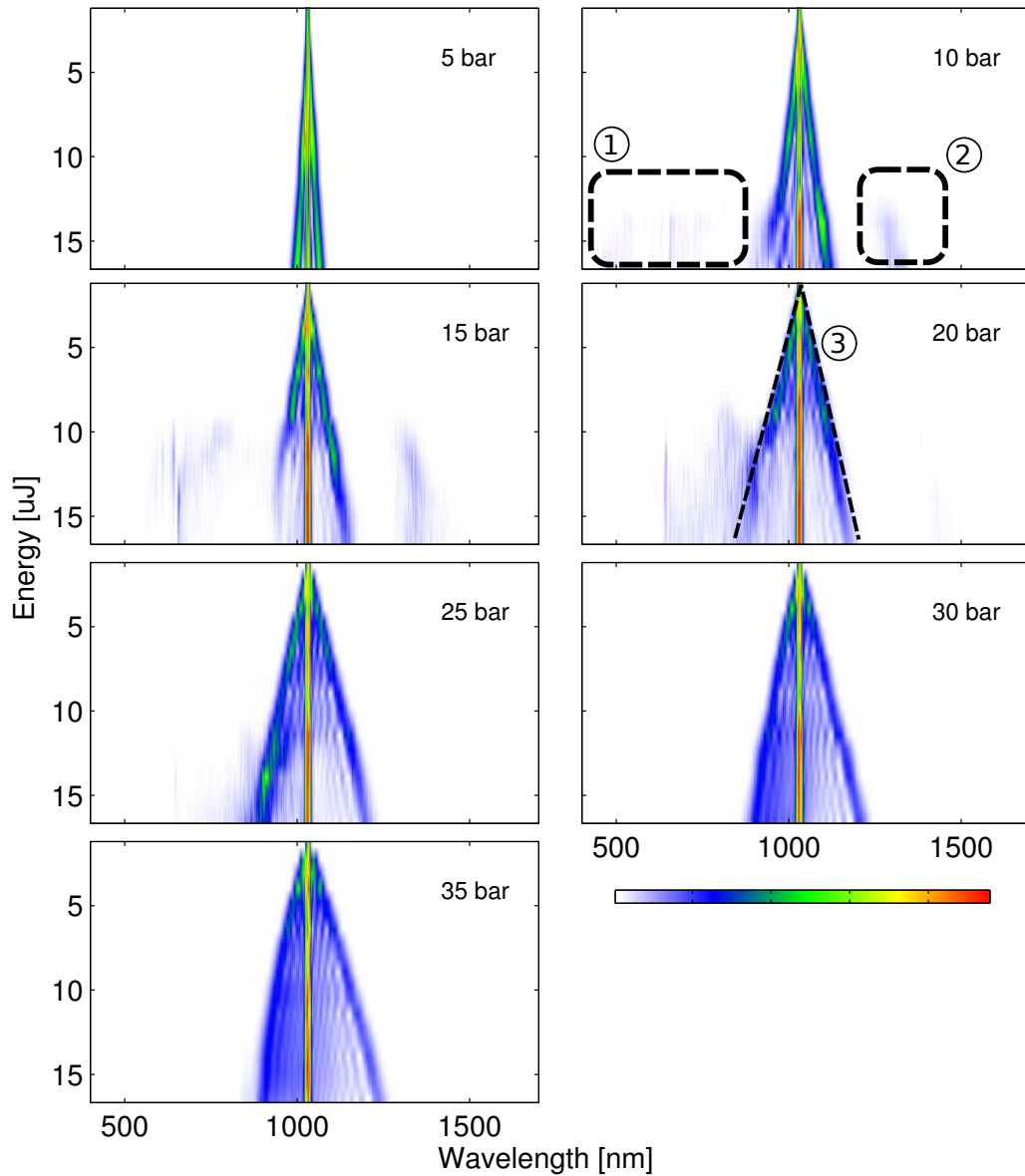


Figure 7.10: Pulse spectrum broadening results in Krypton, fibre length 0.75 m, linear intensity scale. (1) shows the abrupt appearance of an extremely wide spectral wing, (2) shows the appearance of a maximum in the long-wavelength side, (3) shows that initially the broadening follows the typical conical SPM structure, while at higher energies the shape is totally different.

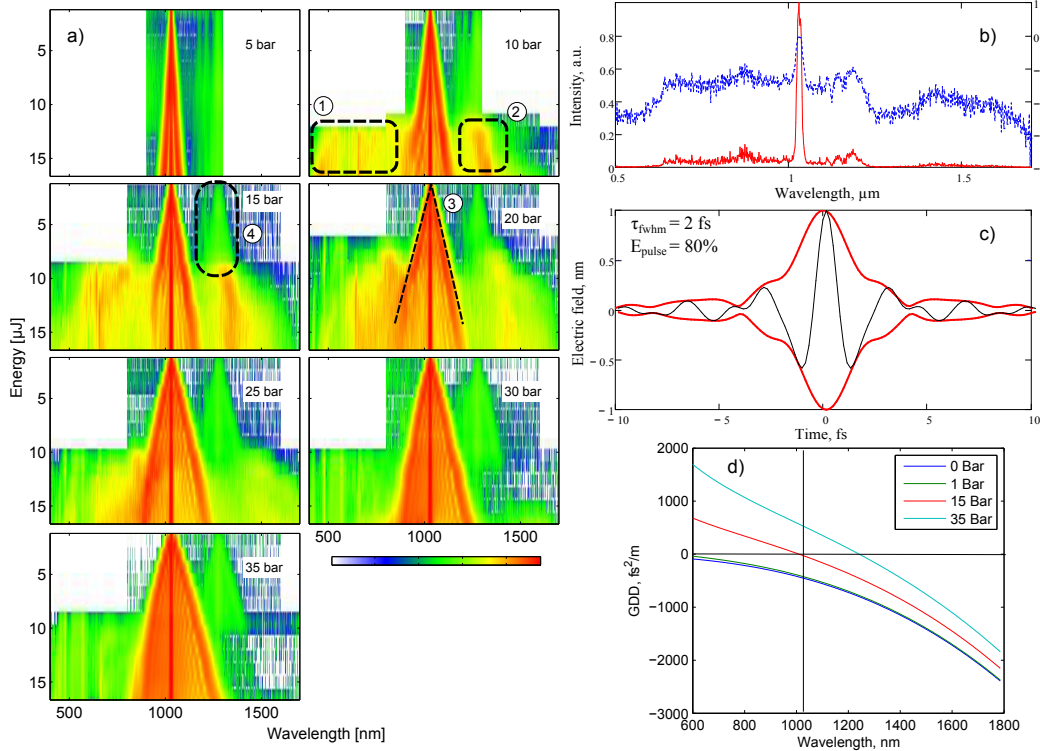


Figure 7.11: a) Dependence of supercontinuum spectrum at different pulse energies and Krypton gas pressures. Color code is shown on a logarithmic scale. Blank areas are due to different scanning ranges of the spectrometer used during the measurement. Feature (1) shows the abrupt appearance of an extremely wide spectral wing, (2) shows the appearance of a maximum in the long-wavelength side, (3) shows that initially the broadening follows the typical conical SPM structure, while at higher energies the shape is totally different, (4) a bump in the spectrum at 1.3 μm is also visible even before visible light generation starts. b) spectrum measured at 35 bar pressure and 16 μJ pulse energy. c) corresponding temporal profile of the transform limited pulse, d) waveguide dispersion at different gas pressures.

A spectrum for the transform-limited pulse duration calculation shown in Fig. 7.12 was taken from the data set shown in Fig. 7.10. The bandwidth supports pulses as short as 2 fs, although one still needs to check how compressible it is. The energy in the main pulse is over 80%, the long pedestal that contains the remaining energy can be attributed to the limited input pulse contrast.

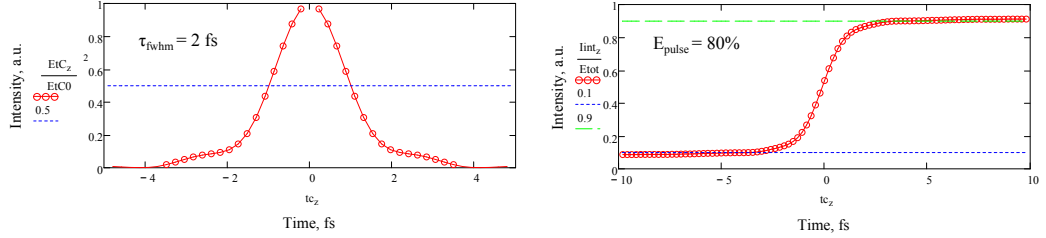


Figure 7.12: Left panel: transform-limited pulse duration calculation from spectrum broadened in 0.75 m long fibre filled with 20 bar Krypton. Input pulse energy is 16 μJ . Right: corresponding calculation of the energy contained in the main pulse by integrating the over the time axis and normalizing the total pulse energy to unity. The 0.1 offset at the edges of the integral shown on the right indicate that $2 \times 0.1 = 20\%$ of the total pulse energy is outside the main pulse.

7.3 Solitonic self-compression

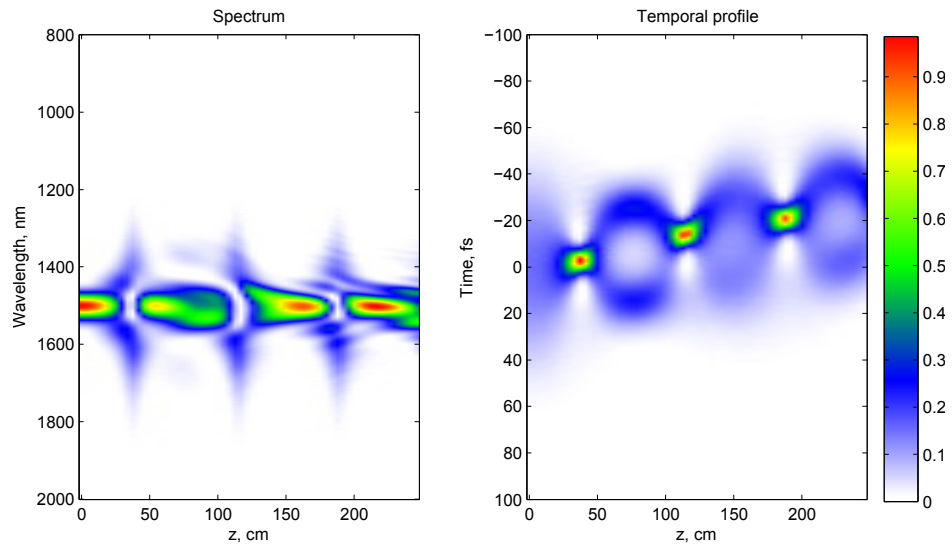


Figure 7.13: Solitonic pulse self-compression in the anomalous dispersion regime of Kagome fibre. Input pulse energy $E_p = 17 \mu\text{J}$, pulse duration $\tau_{fwhm} = 100 \text{ fs}$, center wavelength $\lambda = 1.5 \mu\text{m}$.

A totally different post-compression regime, the so-called solitonic self-compression, happens in the negative dispersion region of the transmission spectral window of the waveguide. An in-depth analysis, measurements and applications

using post-compressed pulses in this regime is discussed in Chapter 8. Calculation results of propagation of 100-fs long pulse centered at $\lambda = 1.5 \mu\text{m}$ through a fibre filled with 1 bar of Argon is shown in Figure 7.13. These parameters were chosen to approximately match that of the pulses from a typical KTA crystal based OPA pumped by a femtosecond Yb CPA laser. The pulse compresses in time and its spectrum widens at a distance of $z \approx 0.5$ m. Second $\beta_2 = -1400 \text{ fs}^2/\text{m}$ and third $\beta_3 = 3500 \text{ fs}^3/\text{m}$ order dispersion which is dominated by the waveguide dispersion at this pressure was included in the calculation and the input pulse energy corresponding to the N=3 order soliton was used. The third order dispersion yields the slant visible in the temporal profile evolution and distortion of the spectrum for higher solitonic compression revivals.

7.4 Summary

In this chapter an octave spanning supercontinuum generation in a Kagome lattice HCPCF in the high power regime is described. Kagome fibre has a very broad transmission bandwidth, low loss and intermediate mode diameter. The scheme allows extending pulse post-compression schemes down to the few-cycle duration at a high repetition rates.

Chapter 8

Sub-Cycle Gigawatt Peak Power Pulses Self-Compressed by Optical Shock Waves

In this chapter a scalable pulse self-compression scheme is presented that uses Kagome photonic crystal fibre with a large hollow core filled with a noble gas as a nonlinear optical medium [116]. The scheme is based on a modified solitonic regime in which an optical shock wave enhances temporal focusing and the energy buildup in the temporally focused part of the pulse proceeds to an unconventionally high level. The enhanced solitonic compression scenario is enabled by a fortunate combination of the wave guiding mechanism, optical nonlinearities and dispersion properties of a hypocycloid core Kagome-lattice hollow-core photonic crystal fibre (HC-PCF) [112]. We show both experimentally and theoretically, that, in a single step, ultra-short infrared pulses with energies of several tens of microjoules undergo a 20-fold nonlinear self-compression to reach a sub-cycle duration and a gigawatt peak power at the fibre exit. These results represent a radical improvement, both in terms of peak-power levels and compression efficiency, compared to all previously reported pulse self-compression schemes regardless of their type and geometry, be it free-space or waveguide [117].

The ability of ultrashort laser pulses to self-compress in negative dispersion waveguides is widely known since the observation of the optical soliton over 30 years ago [118]. Solid-core photonic crystal fibres are particularly well suited for accurate dispersion shaping and controlled solitonic self-compression [119, 120], but they are not scalable for high-energy operation as the correct dispersion profile generally corresponds to tiny core diameters. Secondly, the material damage threshold sets a severe limit on the maximum pulse energy [113]. Gas-filled capillaries permit high energy

throughput and are routinely used for mJ level few-cycle pulse generation [26], but the negative dispersion is weak and is usually overtaken by the positive dispersion of the gas thus preventing self-compression. Finally, the advent of photonic bandgap (PBG) guiding hollow-core photonic crystal fibre [111] showed promise to overcome these limitations of hollow capillaries following the pioneering demonstration of megawatt peak power solitons in this type of fibres [117]. However, restrictions originating in the photonic bandgap guiding mechanism and intrinsic problems of the HC-PCF performance have imposed difficulties in terms of a limited transmission bandwidth, high dispersion slope, and multimode structure [121] thus hampering the quest for nonlinear compression of high energy broadband pulses. The advent of HC-PCF with inhibited coupling between guiding channels created a new paradigm in optical guidance whereby core guided modes could cohabitate with cladding modes with no significant interaction between the two types of modes [122]. Unlike the earlier photonic bandgap guided HC-PCF, the ones with inhibited coupling [123] stand out with a significantly larger bandwidth, lower dispersion and higher power handling, opening the opportunity to reach very high intensities capable of ionizing the gas in the fibre core [115, 124]. Shockwaves are widespread in nature and generally lead to generation of extremely sharp features in time. Here we show that the optical shocks of sub-cycle duration [125, 126] can be generated experimentally in a single guided-photonics structure. We exploit the latest advances in the inhibited coupling guiding HC-PCF design that have led to a lower transmission loss and a smaller power fraction propagating inside the glass walls [113], much improved single-mode operation [112], and a controllable negative dispersion. We identify and experimentally demonstrate a new regime of optical pulse compression, in which an optical shock wave, arising as a part of the highly nonlinear guided-wave evolution of an ultrashort laser pulse, enhances solitonic pulse compression. Sub-cycle field waveforms, generated as a result of this dynamics, combine the most striking features of optical shock waves on the one hand and solitons on the other. Most crucially from the viewpoint of practical high-intensity applications, this unique combination of solitonic and shock-wave phenomena was achieved at intensity and peak power levels higher than 10^{14} W/cm² and gigawatt respectively, which are unprecedentedly high for an optical fibre. Remarkably, this dynamics takes place in a wave-guided manner, in the single-cycle self-compression limit and a single mode fashion. A further practical attribute is the scalability of this regime in both pulse energy and wavelength. Finally, by refocusing the self-compressed 10^{14} W/cm² beam from the fibre, the scheme can serve as a source for strong field applications. We employ above-threshold-ionization (ATI) of Xe atoms in a stereo time-of-flight spectrometer [46, 36] to act, firstly, as a

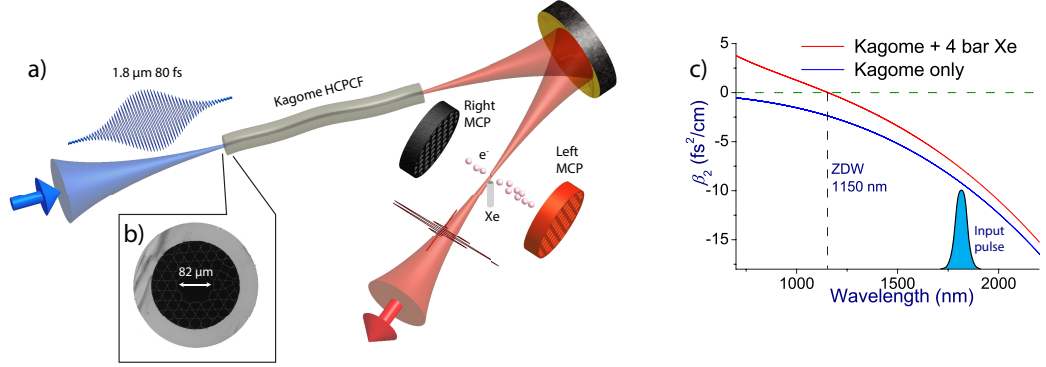


Figure 8.1: Pulse self-compression scheme based on Inhibited Coupling guiding HCPCF and the field measurement using stereo ATI photoelectron spectrometry. a) The experiment consists of launching infrared 80-fs pulses with energies of up to $120 \mu\text{J}$ into 0.2 meter long hypocycloid-core Kagome HCPCF with an inner-circle of $82 \mu\text{m}$ (corresponding to a mode-field diameter of $\approx 64 \mu\text{m}$). The pulses were generated in an optical parametric amplifier, and which wavelengths were tuneable in the $\approx 1.4 - 1.9 \mu\text{m}$. The fibre shown in the inset b) was optimized for this spectral range, exhibiting a linear loss of $\approx 70 \text{ dB/km}$ [113] and an S shaped dispersion curve over 1000 nm-2000 nm optical bandwidth and featuring anomalous dispersion ranging from 0 to 0.5 ps/km/nm within the spectral range of 1150-2000 nm. The solitonic self-compression in the negative dispersion regime is achieved by filling the fibre with Xenon to a pressure of 4 bar so to provide the necessary optical nonlinearity. At such a low pressure, the dispersion is dominated by the negative dispersion of the waveguide as shown in panel c).

practical demonstrator that the output pulses lays in the strong-field regime, and as a full electric field characterization tool of the generated pulses, which allowed a preliminary verification of the carrier envelope phase stability of the solitonically self-compressed pulses.

Figure 8.1 illustrates the uniquely simple Kagome-fibre-based pulse post-compression scheme. Input 80-fs pulses centred at 1800 nm are launched into a negative dispersion waveguide where they undergo self-compression. The Kagome fibre is placed inside a high-pressure gas cell capped on the output side with a quartz window that is only 0.1 mm thick to minimize distortions of the out-coupled self-compressed pulse. To eliminate additional dispersive broadening, only reflective optics is used downstream for conventional and ATI-based pulse characterization. Complete temporal, spectral and spatial characterization of the input and output laser waveforms was performed us-

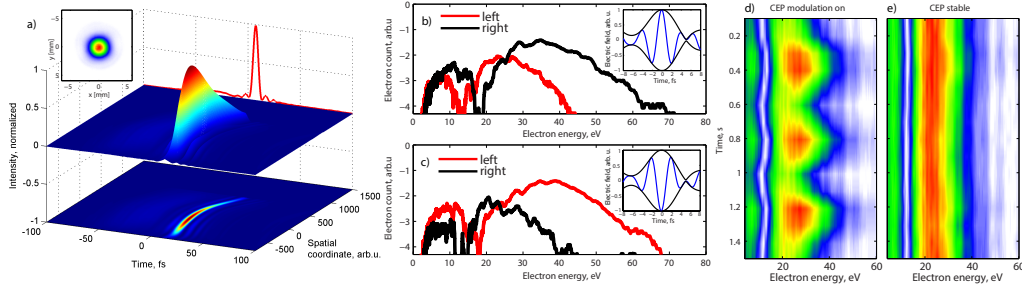


Figure 8.2: The spatial uniformity and whole-beam compression is illustrated in the spatio-temporal reconstruction of the pulse depicted in panel a) and measured beam profile shown in the inset. The panel b) and c) shows the photoelectron spectrum of ionized Xe atoms in two directions in Stereo-ATI spectrometer using self-compressed pulses for $+\cos$ and $-\cos$ electric fields. The panels d) and e) show that the self-compressed pulses retain the CEP phase of the much longer input pulses despite the very high compression ratio. The CEP of the input pulses was locked and the dependence of the electron spectrum was measured when the CEP of the laser is d) modulated with a linear phase ramp scanned with the speed of 12 rad/s and e) kept stabilized.

ing the technique of spatially encoded spectral phase interferometry for direct electric-field reconstruction (SEA SPIDER). Key results of the SEA SPIDER and stereo ATI measurements of the self-compressed pulses are presented in Fig. 8.2. The experimentally obtained spatio-temporal pulse intensity distribution shown in Fig. 8.2a proves that the self-compression mechanism is indeed active across the entire beam cross-section and is not limited to its central portion—one of the key strengths of the demonstrated method for nonlinear pulse compression of high-energy pulses. Figure 8.2b and 8.2c shows ATI spectra obtained for different CEP settings (with a phase difference of π) of the $60 \mu\text{J}$ output pulses obtained when the cell is filled with 1 bar of Ar. The dramatic asymmetry in the flux of the photo-ionized electron outgoing in the direction of the highest-intensity half-cycle of the laser pulse serves as a direct proof that the electric field of the pulse carries but a single dominant half-cycle. Using the procedure described in section 8.4, the measured stereo ATI spectra allow us to calibrate the CEP values and the actual peak intensity, $5 \times 10^{13} \text{ W/cm}^2$, that was reached in the ATI apparatus. By engaging an active CEP lock on the laser pumping the IR OPA that supplies 1800 nm input pulses we were also able to verify that CEP stability is preserved in the self-compressed output pulses as confirmed by an ATI measurement shown in Fig. 8.3d and e.

An experimentally measured as well as a numerically modelled evolution of output pulse temporal and spectral profiles after the propagation in the HC-PCF is shown in Figure 8.3 as a function of input pulse energy. The dynamics reveal pulse self-compression in a negative dispersion fibre down to sub-cycle duration. FROG and SEA-SPIDER techniques were used to characterize the initial stages of the self-compression down to few-cycle regime to independently confirm the same result (see section 8.1 for details). However, with the spectra ultimately spreading into the multi-octave range, only the SEA-SPIDER technique remained adequate pulse characterization in the single-cycle regime. As a consequence of the over-an-octave bandwidth, the red and blue wings of the spectrum exhibit significantly different divergence, with longer-wavelength components diverging faster than the blue ones. For the pulse components near the beam axis, the faster loss of the spectral content in the red wing amounts to an effective pulse broadening in time. To limit such spectral filtering caused by different beam divergences, we used a spherical mirror to re-image the output of the fibre onto the sum-frequency crystal and onto the ATI gas target as sketched in Fig. 8.1a. Re-imaging of the fibre output mode on the target effectively reconstitutes all the spectral components and allows formation of a sub-cycle pulse that otherwise would have been purged to a full cycle pulse known to be the limit for a free-propagating pulse as a consequence of the Gauss theorem. Because the ionization regime can be reached by the self-compressed pulse inside the Kagome waveguide itself, the energy of the single-cycle pulse critically depends on the choice of noble gas. The highest output pulse energy, $75 \mu\text{J}$, was reached for Ar because of its high ionization potential. These pulses were capable of driving the ATI apparatus (Fig. 8.2b,c) although their duration was not as short as in the case of Xenon gas.

The highest quality self-compression results, summarized in Fig. 8.3, were achieved for the gas with the highest non-linearity, Xe. As a consequence of its lower ionization potential, we had to restrict the maximum usable input energy to $35 \mu\text{J}$ resulting in the highest output energy of $25 \mu\text{J}$ corresponding to a sub-cycle pulse. These sub-cycle pulses result from an original sequence. As demonstrated in Fig. 8.3, at low input pulse energies, the pulse starts to shorten due to the interplay between the negative group velocity dispersion (GVD) and the self-phase modulation (SPM). At progressively higher input pulse energies, the nonlinear spectral broadening is increased and the resultant pulse duration is reduced approximately linearly with the pulse energy, as depicted in Fig. 8.3d). Starting with energies around $26 \mu\text{J}$ a needle-like structure emerges on the pulse. Subsequent dynamics differs significantly from the conventional high order solitonic pattern because the pulse continues to shorten instead of breaking up. Numerical modeling convincingly

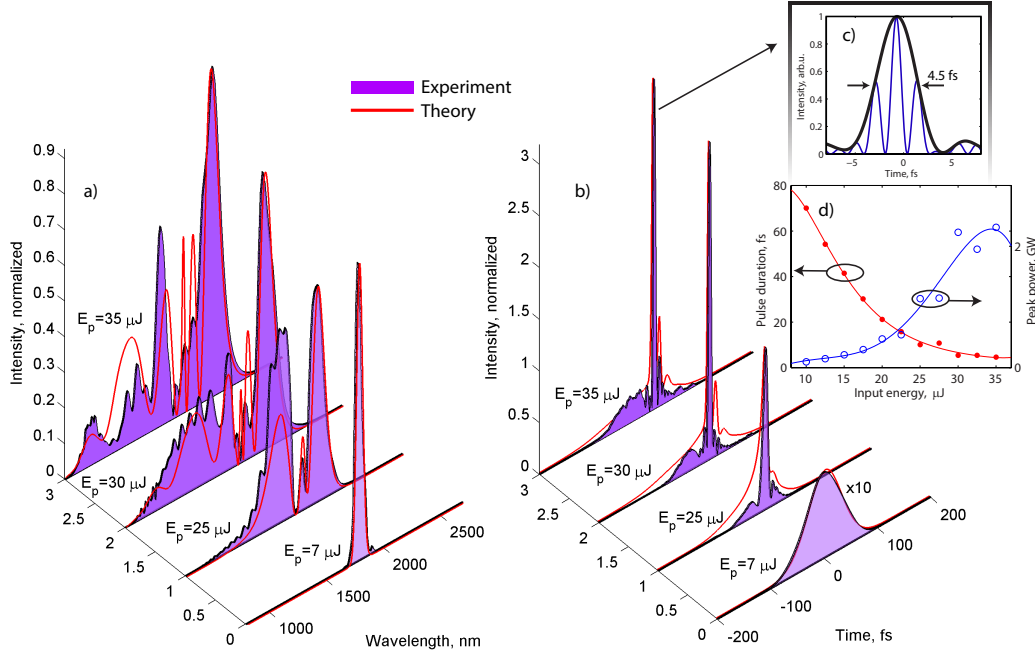


Figure 8.3: Measured pulse self-compression at different energy levels. a) experimentally measured spectra after the waveguide. b) output pulse profiles measured with SEA-SPIDER technique c) Intensity (red) and instantaneous field intensity (blue) profiles of the shortest self-compressed pulse. d) Dependence of the self-compressed pulse duration and peak power on the input pulse energy.

shows that the breakup is constrained due to the higher order nonlinear terms. At $35 \mu\text{J}$ input pulse energy a 4.5 fs pulse is formed. Further increase of the energy does finally break the pulse up. The pedestal of the pulse is intrinsic to the self-compression process. The main pulse contains around 50% of the energy at the shortest 4.5 fs pulse case. At the expense of slightly sacrificing the pulse compression ratio, the pulse fidelity can be substantially improved such that around 60-70% of the energy is gathered in the main pulse. The fibre length of 0.2 m was chosen to achieve the required nonlinear length at a safe operational gas pressure in the fibre cell (section 8.5 describes optimization of experimental parameters). Higher soliton numbers enable compression to shorter pulse widths within shorter stretches of fiber. On the other hand the input pulse energy and peak intensity is limited by the ionization of the noble gas. As expected, Xenon provided the highest self-compression degree because of the highest nonlinearity versus ionization rate ratio and - as a consequence of being an atomic gas - absence of a de-

layered Raman response. The intensity in the fibre is already in the strong-field regime, i.e. the self-compressing pulse begins to ionize the gas. Consequently, the use of a gas (Xe) with a low-ionization potential limited the maximum usable energy of the self-compressed pulse in this waveguide to $\approx 40 \mu\text{J}$. At higher energies, plasma dispersion effects ruin the self-compression mechanism. Despite the low energy, the pulses compress to a single cycle and at a GW peak power level. For the cosine electric field pulse where the peak of the envelope coincides with the peak of the electric field, the instantaneous intensity of the adjacent electric field peaks is 50% less than the main peak. For the extreme nonlinear processes like strong field ionization or high order harmonic generation this confines the interaction to the single main peak of 1.4 fs duration.

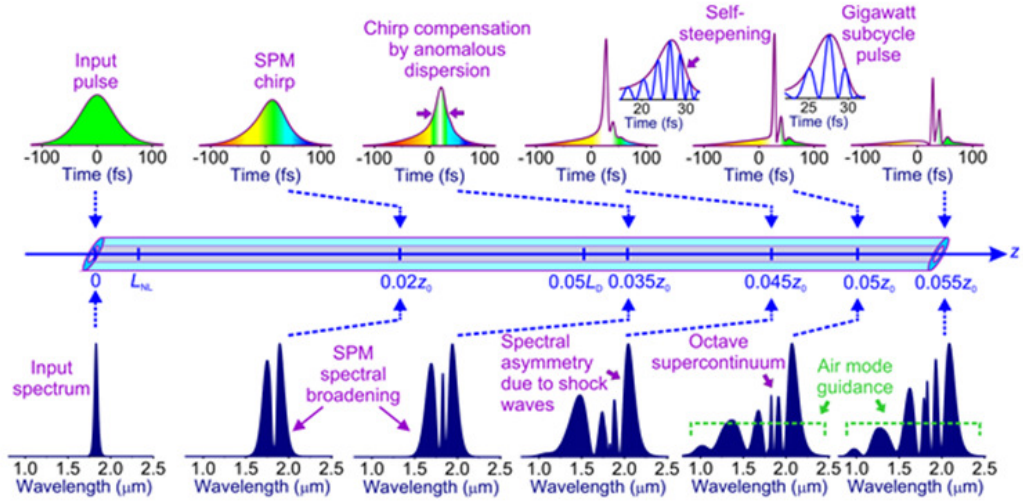


Figure 8.4: Different phases of the pulse self-compression in a waveguide.

The experimental measurement results are in good agreement with theoretical simulations that allow getting more insight into the physics behind the self-compression process. Figure 8.4 outlines the stages of soliton pulse self-compression down to a sub-cycle pulse width. In the case of octave-wide bandwidths, the nonlinear dynamics of the pulse shape deviates substantially from the classical soliton dynamics picture. On the propagation scale of the nonlinear length L_{NL} , self-phase modulation (SPM) induces a chirp and gives rise to noticeable spectral broadening of the laser field. In the regime explored in our work, the dispersion length L_D in this regime is ≈ 290 times larger than the nonlinear length L_{NL} , corresponding to a soliton number $N = \sqrt{L_D/L_{NL}} \approx 17$. With such a mild dispersion, SPM has enough time and space to generate a large nonlinear phase shift and dra-

matically broaden the spectrum before dispersion effects start to play any noticeable role in the solitonic dynamics. At around $z \approx 0.05z_0 \approx 0.08L_D$, (z_0 is the soliton period) dispersion starts to compress the central part of the pulse, where the chirp is almost linear. As the pulse width becomes close to a single field cycle at $z \approx 0.045z_0$, shock-wave effects come into play, blue-shifting the spectra and steepening the trailing edge of the field waveform. Following the point of maximum compression, achieved at $z \approx 0.05z_0$, self-steepening generates an intense blue wing of the spectrum, which eventually falls beyond the zero-group-velocity-dispersion wavelength. Pulse compression in this regime is thus enhanced by self-steepening and is limited by the finite range of air-mode guidance in the gas-filled fibre core. A more in-depth discussion on pulse propagation dynamics and numerical simulations are presented in sections 8.2 and 8.3

8.1 Experimental setup

The experimental setup consists of a femtosecond IR optical parametric amplifier (OPA), Kagome lattice fibre enclosed in a gas cell and an apparatus for spatially encoded spectral phase interferometry for direct electric-field reconstruction (SEA-SPIDER) used for conventional pulse characterization. Figure 8.5 depicts the detailed schematics of the optical arrangement, excluding the ATI spectrometer used in the demonstration of the strong-field capability described in section 8.4. The output of the OPA pumped by a solid-state Yb : CaF₂ chirped pulse laser amplifier running at 2 kHz is tunable in the 1.4 – 1.9 μm range and produces transform limited pulses of 80 fs duration across the tuning range. The dispersion estimation of the fibre show that for gas pressures used in the experiment the waveguide stays in the negative dispersion regime at wavelengths $\lambda > 1.1 \mu\text{m}$. This allows formation of high-order solitons and ultimately leads to the formation of an optical shocks resulting in pulse self-compression at a certain distance. The position where the shortest pulse is formed can be controlled by changing the input pulse energy. More details on the pulse scaling and optimization are given in section 8.5.

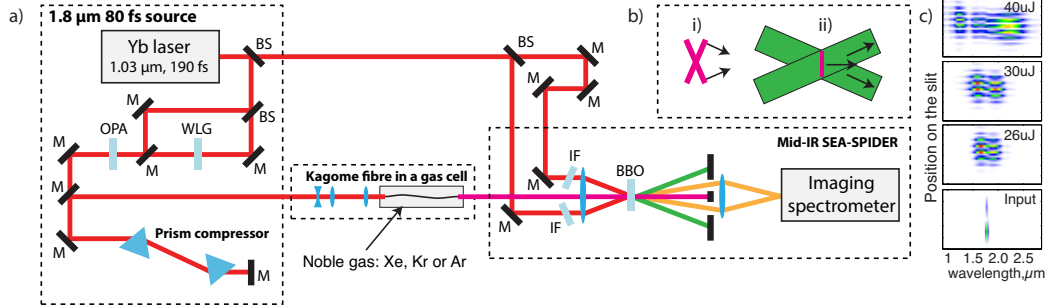


Figure 8.5: a) A general scheme of the experimental setup and the mid-IR SEA-SPIDER pulse characterization apparatus. BS – beam splitter, M – mirror, IF – narrowband interference filter, WLG – white light generation in bulk YAG plate. b) an illustration of geometrical smearing effect in non-collinear SHG FROG measurements: i) two non-collinear beam crossing in the case of SHG FROG and ii) two long-pulse ancilla beams and a short test pulse fully overlap in the case SEA-SPIDER. c) raw SEA-SPIDER traces for several input pulse energies, pulses were self-compressed in 20 cm long fibre filled with 3 bar Xenon.

Pulses from the OPA centered at 1.8 μm wavelength are coupled into the Kagome fibre. The chirp of the input pulses from the OPA is fine-tuned using a prism compressor. The evolution of the pulse temporal profile as a function of input pulse energy was recorded using the SEA-SPIDER technique. The SEA-SPIDER setup was optimized for mid-IR spectral range by using ancillary beams derived directly from the laser pulse at $\lambda_0 = 1.03 \mu\text{m}$. To obtain a frequency shear between the two ancillary beams, they were passed through two independently tuned 3-nm narrowband interference filters. As a result, the wavelength of one ancillary beam is 1025 nm whereas the other ancillary beam is at 1035 nm. The two ancillary beams and the self-compressed test beam are focused using a common spherical mirror onto a BBO crystal, resulting in the generation of two non-collinear sum-frequency beams. The two sum-frequency signals are subsequently spatially filtered and re-imaged on the imaging spectrometer [127]. By processing the measured interference pattern the full temporal profile is reconstructed. The setup was carefully calibrated and cross-checks were applied by simultaneously recording FROG traces so long the bandwidth of frequency-broadened pulses remained within the working bandwidth of the FROG apparatus. The SEA SPIDER and FROG pulse reconstructions under such conditions produced a very nice agreement. Despite the use of a noncollinear beam geometry the SEA-SPIDER technique is free of geometric time smearing. Another factor that makes it a technique of choice for measuring over-an-octave bandwidth

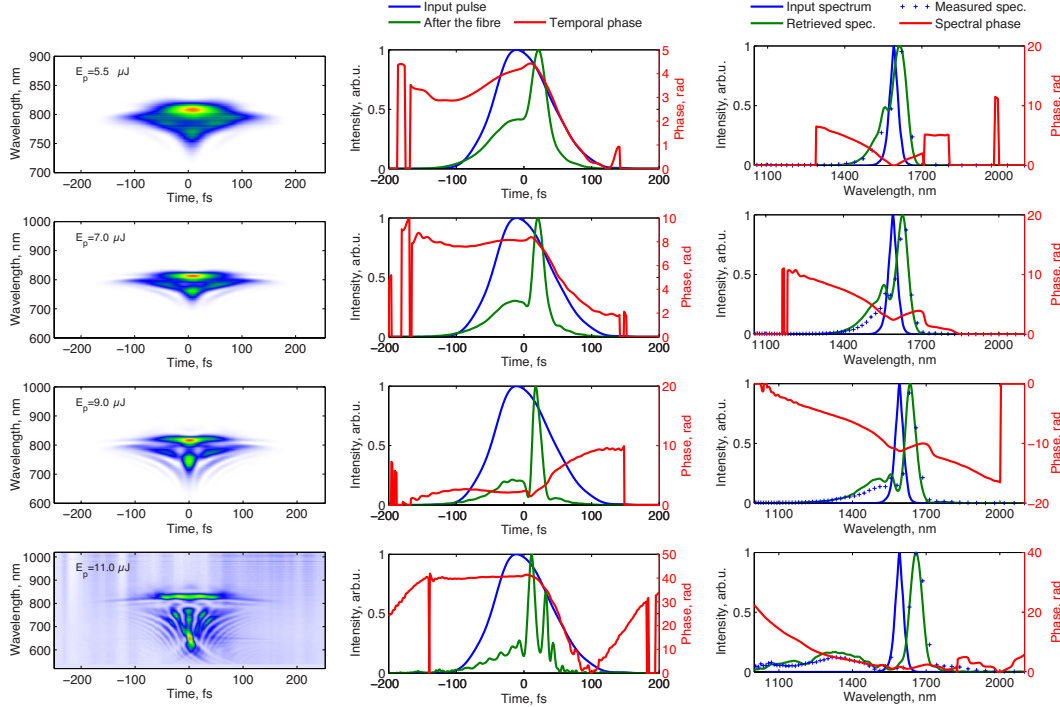


Figure 8.6: SHG FROG traces, reconstructed temporal profiles and spectra of the self-compressed pulses for several input pulse energies. Input pulse parameters: $\lambda_0 = 1.6 \mu\text{m}$, 75 cm long fibre filled with 3 bar Krypton.

pulses with potentially a sub-cycle duration is the lack of bandwidth limitation to within a single octave. The sum-frequency signals are generated from the interaction with narrowband ancillary beams, whereby the entire test pulse volume, despite the noncollinear arrangement, is fully overlapped with the ancillary beams that carry long narrowband pulses and are of a relatively large diameter. The two sum-frequency beams are then filtered using simply a spatial filter and re-imaged on the imaging spectrometer. The full temporal profile of the self-compressed pulse is reconstructed by processing the measured interference pattern of the two ancillary beams on the imaging spectrometer slit.

The SEA-SPIDER technique allows reconstruction of the temporal pulse profile across one transversal spatial coordinate. These measurements, in combination with the direct beam profile measurement using a pyroelectric camera confirm that the pulse self-compresses uniformly across the beam.

As a crosscheck of the SPIDER measurements, we characterized the dynamics of the pulse profile evolution using SHG FROG technique. The results are summarized in the Fig. 8.6. Although the experimental conditions are

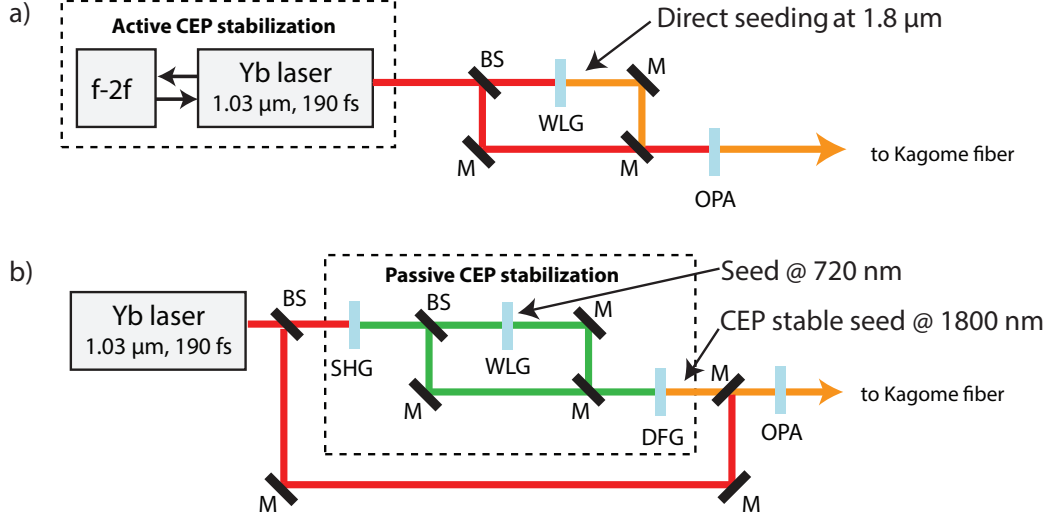


Figure 8.7: CEP stabilization schemes of the input OPA source via a) active stabilization of CPA laser, b) passive stabilization via DFG.

slightly different, these measurements confirm that the pulse uniformly self-compresses at this high peak power regime forming a short pulse with most of the energy concentrated in it. The experimental parameters were not optimized, namely the input pulses were centred at $1.6 \mu\text{m}$, there was some uncompensated chirp of the OPA source, which resulted pulses with stronger pedestal. The limitation of FROG technique is that the bandwidth is limited to below one octave. In other words, for the over-an-octave bandwidth, the second harmonic of the long wavelength wing overlaps with the short wavelength spectral wing of the fundamental pulse. In the non-collinear geometry pulse duration is inevitably overestimated due to geometrical smearing effect. Despite these limitations, pulses as short as 8 fs were measured using SHG FROG technique independently of SEA-SPIDER measurement.

The CEP of the input source was locked and controlled using active CEP stabilization loop of the Yb pump laser as shown in Figure 8.7 a). The OPA is seeded via supercontinuum generated in a bulk YAG plate which inherits the CE phase of the driving laser pulse [128]. The oscillator and CPA of the driving laser is stabilized using two feedback loops, the fast loop based on heterodyne phase detection stabilizes the oscillator and the second loop based on spectral phase detection stabilizes the slower phase drifts in the amplifier. The stabilization of the driving laser system is described in details in chapter 4.1. However, since OPA is used for frequency conversion anyway, it is possible to simplify the setup greatly by implementing passive CEP stabilization in the OPA [65, 76, 10] as shown in Figure 8.7 b). The passive CEP lock is

achieved by generating seed at 1800 nm via difference frequency generation between the short wavelength side of the supercontinuum spectrum and the frequency doubled pump pulse [129].

Figure 8.8 shows characterization data of the OPA source that was used for the experiments. The pulses from the OPA are nearly transform limited and do not require any sophisticated dispersion management apparatus typically attributed to OPCPA schemes [130]. The central wavelength can be tuned within the range of 1.4-1.8 μm . The spot of the beam has a rather good quality with symmetric Gaussian profile. The temporal profile, however, has some residual chirp. The chirp, in principle, can be compensated using ≈ 30 mm glass block, however, the third order phases add up. For the best compression a pulse shaper (i.e. DAZZLER) can be used.

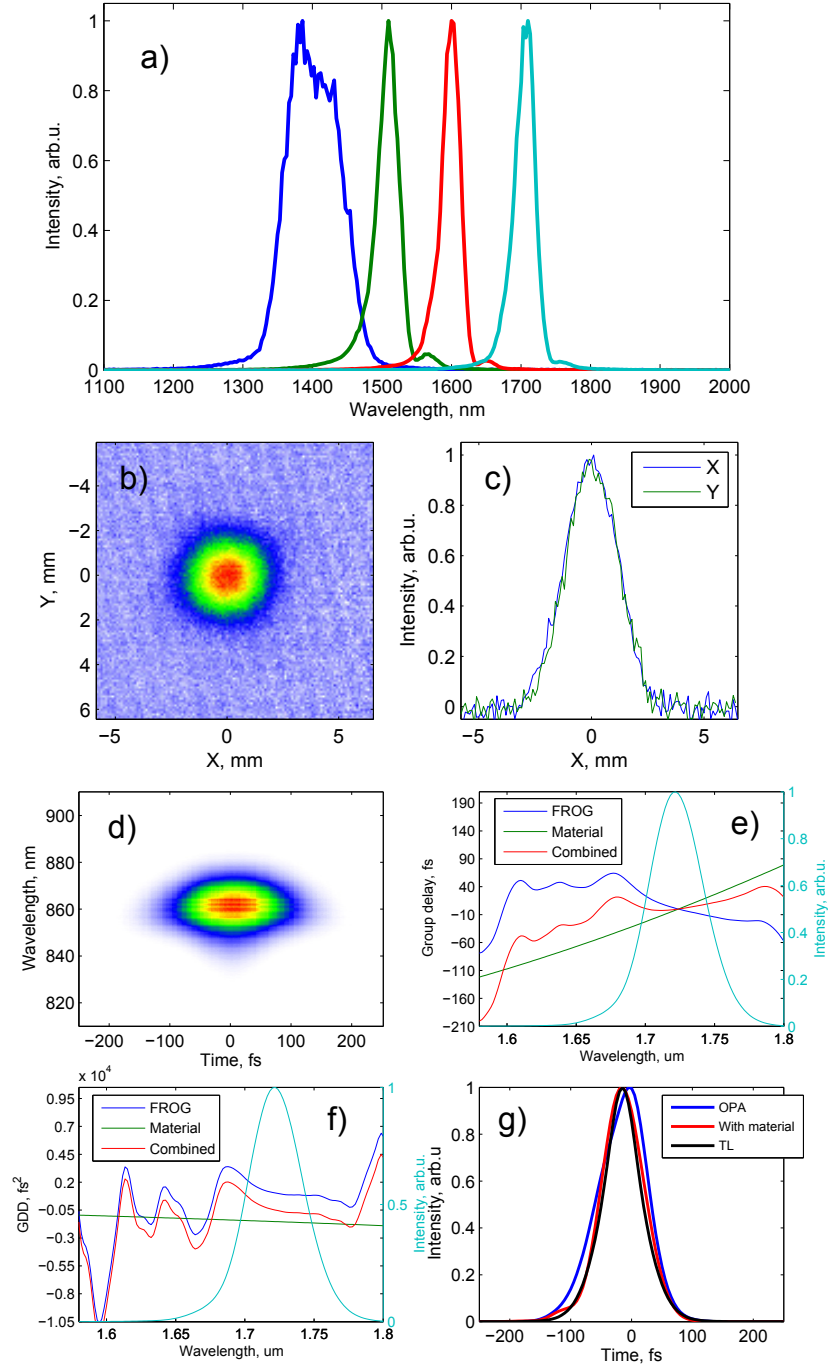


Figure 8.8: Characterization of the OPA used for the Kagome experiments. a) spectra at different central wavelengths, b) and c) beam profile and the lineouts. Panels d)-g) shows the temporal characterization of the input pulse and the calculation of the pulse compression using 30 mm thick fused silica glass block. d) measured FROG trace, e) reconstructed group delay of the spectral components of the input pulse the fiber, f) group delay dispersion, g) temporal profiles of the input pulse, calculated compression using a 30 mm glass block and the transform limited pulse shape.

8.2 Pulse propagation dynamics

The envelope evolution upon nonlinear pulse propagation in the waveguide is a highly complex process involving an interplay between the nonlinear phase shift due to intensity-dependent refractive index and dispersion of the waveguide and the filling gas. Note that unlike in the case of femtosecond pulse filamentation [131], the dynamics is mainly confined to one dimension in space because of a true waveguide geometry and the complicated spatial-temporal coupling effects can be neglected under the conditions used in this experiment. This not only results in a spatially uniform pulse at the output of the fibre, but also greatly simplifies the analysis of the nonlinear dynamics and yields a better understanding of the physics behind the self-compression process. Moreover, the use of noble gas as a nonlinear medium that has no vibrational or rotational Raman activities provides a nearly perfect instantaneous nonlinearity that works favorably for the formation of optical shock waves. In the case of non-linear propagation in the self-compression regime, the short pulse is obtained at a specific distance in the fibre for a given conditions. However, the fibre length cannot be varied in the experiment. The easily variable parameter is the pulse energy which also determines the position at which the short pulse is formed. Figure 8.9 shows the measured pulse spectrum and temporal profile dependence on the input energy. Generally, the higher is the input pulse energy, the broader is the spectrum and the shorter is the pulse at the output of the fibre. The dynamics can be roughly divided into three phases. In the first phase, the pulse continuously shortens with increasing input pulse energy as indicated in the graph Fig. 8.3d. This regime can be considered as a classical high order soliton evolving towards short peak formation. The spectrum broadens nearly symmetrically, the positive chirp due to self phase modulation is balanced with the phase shift induced by the anomalous dispersion of the fibre (see Figure 8.1c). However, when the pulse gets shorter, the peak of the pulse is slowed down relative to the rest of pulse temporal components due to the dependence of the group velocity on the intensity and an optical shock wave formation sets in enhancing the pulse shortening [126]. Finally in the last stage marked (iii) in Figure 8.9 a very short light transient is formed right at the exit of the fibre with the envelope duration shorter than the field cycle with most of the input pulse energy concentrated in it. At this point the peak intensity reaches the level where ionization becomes significant and eventually limits the further increase of peak power.

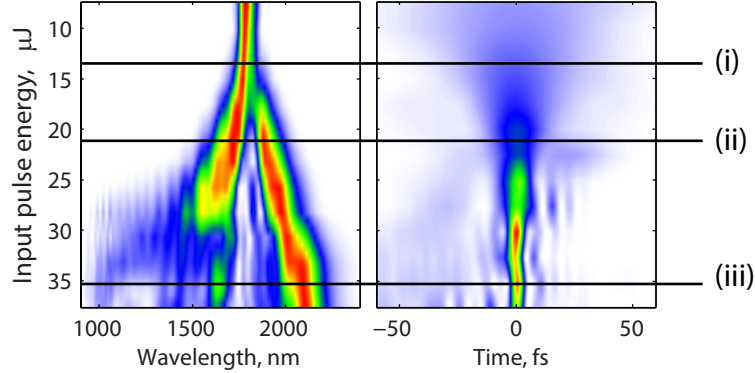


Figure 8.9: Dependence of the self-compressed pulse spectrum (left panel) and temporal profile (right panel). The dynamics can be divided into three phases: (i) classical high order soliton formation, where the SPM-induced nonlinear phase is balanced by the phase acquired due to the negative dispersion of the fibre and the input pulse power is several times the power of the fundamental soliton. (ii) the spectrum of the self-compressed pulse increases enough so that the group velocity dependence on intensity steepens the trailing edge of the pulse and an optical shock wave starts to be formed. (iii) an intense sub-cycle duration light transient is formed as a result of shock-wave-enhanced soliton self-compression.

8.3 Numerical simulation of nonlinear pulse propagation

In the case of solitonic self-compression, the short pulse is obtained at a specific distance in the fibre for a given conditions. However, the fiber length cannot be varied in the experiment. The easily variable parameter is pulse energy which also changes the position where the short pulse is formed. The simulations show that varying the pulse energy is somewhat similar to the varying the distance except that soliton order is also changing. The simulation of $\tau_{fwhm} = 80$ fs pulse centered at $\lambda_0 = 1.7 \mu\text{m}$ propagation through a fiber with second $\beta_2 = -442 \text{ fs}^2$ and third $\beta_3 = 1380 \text{ fs}^3$ order dispersion medium (shown in Figure 8.1 (c)) for various input energies is shown in Figure 8.10. The simulation was done for Krypton ($n_2 = 2.6 \times 10^{-23} \text{ m}^2\text{W}^{-1}\text{bar}^{-1}$) at 6 bar pressure and $d = 82 \mu\text{m}$ fiber core diameter. Sidebands in the spectrum moving towards long wavelength side with increasing energy can be identified in measured and simulated spectra. The corresponding soliton order at the first compression cycle is approximately $N \approx 4$. The second and third order dispersion values were approximated using a polynomial fitted to capillary

dispersion profile calculated using finite element analysis.

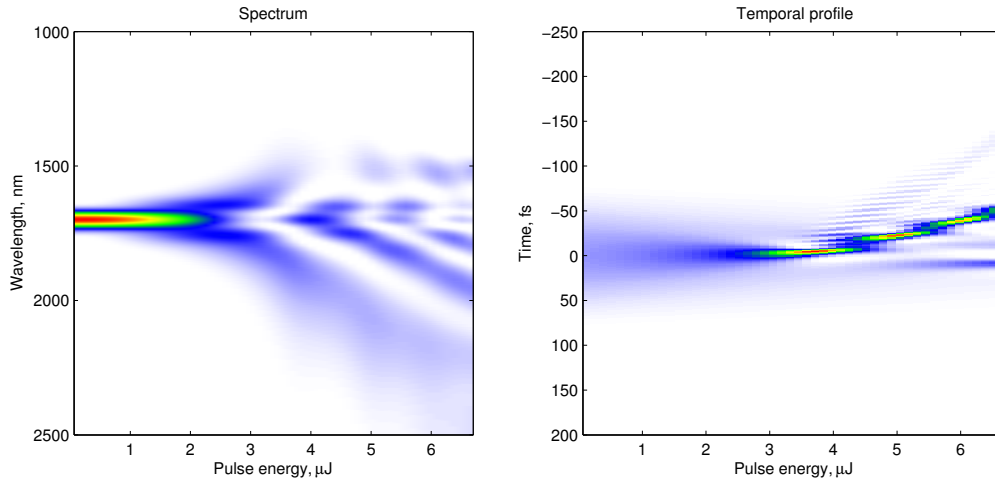


Figure 8.10: Simulation of solitonic self-compression: temporal profile and spectrum dependence on the input pulse energy for a fixed 1 m fiber length. Gas pressure: 6 bar of Krypton.

The spectrum and temporal profile corresponding to the first compression cycle at pulse energy $E_p = 3.5 \mu\text{J}$ is shown in Figure 8.11. Due to third order dispersion, the pulse profile is asymmetric with a higher “bump” at the long wavelength side which is consistent with our experimental observations.

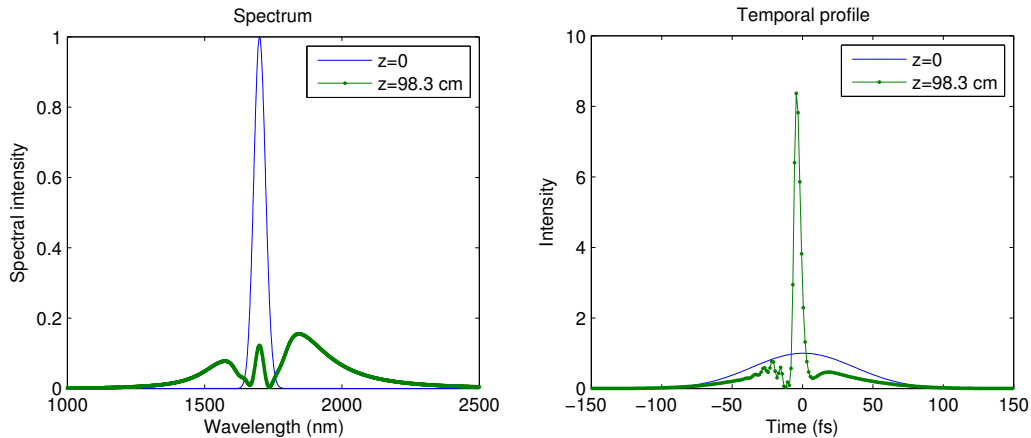


Figure 8.11: Simulated spectrum and temporal profile at $E_p = 3.5 \mu\text{J}$.

A more detailed comparison of the effect of the spectral phase of the input pulse is shown in Figure 8.12. The propagation dynamics and the spectrum

strongly depends on the shape of the input pulse. Positive chirp tends to induce formation of two symmetric “bumps” and splitting of the spectrum. Negative chirp yields first narrowing of the spectrum and then again broadening. More importantly, the third order phase yields asymmetric spectrum and formation of a sharp spike in the spectrum as shown by arrows in panels d) and e). This illustrates the necessity for careful phase control of the input pulses as even a small chirp on the input pulse that does not significantly change pulse duration, has a dramatic effect on the self-compressed pulse shape.

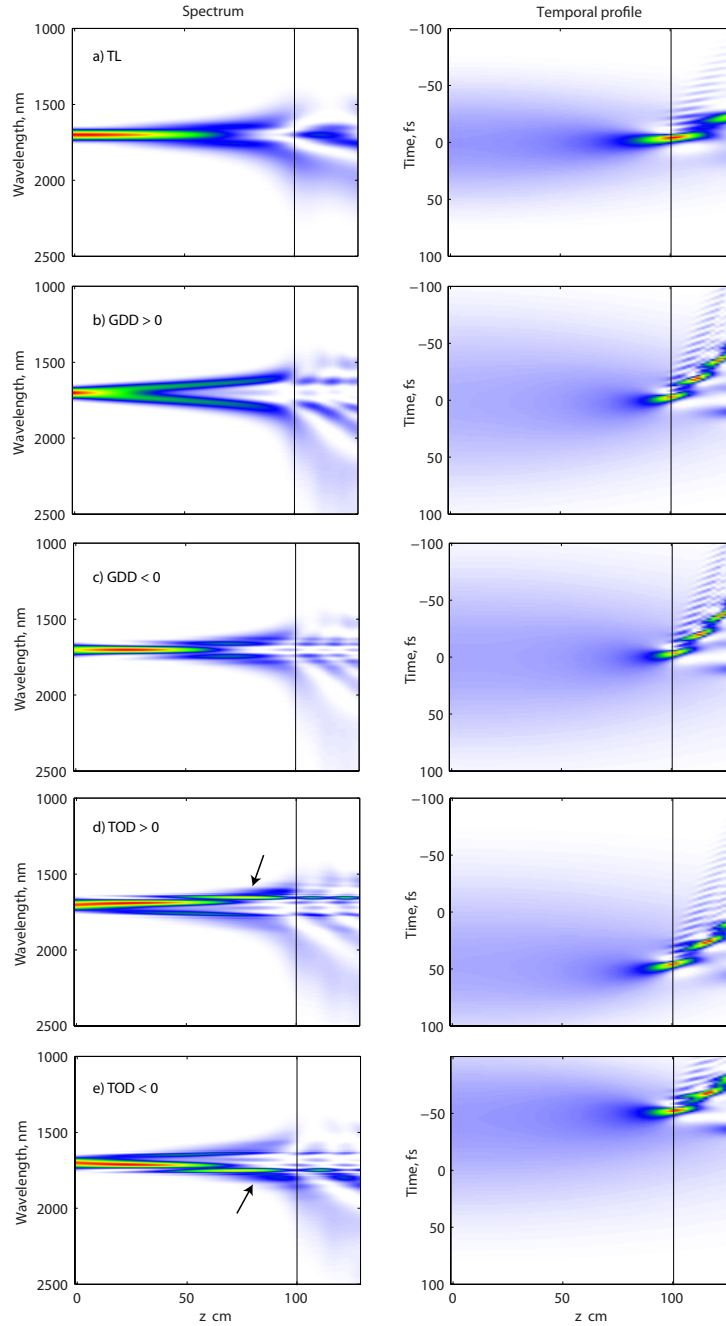


Figure 8.12: Simulation of solitonic self-compression for various input pulse shapes. a) transform limited pulse, b) positively c) and negatively chirped, d) positive and e) negative third order phase. The soliton order was adjusted in each case in order to keep the first compression cycle at a constant distance of $z = 1$ m; The corresponding soliton orders are: a) $N = 4.9$, b) $N = 7.5$, c) $N = 8.2$, d) $N = 7.0$ and e) $N = 7.2$. Input pulse center wavelength $\lambda_0 = 1.7 \mu\text{m}$. The arrows show the formation of a sharp spike in the spectrum in the presence of the third order phase.

8.4 Characterization of the self-compressed pulses with stereo-ATI electron spectrometry

Here self-compressed pulse characterization using stereo Above Threshold Ionization (stereo-ATI) electron spectrometry is described. These experiments also serve as an example of the application of these self-compressed pulses for strong field experiments. Using stereo ATI spectrometer that consists of two time-of-flight (TOF) electron spectrometers in two directions we measure the photoelectron spectrum of the ionized noble gas atoms (Xe) for different carrier envelope phase (CEP) values. The calculated instantaneous intensity (field squared) of the shortest self-compressed pulse and the ionization rate of xenon as shown in Figure 8.13. By focusing that into 60 μm spot, the peak intensity $6 \times 10^{13} \text{ W/cm}^2$ is reached. Due to highly non-linear nature of the ionization, only one half-cycle yields significant ionization rate, leads to a cleaning effect of the wings.

The CEP dependent ATI spectrum measurement is a tool that provides direct information on the number of cycles in the ultrashort pulse [132]. For a cosine pulse ($\varphi_{cep} = \pi/2$), there is only one strong half-cycle that generate electrons that are drifting only in one direction. The other half-cycles have much lower instantaneous intensity and produce much lower electron yield. Moreover, in the energy resolved photoelectron spectrum one can directly measure the cut-off which is proportional to the instantaneous intensity $U_p \propto I_{inst} \times \lambda^2$. By measuring the ratio of the cut-offs in the left and right directions U_p^{left}/U_p^{right} , one can directly measure the ratio of the instantaneous intensity of the adjacent half-cycles. For a sub-cycle pulse the intensity of the adjacent half-cycle be $<50\%$. The shortest pulse generation and the strong-field ATI spectrometry experimental conditions were slightly different, for the ATI experiment the fibre length was optimized for high energy therefore the pulses are slightly longer, producing pulses with the adjacent half-cycle peak intensity ratio of around 60% as shown in the measured electron spectrum in Figure 8.13.

One challenge of the nonlinear pulse self-compression is that the pulse intensity in the last stage of the compression, just before the fibre exit, is at its highest. The high intensity compatible with the level needed for strong-field experiments can be achieved by filling the fibre with high ionization potential (I_p) noble gas and tightly refocusing the self-compressed beam on target. In the experimental scheme shown in Figure 8.13 a), we filled the fibre with Neon gas and the lower I_p Xenon gas was used in the ATI spectrometer. The beam was refocused with demagnification factor $f_1/f_2 = 2$ thus further increasing the intensity in the interaction region. This allowed nearly fully

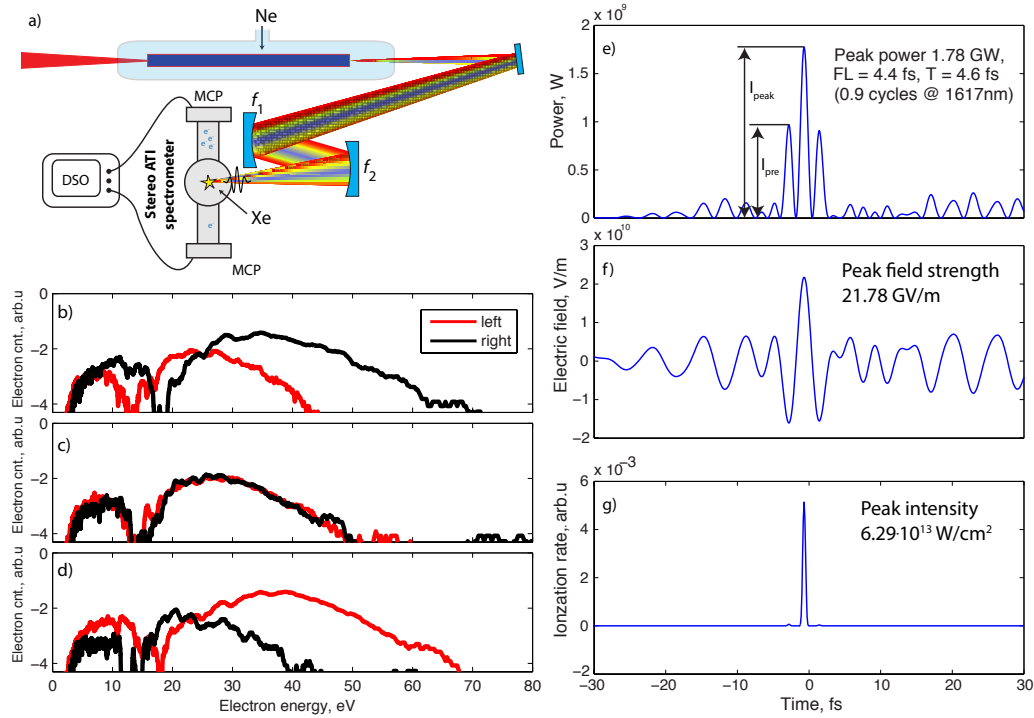


Figure 8.13: An illustration of application of the self-compressed pulses for strong field physics experiments. a) experimental scheme for the use of self-compressed single-cycle pulses for ATI electron spectrometry. DSO – digital sampling oscilloscope. Spherical mirror focal lengths f_1 and f_2 were chosen in order to increase the intensity in the ATI spectrometer. Panels b) and d) show the large asymmetry of the electron spectrum in the two directions for different CEP, indicative of $+\cos$ and $-\cos$ electric fields, whereas panel c) shows the symmetric case, indicative of a \sin electric field. Panel e) shows the instantaneous intensity and the intensity ratio of the two adjacent half-cycles I_{pre}/I_{peak} and f) electric field of the shortest self-compressed pulse. Panel g) show the corresponding calculated ionization rate in Xe assuming $60 \mu\text{m}$ spot size.

ionizing the target gas while completely avoiding detrimental effects due to ionization in the fibre.

8.5 Optimization of self-compression and energy scalability

The fibre length, gas type and pressure were optimized to ensure the shortest pulse generation. The duration of the self-compressed pulse can be decreased by increasing the corresponding soliton number which translates into shortening the fibre length. Higher soliton numbers help to achieve shorter pulse widths within a shorter stretch of fibre and make the pulse less sensitive to the nonuniformities of the transmission of the fibre as the dynamics is confined to a shorter length. However, the reduction of the nonlinear phase shift due to shortening of the fibre has to be compensated by increasing the nonlinearity of the medium. The gas type is chosen according to the nonlinearity and pressure limitations of the experimental setup. Different inert gases (Xe, Kr, Ar, Ne, He) have different ionization potentials I_p . The higher the I_p , the higher the intensity can be achieved before detrimental ionization effects sets in, the more energy can be coupled into the fibre. However, the nonlinearity of the gas also decreases strongly with increasing I_p . For the experiment, the Xe gas was chosen which has the highest nonlinearity. Another optimization parameter is the gas pressure in the cell – the nonlinearity Δn grows linearly with the pressure. This means that for example, that by increasing the pressure twice, almost the same dynamics can be achieved at just half of the intensity. The ionization probability is a highly nonlinear function of intensity. However, in the experiment in order to out-couple the pulse with minimal distortion a very thin window has to be used which limits the pressure that can be used in the gas cell. In the experiment Xe at 4 bar was used. The maximum pressure that we achieved with 150 μm thick window is 10 bar.

The maximum transmittable pulse energy depends on a number of experimental parameters, such as coupling efficiency, nonlinearity of the filling gas, pulse duration, etc. Although we did not do a systematic damage threshold measurements, we did observe damage of the fibre at around 150 μJ of the input pulse energy. However, recently mJ level pulse transmission through a very similar fibre structure was demonstrated [133]. Furthermore, our system provides a lot of freedom in scaling both in terms of pulse energy and spectral properties. These control parameters of our system are the following: a) the fibre transmission and dispersion can be tailored by simply changing

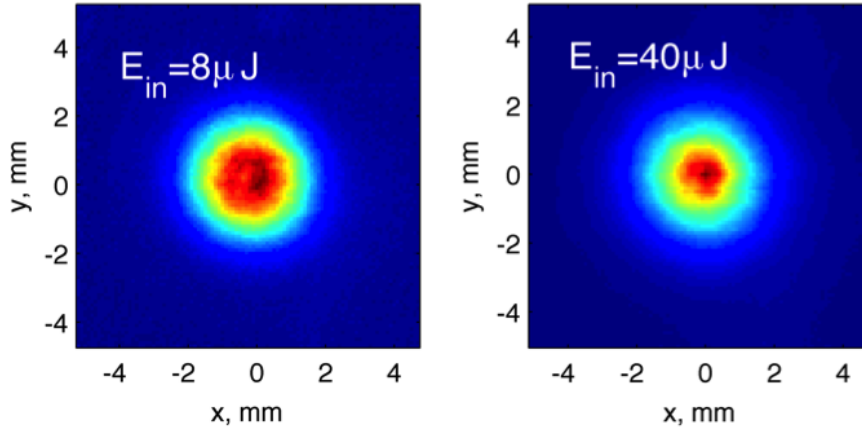


Figure 8.14: Comparison of the beam profile at the output of the fibre for different input pulse energies.

the cladding silica web thickness. With this, one can tune the dispersion regime and zero-GVD wavelength; b) the fibre dispersion is so low that introducing a gas provides a further dispersion control. c) energy scaling and photo-ionization handling could be done by simply introducing a higher I_p gas such as helium, and/or operating at low pressure. This could be done without compromising the nonlinear spectral broadening by adjusting the fibre length and its effective area.

Another limitation is the spatial self-focusing inside the fibre due to Kerr lens which limits the maximum peak power. The critical power scales with wavelength as $P_{crit} \propto \lambda^2$, therefore the infrared spectral range around $1.8 \mu\text{m}$ we use in our experiments acts favorably and allows achieving higher peak power of the final self-compressed pulse. The experimental parameters were optimized in order to achieve the shortest pulse duration keeping the peak power below the self-focusing threshold. The changes of the beam profile at the output of the fibre at low and high input energy are minor in our experiments, as shown in Fig. 8.14.

We experimentally show the possibility to upscale the energy of the self-compressed pulse by choosing the type of gas and simultaneously adjusting the gas pressure and the fibre length. The pulse compression in the Kagome fibre can be optimized for various regimes and the extremely short pulse duration comes at the expense of reduced fidelity of the pulse. The shortest duration of the self-compressed pulse measuring 4.5 fs FWHM (Figure 8.3) was obtained in a 20-cm long piece of fibre filled with Xe ($I_p = 12.13 \text{ eV}$) at the pressure of 4 bar and the corresponding input pulse energy was $35 \mu\text{J}$. The highest output energy of $75 \mu\text{J}$ of the self-compressed pulse in our experi-

ments was obtained in a 45-cm-long piece of fibre filled with Ar ($I_p = 15.8$ eV) at the pressure ≈ 1 bar. These results demonstrate great flexibility of the nonlinear pulse compression scheme whereby the substitution of the gas ionization potential and dispersion can be efficiently compensated by controlling the gas pressure and the fibre length. Nevertheless, there is a noticeable impact on the fidelity of the self-compressed pulse as the shortest duration obtained at the highest energy in the case of Ar measures 6 fs FWHM. The ability to reach an efficient self-compression regime over a wide parameter space including the pulse energy, wavelength and the Kagome waveguide geometry proves the overall robustness of the method and its adaptability to application-dictated target parameters.

In order to illustrate the effect of the dispersion of transmission optical elements on the pulse profile of these short self-compressed pulses and emphasize the importance of optimizing the optical setup for minimal dispersion, calculation shown in Figure 8.15 shows the distortion of the 3 mm thick fused silica window on an ultra-short 8-fs pulse.

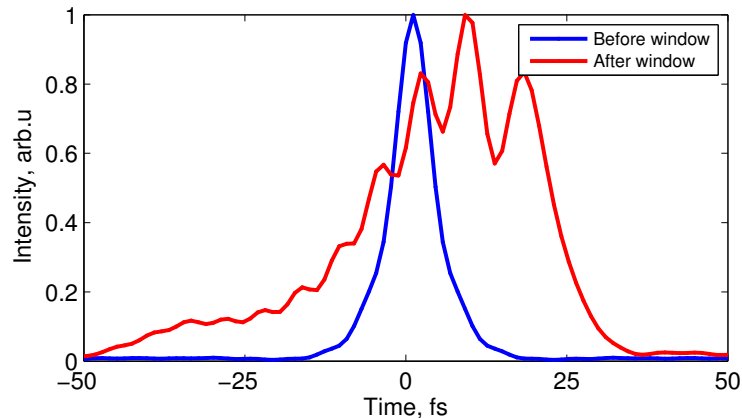


Figure 8.15: Calculation of the effect of a 3 mm thick window dispersion on the self-compressed 8-fs pulse.

8.6 Configurations of the strong-field source

The self-compression scheme in Kagome fiber described here is compatible with several geometries used in generic strong-field experiments. Specifically, one challenge is the delivery of the self-compressed pulse onto the target and the ability of the nonlinear self-compression scheme to compensate extra dispersion between the fiber exit and the target to which the pulse has to be delivered at the highest possible level of compression. Here, we assume

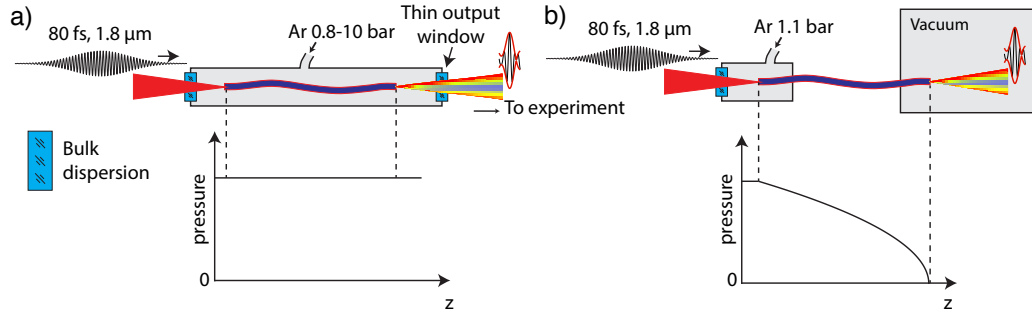


Figure 8.16: Schemes of pulse delivery to an application and corresponding pressure profiles along Kagome fibre in case of a) fibre mounted in a static gas cell and b) a pressure gradient case when the output of the fibre is mounted directly in a vacuum chamber.

that a dispersion-less focusing is employed by use of a concave mirror and distinguish two generic geometries suitable for a strong-field experiment, as summarized in Fig. 8.16. The first relevant geometry, shown in Fig. 8.16a, is based on a Kagome waveguide in a cell with a static gas pressure. At the minimum, this includes an inevitable extra dispersion of the out-coupling window. In some schemes, on top of that one might be also required to compensate additional dispersion contributions arising from propagation through air and an in-coupling window. The second scheme, shown in Fig. 8.16b, assumes fiber termination directly into a vacuum target chamber. The main conceptual difference between the two schemes is that the one with vacuum termination avoids extra bulk dispersion and supplies a longitudinal pressure gradient.

The case of extra bulk dispersion (Fig. 8.16a) is frequently encountered in gas-based self-compression schemes [134, 135] and can be turned into an advantage because the intensity of the divergent beam in the exit window is low and it can be treated as a linear bulk compressor. The bulk dispersion of the window in the case of the IR wavelength is anomalous, i.e. of the same sign as the gas-filled waveguide dispersion. Because of that, one can terminate the process of nonlinear self-compression at a safe peak power level and then additionally post-compress the pulse with bulk dispersion to reach a higher peak power level while avoiding additional nonlinear interaction. In section 8.5 it is explained how the interplay of the intensity, gas nonlinearity, gas pressure and the waveguide length can be used to optimize the compression level and the peak power. In a practical experiment, in which the gas type and the fiber length are fixed, we carefully tune the gas pressure and attenuate the input pulse energy to achieve the desired balance

between the pulse energy and pulse fidelity and duration. In the context of the experiments with Xe and Kr filling gases presented in the main article text, we point out that the presence of small extra bulk dispersion allows us to increase the pulse energy on target compared to the case when the highest peak power would be reached inside the fiber, entailing ionization loss and associated pulse distortions. We conservatively estimate that the use of a 150 μm thin output window helps us win additional 10-15% of the usable pulse energy and an even larger fraction of the achievable peak power (cf. section 8.2) compared to the case when the self-compressed pulse exits the waveguide without a small amount of pre-chirp compensated by the window. The case of vacuum termination (Fig. 8.16b) closely resembles the pressure-gradient technique used in the hollow waveguide chirping technique for high-energy pulses [136]. The main advantage of this scheme is that the energy transmission can be significantly boosted in comparison with the static pressure case because the gas density is progressively reduced with the growth of the peak power, helping to hold off ionization losses. Whereas the experiments presented in the paper were performed using the fiber in a static gas cell, we have also investigated the suitability of the scheme in the geometry shown in Fig. 8.16b. Figure 8.19 compares the evolution of the pulse spectrum as a function of input energy in both geometries for a $L=45$ cm piece of Kagome filled with a static pressure of 1.2 bar (Fig. 8.19 a,c) and with evacuation connected to the fiber output Fig. 8.19 b,c).

8.7 Fibre properties

Transmission curve of the 3 meter long fibre is shown in Figure 8.17. The transmission signal was normalised to the supercontinuum light source. The spectrum exhibits a very low loss for the wavelengths longer than 1 μm . This corresponds to the fundamental band of the inhibited coupling guiding fibre [122] and extends above 2.4 μm ; which is the long-wavelength detection limit of the used spectrum analyser.

The dispersion of the waveguide was modelled using finite element analysis and commercially available software package. The modelled structure was extracted from scanning electron micrograph (SEM) of the fibre. The detailed of mode solving can found in the supplementary materials of Ref. [122]. The group velocity dispersion in the spectral range relevant to this experiment is shown in Figure 8.1 c). The polynomial fitting function (8.7) and its coefficients that describe the dispersion are listed below:

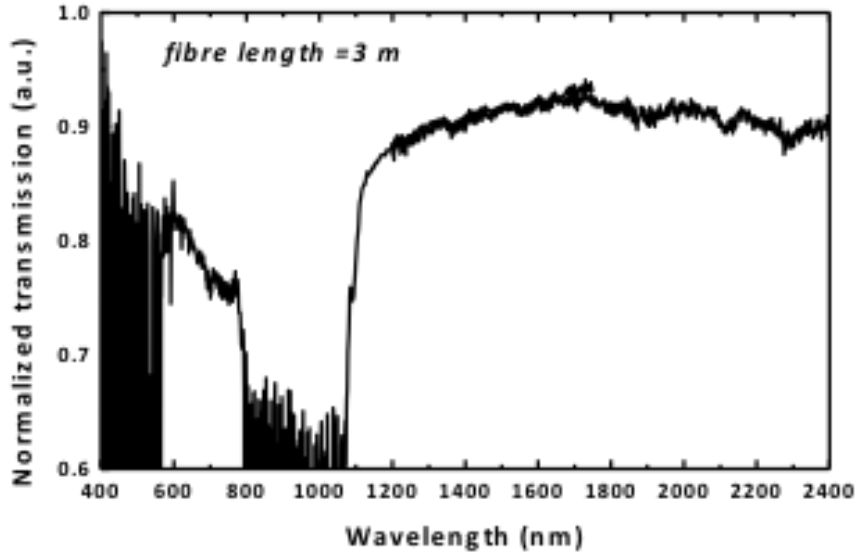


Figure 8.17: Measured transmission spectrum through 3 m long fibre. The transmission signal is normalised to the whit light source. The graph was kindly provided by F. Gérôme and F. Benabid.

$$\begin{aligned}
 GDD \left[\frac{ps}{nm \times km} \right] = & -3335.64 \times \Lambda \times \\
 & \times (0.00931144 - 0.0181275 \times \Lambda + 0.00986497 \times \Lambda^2 - 0.000860359 \times \Lambda^4),
 \end{aligned} \tag{8.1}$$

here wavelength Λ is expressed in units of μm .

8.8 An integrated self-compression and XUV-generation scheme

Coherent soft XUV sources based on high-order harmonic generation (HHG) are required for applications in non-invasive materials imaging and control and are of great importance in time-resolved atomic and molecular physics. Recently, the collection of available femtosecond sources for driving HHG grew to include long-wavelength optical parametric amplifiers (OPA) [137] and high-repetition-rate Yb fiber and slab lasers [23], representing the trends for wavelength- and average-power scaling aimed at improving the XUV photon flux. For driver wavelengths in the near- and low mid-IR, the process of

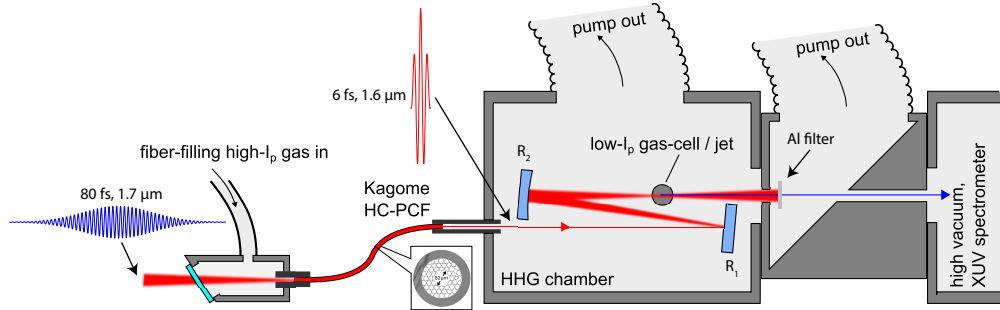


Figure 8.18: Experimental scheme of integrated pulse self-compression based on Kagome HC-PCF and XUV pulse generation via high order harmonic generation. We launch 80-fs pulses with up to $120 \mu\text{J}$ energy into a 45 cm long Kagome HC-PCF with an inner-circle of $82 \mu\text{m}$ (mode-field diameter $\approx 64 \mu\text{m}$). The input pulses were generated in an optical parametric amplifier with $1.7 \mu\text{m}$ signal wavelength. The fiber, whose cross section is shown in the inset, was optimized for this spectral range, exhibiting a very low linear loss of $\approx 70 \text{ dB/km}$ and negative dispersion throughout the spectral range of $1.2\text{--}2.0 \mu\text{m}$. Solitonic self-compression is achieved by filling the fiber with several bars of a noble gas providing optical nonlinearity while remaining in the negative dispersion regime. The output of the Kagome HC-PCF is refocused onto a gas cell where HHG is generated and a $0.2 \mu\text{m}$ Aluminum filter separates the XUV radiation.

HHG is accomplished within a single optical cycle, leading to essentially an isolated attosecond XUV burst. Consequently, a massive development effort has been invested over the past decade into the generation and application of quasi-single-cycle driver pulses for HHG. A typical scheme includes an external pulse compression stage—an SPM-based spectral broadening [26] with a subsequent dispersion compensation—wedged between the laser source and the HHG setup and severely compromising the robustness of the chain in the whole range of aspects: pointing instabilities, intensity and phase fluctuations, thermal drift, etc. The quest to eliminate the problems associated with a separate setup for external pulse compression has led to the emergence of hybrid methods in which the shortening of the driver pulse and the high-order harmonic emission are combined in the same target medium. Recently, for the mJ energy range, pulse self-compression and HHG, both taking place in a single filament in the target gas, were reported [138, 25]. In the sub-mJ pulse energy range, however, such a fortunate combination is not feasible because it is not possible to supply the correct dispersion profile in a high-pressure gas target.

In this section a very robust scheme is presented allowing to combine a waveguide-based self-compression of IR pulses with energies up to $100 \mu\text{J}$ with HHG in an integrated scheme depicted in Fig. 8.18. The nonlinear pulse shortening down to a single cycle duration [116] takes place in a Kagome-lattice microstructure fiber filled with a noble gas [112, 115, 122, 123, 124]. The pulse characterization measurements described in the previous sections of this chapter confirm that the self-compressed output can ensure, with moderate focusing, peak intensities sufficient for driving high-field phenomena such as above threshold ionization [116]. Here we demonstrate that such pulses are also capable of a far more challenging driving of a bright HHG source. Prior to integrating the Kagome self-compression stage into the HHG setup, we have verified that it was possible to perform XUV generation also in a stand-alone version, i.e. when the Kagome setup was completely isolated from the vacuum HHG setup and the extra dispersion—contributed by the exit window of the Kagome gas cell, passage in air, and the entrance window of the HHG chamber—has noticeably negatively pre-chirped the pulse. The integrated setup depicted in Fig. 8.18 solves the issue of a mechanically robust, dispersion-free coupling of the self-compressed pulses into the HHG target. In addition, the termination of the exit facet of the Kagome fiber into vacuum, rather than into a static pressure as in a cell, supplies a useful pressure gradient. The latter ensures that the gas density is progressively lowered as the peak power of the pulse undergoing self-compression during its propagation down the fiber core progressively grows. As a result, it is possible to bypass the limit imposed on the energy of the self-compressed pulse by ionization of the gas in the vicinity of the output facet of the fiber and, consequently, to increase the energy available for HHG driving. The presented combination of a nonlinear compression technique coupled to an HHG target provides very well controllable adjustment parameters and enables the use of different gases in the Kagome fiber and the HHG target. The gases are chosen to deliberately prevent ionization inside the Kagome fiber (requiring a higher ionization potential, I_p , gas) and enable it in the HHG target (filled with a lower I_p gas). The optimum pulse compression is achieved by balancing the backing gas pressure connected to the inlet at the entrance of the Kagome fiber and the injected pulse energy.

The input end of the fiber is connected to a miniature gas cell filled with Krypton (the high- I_p gas) at around ≈ 1.3 bar absolute pressure. The output end of the fiber is introduced into the vacuum system of the HHG beam-line. This creates an approximately linear gradient of the gas pressure in the fiber. Due to small core and long length of the fiber, the gas flow rate through the fiber is negligible compared to the gas load of the HHG gas target. The input pulse energy and the gas pressure in the fiber is adjusted in order to

get the shortest pulse at the output of the fiber. In the XUV generation vacuum chamber the output beam from the fiber is refocused into a 0.7 mm long Xe gas target using two spherical mirrors (radiuses of curvature $R_1 = -400$ mm and $R_2 = -200$ mm respectively). The demagnification factor of two as well as the lower I_p of the Xenon gas used in the target for the HHG allows achieving high degree of ionization level required for the XUV generation while simultaneously avoiding detrimental effects of plasma on the pulse self-compression. Input 80-fs pulses centred at $1.7 \mu\text{m}$ are launched into Krypton-filled Kagome HC-PCF where they undergo self-compression due to combined effects of the self-phase modulation, negative dispersion and shock-wave generation and yield an impressive 20-fold pulse shortening.

The spectrum measurements of the self-compressed pulses are shown in Fig. 8.20. The intensity of the self-compressing pulse towards the end of the fiber increases and reaches values that lead to low but significant strong-field ionization of the fiber-filling gas at the maximum input energies. This is an undesired effect and the pressure gradient allows reducing its effects as the pressure towards the end of the fiber decreases. In contrast to differentially pumped hollow-core capillary post-compression setups in the normal dispersion regime [26], the optimal pressure gradient direction in our case is opposite. In the positive dispersion regime the pulse intensity decreases during propagation due to losses, while our case is exactly opposite, the pulse intensity increases towards the end of the fiber. The comparison of the dependence of the spectrum evolution in case of uniformly filled and pressure gradient case shown in Fig. 8.19 panels b) and c) was done by measuring the spectrum at the output of the fiber in ambient air and when the chamber was evacuated. Due to pressure gradient most of the nonlinear interaction is concentrated in the beginning of the fiber thus effectively shortening the interaction length and increasing corresponding soliton order. In other words, because the highest gas pressure is present only at the fibre input and the pressure at the output is 0, the effective interaction length in the vacuum-terminated case is roughly halved compared to static cell case. Correspondingly, the pulse energy at which the optimum pulse spectral broadening and the pulse compression are expected are significantly increased from 65 to 100 μJ . The broadest spectrum in the case of a pressure gradient shown in Fig. 8.19 d) exhibit notable increase of the blue side of the spectrum indicating a shorter transient generation of the self-compressed pulse.

Temporal characterization the pulse compression in a fiber filled with Xenon gas was done using SEA-SPIDER technique [116], the pulse duration and peak power dependence on the input pulse energy is shown in Fig. 8.20 a). At optimum input pulse energy the pulse self-compresses from 80 fs down to single optical cycle regime. The Fig. 8.20 b) shows two temporal pulse

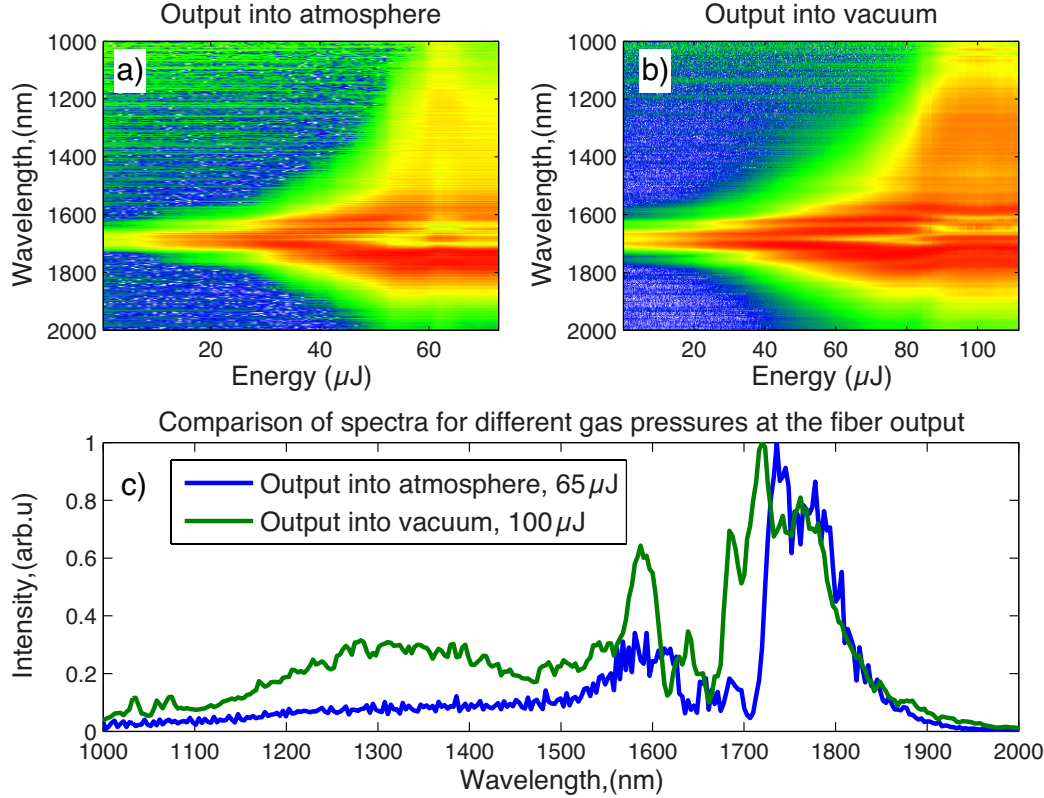


Figure 8.19: Self-compression in a differentially pumped Kagome fiber. Panels a) and b) show the measured spectral evolution at the output pulse as a function of input pulse energy in case of atmospheric pressure at the output (almost no pressure gradient) and vacuum (large pressure gradient) respectively. c) comparison of broadest spectra in case of small and large pressure gradient in the fiber.

profiles and illustrates the control of the self-compressed pulse duration by changing the input pulse energy.

The characteristic measured HHG spectra using self-compressed driver pulses are shown in Fig 8.20 c). Discrete harmonic peaks are observed when input pulses are of lower energy and self-compression yields longer, multi-cycle pulses. When the input pulse energy is increased, the pulse shortens to the single cycle regime and the number of emitted XUV bursts decreases leading to near-vanishing harmonic peak modulation. An additional cross-check against artifacts due to visible stray light on the CCD detector was made by inserting a glass plate into the XUV beam path which absorbs the XUV radiation but transmits the visible background. Even though, the CEP

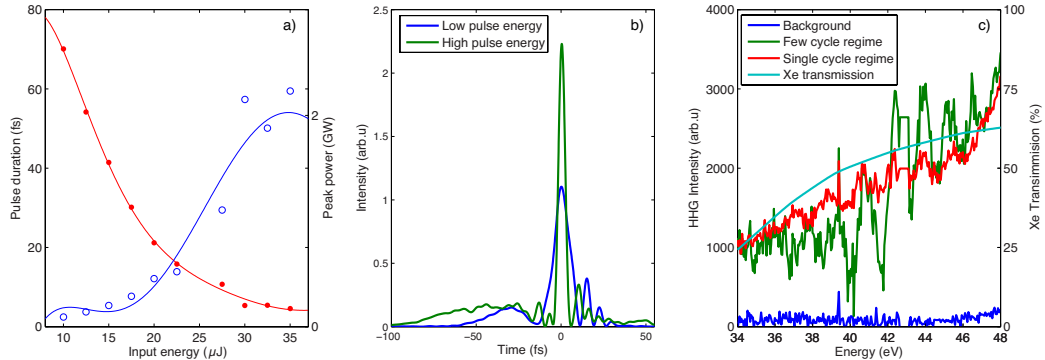


Figure 8.20: a) self-compressed pulse duration and peak power dependence on the input pulse energy measured with SEA-SPIDER technique, b) comparison of corresponding temporal pulse profiles, where lower input pulse energy (27.5 μJ) yields multi-cycle self-compressed pulse (blue line), and at higher input pulse energy (30 μJ) pulse shortens close to one optical cycle (green line). c) measured HHG spectra corresponding to different self-compressed pulse durations. The red curve shows nearly vanishing harmonic peak modulation which is due to reduction of the number of emitted XUV bursts. The light green curve shows XUV transmission through Xenon medium which is responsible for the increased losses at lower photon energies.

of the driving pulses was not locked in this case, the preliminary high-order harmonic generation results clearly shows the potential of the scheme for implementation of a compact isolated attosecond pulse generation setup.

8.9 Spectral broadening in a positive dispersion regime

In order to illustrate the flexibility of the pulse compression in Kagome fiber, we demonstrated continuous transition from negative to positive dispersion regime by increasing the filling gas pressure to a very high value. Measurements were done in the positive dispersion regime using rather high 33 bar Krypton pressure and shorter driving pulse wavelength, $\lambda_0 = 1.5 \mu\text{m}$. In this case the spectrum broadens due to SPM and yields positively chirped pulses at the output of the fiber. It was possible to partially compensate the positive dispersion of the broadened pulses due to SPM using simply a glass block, which has a negative dispersion in this spectral region. The spectrum of the broadened pulse and temporal characterization is shown in Figure 8.21. The left column corresponds to the broadened pulse from the fibre and the right

column corresponds to the FROG measurement after ≈ 35 mm of glass was inserted in the beam path. Insertion of the glass partially removed the positive chirp of the broadened spectrum pulses (see the evident slanted Wigner distribution on the left column) and the pulse shortened from initial 40 fs duration down to 26 fs. The positive dispersion regime was not optimized and serves solely as an example of the wide tunability of the dispersion profile.

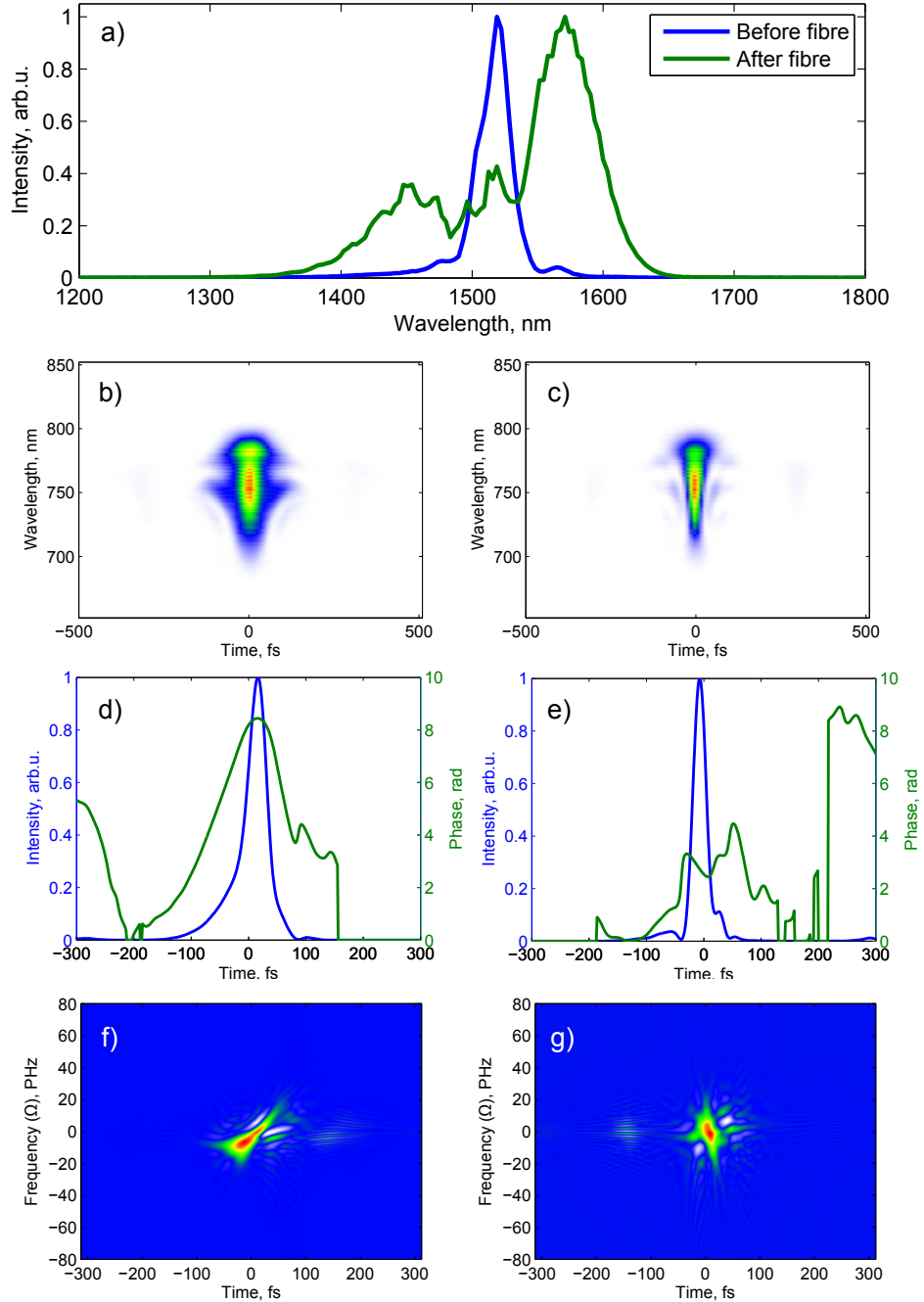


Figure 8.21: Spectral broadening in the positive dispersion regime and compression using a glass block. a) comparison of the input and broadened pulse spectrum. Panels b) - g) show the measured FROG traces, retrieved temporal profiles and Wigner distribution plots for time-frequency analysis. Left and right columns correspond to the pulse before and after 35 mm glass block respectively.

8.10 Summary

In summary, we demonstrate an efficient pulse self-compression scheme based on shock wave formation in an ultrabroadband Kagome lattice fibre. The proposed approach leads to the sub-cycle pulse generation in a relatively simple experimental setup. The scheme is scalable in energy and wavelength and has the potential to answer the demand for energetic sub-cycle sources in many strong-field applications.

List of Publications

Papers:

1. ***T. Balčiūnas**, C. Fourcade-Dutin, G. Fan, T. Witting, A. A. Voronin, A. M. Zheltikov, G. Frederic, G. G. Paulus, A. Baltuška, and F. Benabid, "A strong-field driver in the single-cycle regime based on self-compression in a kagome fibre," *Nature Comm.* **6**, 6117 (2015)
2. ***T. Balčiūnas**, D. Lorenc, M. Ivanov, O. Smirnova, A. M. Zheltikov, D. Dietze, K. Unterrainer, T. Rathje, G. G. Paulus, A. Baltuška, and S. Haessler, "CEP-stable tunable THz-emission originating from laser-waveform-controlled sub-cycle plasma-electron bursts," *Optics Express* **23**, 15278 (2015)
3. ***T. Balčiūnas**, T. Flöry, A. Baltuška, T. Stanislauskas, R. Antipenkov, A. Varanavičius, and G. Steinmeyer, „Direct carrier-envelope phase control of an amplified laser system,“ *Optics Letters* **39**, 1669 (2014).
4. ***T. Balčiūnas**, G. Y. Fan, G. Andriukaitis, A. Pugžlys and A. Baltuška, „High Power Top-Hat Pulses From an Yb MOPA for Efficient OPA Pumping“, *Optics Letters* **36**, 3242–3244 (2012).
5. ***T. Balčiūnas**, O. D. Mücke, P. Mišeikis, G. Andriukaitis, A. Pugžlys, L. Giniunas, R. Danielius, R. Holzwarth and A. Baltuška, „Carrier envelope phase stabilization of a Yb:KGW laser amplifier,“ *Optics Letters* **36**, 3242-3244 (2011)
6. *(Book chapter) **T. Balčiūnas**, A.J. Verhoef, S. Haessler, A.V. Mitrofanov, G. Fan, E.E. Serebryannikov, M.Y. Ivanov, A.M. Zheltikov, and A. Baltuška, “Strong field ionization in a multi-color field”, Springer, 'Trends of Attosciences', edited by A. Zair.
7. **T. Balčiūnas**, A. Melninkaitis, A. Vanagas, and V. Sirutkaitis, "Tilted pulse time-resolved off-axis digital holography," *Optics Letters* **34**, 2715-2717 (2009)

8. **T. Balčiūnas**, A. Melninkaitis, G. Tamosauskas, and V. Sirutkaitis, "Time-resolved off-axis digital holography for characterization of ultrafast phenomena in water," *Optics Letters* **33**, 58-60 (2008).
9. **T. Balčiūnas**, G. Fan, S. Haessler, C. Fourcade-Dutin, T. Witting, A.A. Voronin, A.M. Zheltikov, F. G er ome, G.G. Paulus, A. Baltuška and F. Benabid, "Strong Field Applications of Gigawatt Self-compressed Pulses from a Kagome Fiber," *Ultrafast Phenomena XIX Springer Proceedings in Physics* **162**, Chapter 3, 11 (2015)
10. ***T. Balčiūnas**, S. Haessler, G. Fan, G. Andriukaitis, A. Pugžlys, A. Baltuška, A. Zair, R. Squibb, L. Chipperfield, L. Frasiniski, J. Tisch, J. Marangos, "Toward a "Perfect-Wave" HHG Driving With a Multi-color OPA," *Proceedings of XVIIIth International Conference on Ultrafast Phenomena*, Lausanne, Switzerland, July 8-13, 2012 Edited by M. Chergui, A. Taylor, S. Cundiff, R. de Vivie-Riedle and K. Yamanouchi
11. ***T. Balčiūnas**, O. D. M ucke, A. J. Verhoef, A. Pugžlys, A. Baltuška, D. Mikalauskas, L. Giniūnas, R. Danielius, M. Lezius, and R. Holzwarth, "Cycle engineering for coherent steering of electrons with a sub-mJ optical parametric synthesizer," *Proceedings of the 17th International Conference*, Snowmass, Colorado, US, July 18-23, 2010 Edited by Majed Chergui, David Jonas, Eberhard Riedle, Robert Schoenlein, and Antoinette Taylor
12. ***T. Balčiūnas**, D. Lorenc, M. Ivanov, O. Smirnova, A. Pugžlys, A. M. Zheltikov, D. Dietze, J. Darmo, K. Unterrainer, T. Rathje, G. Paulus, A. Baltuška, "Tunability of THz Emission Originating from Sub-Cycle Electron Bursts in a Laser Induced Plasma," *Proceedings of the 17th International Conference*, Snowmass, Colorado, US, July 18-23, 2010 Edited by Majed Chergui, David Jonas, Eberhard Riedle, Robert Schoenlein, and Antoinette Taylor
13. S. Haessler, **T. Balčiūnas**, G. Fan, G. Andriukaitis, A. Pugžlys, and A. Baltuška, T. Witting, R. Squibb, A. Za ir, J. W. G. Tisch, and J. P. Marangos, and L. Chipperfield, "Optimization of Quantum Trajectories Driven by Strong-Field Waveforms", *Physical Review X* **4**, 021028 (2014)
14. S. Haessler, **T. Balčiūnas**, G. Fan, L. E. Chipperfield, and A. Baltuška, "Enhanced multi-colour gating for the generation of high-power isolated attosecond pulses," *Scientific Reports* **5**, 10084 (2015)

15. T. Popmintchev, M. C. Chen, D. Popmintchev, P. Arpin, S. Brown, S. Ališauskas, G. Andriukaitis, **T. Balčiūnas**, O. D. Mucke, A. Pugžlys, A. Baltuška, B. Shim, S. E. Schrauth, A. Gaeta, C. Hernandez-Garcia, L. Plaja, A. Becker, A. Jaron-Becker, M. M. Murnane, and H. C. Kapteyn, "Bright Coherent Ultrahigh Harmonics in the keV X-ray Regime from Mid-Infrared Femtosecond Lasers," *Science* **336**, 1287–1291 (2012)
16. P. Stajanca, D. Pysz, G. Andriukaitis, **T. Balčiūnas**, G. Fan, A. Baltuska, and I. Bugar "Ultrafast multi-wavelength switch based on dynamics of spectrally-shifted solitons in a dual-core photonic crystal fiber," *Optics Express* **22**, 31092-31101 (2014)
17. G. Andriukaitis, **T. Balčiūnas**, S. Ališauskas, A. Pugžlys, A. Baltuška, T. Popmintchev, M. Chen, M. M. Murnane, and H. C. Kapteyn, „90 GW peak power few-cycle mid-infrared pulses from an optical parametric amplifier“, *Optics Letters* **36**, 2755-2757 (2011)
18. E. Brasselet, **T. Balčiūnas**, N. Murazawa, S. Juodkazis, and H. Misawa, „Light-induced nonlinear rotations of nematic liquid crystal droplets trapped in laser tweezers“, *Molecular Crystals and Liquid Crystals* **512**, 143-151 (2009)
19. A. Melninkaitis, **T. Balčiūnas**, V. Sirutkaitis, V. Juzumas, J. Janusonis, and G. Sleky "Formation of grooves in SiO₂ coated silicon using femtosecond ytterbium DPSS laser", *Proc. SPIE* **7005**, 70050L (2008)
20. Melninkaitis, D. Miksys, **T. Balčiūnas**, O. Balachninaite, T. Rakickas, R. Grigonis, and V. Sirutkaitis, "Automated test station for laser-induced damage threshold measurements according to ISO 11254-2 standard", *Proceedings of the SPIE* **6101**, 377-386 (2006)
21. Melninkaitis, D. Miksys, **T. Balčiūnas**, V. Sirutkaitis, A. Skrebutenas, R. Buzelis, G. Abromavicius, R. Drazdys, "Effect of substrate temperature and ion assistance on nanosecond laser-induced damage threshold in high reflection dielectric coatings", *Proceedings of SPIE* **5991**, 59911B, (2005)

Selected list of my presentations at international conferences:

1. (Talk) **T. Balčiūnas**, G. Fan, S. Haessler, C. Fourcade-Dutin, T. Witting, A.A. Voronin, A.M. Zheltikov, F. Gérôme, G.G. Paulus, A. Baltuška and F. Benabid, "Strong Field Applications of Gigawatt Self-compressed Pulses from a Kagome Fiber", *Ultrafast Phenomena XIX*, July 7-11, 2014, Okinawa, Japan,

2. (Invited talk) T. **Balčiūnas**, T. Flöry, A. Baltuška, T. Stanislauskas, R. Antipenkov, A. Varanavičius, and G. Steinmeyer, „Direct Carrier-Envelope Phase Control of a sub-MHz Yb amplifier“, HILAS (High Intensity Lasers and Applications), March 18-20, 2014, Berlin, Germany
3. (Talk) T. **Balčiūnas**, C. Fourcade-Dutin, G. Fan, T. Witting, A.A. Voronin, A. M. Zheltikov, G. Frédéric, G.G. Paulus, A. Baltuška and F. Benabid, “Sub-Cycle Gigawatt Peak Power Pulses Self-Compressed by Optical Shock Waves”, HILAS (High Intensity Lasers and Applications), March 18-20, 2014, Berlin, Germany
4. (Best student oral presentation award) T. **Balčiūnas**, T. Flöry, T. Stanislauskas, R. Antipenkov, A. Varanavicius, A. Baltuška, and G. Steinmeyer, "Direct carrier-envelope phase control of an amplified laser system", Ultrafast Optics IX, March 4-8 2013, Davos, Switzerland
5. (Post-deadline talk), T. **Balčiūnas**, G. Y. Fan, G. Andriukaitis, A. Pugžlys and A. Baltuška, “High power top-hat pulses from an Yb MOPA for efficient OPA pumping”, Advanced Solid-State Photonics (ASSP), 29 January - 1 February 2012, San Diego, California, USA
6. (Talk) T. **Balčiūnas**, G. Andriukaitis, A. Pugžlys, A. Baltuška, P. Mišeikis, L. Giniunas, R. Danielius, L. Hand and R. Holzwarth, “CEP stabilization of a cascaded high-energy Yb amplifier chain”, Advanced Solid-State Photonics (ASSP), 29 January - 1 February 2012, San Diego, California, USA
7. (Invited talk) T. **Balčiūnas**, G. Andriukaitis, A. Pugžlys, A. Baltuška, O. Smirnova, M. Yu. Ivanov, A.M. Zheltikov, T. Rathje, G. Paulus, “Steering of Tunneling Currents by Sub-Cycle Waveform Shaping”, IEEE photonics society 23rd annual meeting, November 7-11, 2010 Denver, CO, USA
8. (Invited talk) T. **Balčiūnas**, O. D. Mücke, A. J. Verhoef, A. Pugžlys, A. Baltuška, D. Mikalauskas, L. Giniūnas, R. Danielius, M. Lezius, and R. Holzwarth, “Cycle engineering for coherent steering of electrons with a sub-mJ optical parametric synthesizer”, Ultrafast Phenomena 2010, July 18-23, 2010, Snowmass Village, Colorado, USA
9. (Post-deadline talk) T. **Balčiūnas**, D. Lorenc, M. Ivanov, O. Smirnova, A. Pugžlys, A. M. Zheltikov, D. Dietze, J. Darmo, K. Unterrainer, T.

Rathje, G. Paulus, A. Baltuška, “Tunability of THz Emission Originating from Sub-Cycle Electron Bursts in a Laser Induced Plasma”, Ultrafast Phenomena 2010, July 18-23, 2010, Snowmass Village, Colorado, USA

10. (Invited talk) T. **Balčiūnas**, D. Lorenc, A. Pugžlys, D. Dietze, J. Darmo, K. Unterrainer, A. Baltuška, T. Rathje, G. Paulus, “Tunability of THz Emission in a Laser Induced Plasma”, ICONO/LAT 2010, August 22-26, 2010, Kazan, Russia
11. (Talk) S. Haessler, T. **Balčiūnas**, G. Andriukaitis, O. D. Mücke, A. Pugžlys, A. Baltuška, R. Squibb, L. Frasinski, J. Marangos, J. W. G. Tisch, L. Giniūnas, R. Danielius, and R. Holzwarth, “Multicolor optical parametric synthesizer for high-field science”, HILAS (High Intensity Lasers and Applications), February 14-18, 2011, Istanbul, Turkey
12. (Post-deadline presentation) T. **Balčiūnas**, A. Melninkaitis, A. Vana-gas, and V. Sirutkaitis, „Femtosecond Time-Resolved Off-Axis Digital Holography,“ Digital Holography and Three-Dimensional Imaging, April 27-29, 2009, Vancouver, BC, Canada.
13. (Talk) T. **Balčiūnas**, A. Melninkaitis, G. Tamošauskas, and V. Sirutkaitis, „Time-resolved off-axis digital holography for characterization of ultra-fast phenomena in water,“ Ultrafast Phenomena 2008, June 9-13, 2008, Stresa, Italy.

* Papers included in this thesis

Abbreviations

ADK	M. V. Ammosov, N. B. Delone and V. P. Krainov formalism
AOFS	Acousto-Optic Frequency Shifter
AOM	Acousto-Optic Modulator
AOPDF	Acousto-Optic Programmable Dispersive Filter
ASE	Amplified Spontaneous Emission
ATI	Above Threshold Ionization
BBO	Beta Baryum Oxyde
BPF	Band-Pass Filter
C-C	Continuum-Continuum
CEP	Carrier-Envelope Phase
CPA	Chirped Pulse Amplification
CW	Continuous Wave
DPSS(L)	Diode-Pumped Solid-State (Laser)
DSO	Digital Storage Oscilloscope
EO	Electro-Optical
FFT	Fast Fourier Transform
FROG	Frequency Resolved Optical Gating
FWHM	Full Width at Half Maximum
GD	Group Delay
GDD	Group Delay Dispersion
GVD	Group Velocity Dispersion
HC	Hollow Core
HHG	High-Harmonic Generation
IF	Intermediate Frequency
IR	Infra Red
KTA	Potassium Titanyle Arsenate
LO	Local Oscillator
LPMM	Lines per millimeter
MCP	Micro Channel Plate detector
MOPA	Master Oscillator Power Amplifier
OL	Out-of-Loop

OPA	Optical Parametric Amplifier
OPCPA	Optical Parametric Chirped Pulse Amplification
OSA	Optical Spectrum Analyzer
OSC	Oscillator
PBG	Photonic Band-Gap
PCF	Photonic Crystal Fibre
PLL	Phase-Locked Loop
PPT	A. M. Perelomov, V. S. Popov and M. V. Terent'ev formalism
PSD	Power Spectral Density
r.m.s.	Root Mean Square
RA	Regenerative Amplifier
RF	Radio Frequency
SEM	Scanning Electron Microscope
SF57	Dense flint glass
SFA	Strong Field Approximation
SHG	Second Harmonic Generation
SPIDER	Spectral Phase Interferometry for Direct Electric-field Reconstruction
SPM	Self Phase Modulation
TDSE	Time-Dependent Schrödinger Equation
TOF	Time Of Flight
VCO	Voltage-Controlled Oscillator
XUV	eXtreme Ultra Violet
Yb:CaF ₂	Ytterbium doped Calcium Fluoride
YDFA	Ytterbium-Doped Fiber Amplifier

Bibliography

- [1] F. Krausz and M. Ivanov, “Attosecond physics,” *Reviews of Modern Physics* **81**(1), 163–234 (2009).
- [2] L. Keldysh, “Ionization in the field of a strong electromagnetic wave,” *Sov. Phys. JETP* **20**, 1307–1314 (1965).
- [3] P. Agostini, F. Fabre, G. Mainfray, G. Petite, and N. K. Rahman, “Free-Free Transitions Following Six-Photon Ionization of Xenon Atoms,” *Physical Review Letters* **42**(17), 1127–1130 (1979).
- [4] M. D. Thomson, M. Kress, T. Loeffler, and H. G. Roskos, “Broadband THz emission from gas plasmas induced by femtosecond optical pulses: From fundamentals to applications,” *Laser & Photonics Reviews* **1**(4), 349–368 (2007).
- [5] P. B. Corkum, “Plasma perspective on strong field multiphoton ionization,” *Physical Review Letters* **71**(13), 1994–1997 (1993).
- [6] J. L. Krause, K. J. Schafer, and K. C. Kulander, “High-order harmonic generation from atoms and ions in the high intensity regime,” *Physical Review Letters* **68**(24), 3535–3538 (1992).
- [7] A. Baltuška, T. Fuji, and T. Kobayashi, “Visible pulse compression to 4 fs by optical parametric amplification and programmable dispersion control,” *Opt. Lett* **27**(5), 306–308 (2002).
- [8] R. Bartels, S. Backus, E. Zeek, L. Misoguti, G. Vdovin, I. Christov, M. Murnane, and H. Kapteyn, “Shaped-pulse optimization of coherent emission of high-harmonic soft X-rays,” *Nature* **406**(6792), 164–166 (2000).
- [9] Z. Chang, A. Rundquist, H. Wang, I. Christov, H. Kapteyn, and M. Murnane, “Temporal phase control of soft-x-ray harmonic emission,” *Physical Review A* **58**(1), R30–R33 (1998).
- [10] A. Baltuška, M. Uiberacker, E. Goulielmakis, R. Kienberger, V. S. Yakovlev, T. Udem, T. W. Hänsch, and F. Krausz, “Phase-Controlled Amplification of Few-Cycle Laser Pulses,” *IEEE Jnl. on Sel. Topics in Quant. Elect.* **9**(4), 972–989 (2003).
- [11] F. Calegari, C. Vozzi, M. Negro, G. Sansone, F. Frassetto, L. Poletto, P. Villoresi, M. Nisoli, S. De Silvestri, and S. Stagira, “Efficient continuum generation exceeding 200 eV by intense ultrashort two-color driver.” *Optics Letters* **34**(20), 3125 (2009).
- [12] G. Cerullo and S. De Silvestri, “Ultrafast optical parametric amplifiers,” *Review of Scientific Instruments* **74**(1), 1 (2003).

-
- [13] G. Cerullo, A. Baltuška, O. D. Mücke, and C. Vozzi, “Few-optical-cycle light pulses with passive carrier-envelope phase stabilization,” *Laser and Photonics Reviews* **5**(3), 323–351 (2011).
- [14] M. Y. Ivanov, M. Spanner, and O. Smirnova, “Anatomy of strong field ionization,” *Journal of Modern Optics* **52**(2), 165–184 (2005).
- [15] A. Perelomov, V. Popov, and M. Terent’ev, “Ionization of atoms in an alternating electric field,” *Soviet Physics JETP* **23**(5), 924–934 (1966).
- [16] O. Smirnova, A. S. Mouritzen, S. Patchkovskii, and M. Y. Ivanov, “Coulomb–laser coupling in laser-assisted photoionization and molecular tomography,” *Journal of Physics B: Atomic, Molecular and Optical Physics* **40**(13), F197 (2007).
- [17] M. Ammosov, N. Delone, and V. Krainov, “Tunnel ionization of complex atoms and of atomic ions in an alternating electromagnetic field,” *Soviet Physics JETP* **64**(6), 1191–1194 (1986).
- [18] G. Yudin and M. Ivanov, “Nonadiabatic tunnel ionization: Looking inside a laser cycle,” *Physical Review A* **64**(1), 6–9 (2001).
- [19] P. Zhokhov and A. Zheltikov, “Field-cycle-resolved photoionization in solids,” *Physical Review Letters* **113**(13), 133,903 (2014).
- [20] M. Uiberacker, T. Uphues, M. Schultze, A. J. Verhoef, V. Yakovlev, M. F. Kling, J. Rauschenberger, N. M. Kabachnik, H. Schröder, M. Lezius, K. L. Kompa, H.-G. Muller, M. J. J. Vrakking, S. Hendel, U. Kleineberg, U. Heinzmann, M. Drescher, and F. Krausz, “Attosecond real-time observation of electron tunnelling in atoms.” *Nature* **446**(7136), 627–632 (2007).
- [21] C. DeMichelis, “Laser induced gas breakdown,” *IEEE Journal of Quantum Electronics* **5**(4), 188–202 (1969).
- [22] M. Schulz, R. Riedel, A. Willner, T. Mans, C. Schnitzler, P. Russbuedt, J. Dolkemeyer, E. Seise, T. Gottschall, S. Hädrich, S. Duesterer, H. Schlarb, J. Feldhaus, J. Limpert, B. Faatz, A. Tünnermann, J. Rossbach, M. Drescher, and F. Tavella, “Yb:YAG Innoslab amplifier: efficient high repetition rate subpicosecond pumping system for optical parametric chirped pulse amplification.” *Optics Letters* **36**(13), 2456–2458 (2011).
- [23] M. Krebs, S. Hädrich, S. Demmler, J. Rothhardt, A. Zair, L. Chipperfield, J. Limpert, and A. Tünnermann, “Towards isolated attosecond pulses at megahertz repetition rates,” *Nature Photonics* **7**(7), 555–559 (2013).
- [24] E. J. Takahashi, T. Kanai, K. L. Ishikawa, Y. Nabekawa, and K. Midorikawa, “Coherent water window X ray by phase-matched high-order harmonic generation in neutral media,” *Physical review letters* **101**(25), 253,901 (2008).
- [25] T. Popmintchev, M.-C. Chen, D. Popmintchev, P. Arpin, S. Brown, S. Ališauskas, G. Andriukaitis, T. Balčiūnas, O. D. Mücke, A. Pugžlys, A. Baltuška, B. Shim, S. E. Schrauth, A. Gaeta, C. Hernández-García, L. Plaja, A. Becker, A. Jaron-Becker, M. M. Murnane, and H. C. Kapteyn, “Bright Coherent Ultrahigh Harmonics in the keV X-ray Regime from Mid-Infrared Femtosecond Lasers,” *Science* **336**(6086), 1287–1291 (2012).

- [26] M. Nisoli, S. D. Silvestri, and O. Svelto, "Generation of high energy 10 fs pulses by a new pulse compression technique," *Applied Physics Letters* **68**(20), 2793–2795 (1996).
- [27] P. Corkum and F. Krausz, "Attosecond science," *Nature Physics* **3**(6), 381–387 (2007).
- [28] E. Goulielmakis, V. Yakovlev, A. Cavalieri, M. Uiberacker, V. Pervak, A. Apolonski, R. Kienberger, U. Kleineberg, and F. Krausz, "Attosecond Control and Measurement: Lightwave Electronics," *Science* **317**(5839), 769–775 (2007).
- [29] T. Uphues, M. Schultze, M. Kling, M. Uiberacker, S. Hendel, U. Heinzmann, N. Kabachnik, and M. Drescher, "Ion-charge-state chronoscopy of cascaded atomic Auger decay," *New J. Phys.* **10**(2), 25,009 (2008).
- [30] A. Cavalieri, N. Muller, T. Uphues, V. Yakovlev, A. Baltuška, B. Horvath, B. Schmidt, L. Blumel, R. Holzwarth, S. Hendel, M. Drescher, U. Kleineberg, P. Echenique, R. Kienberger, F. Krausz, and U. Heinzmann, "Attosecond spectroscopy in condensed matter," *Nature* **449**(7165), 1029–1032 (2007).
- [31] A. J. Verhoef, A. V. Mitrofanov, E. E. Serebryannikov, D. V. Kartashov, A. M. Zheltikov, and A. Baltuška, "Optical Detection of Tunneling Ionization," *Physical Review Letters* **104**(16), 163,904 (2010).
- [32] F. Brunel, "Harmonic generation due to plasma effects in a gas undergoing multi-photon ionization in the high-intensity limit," *J. Opt. Soc. Am. B* **7**(4), 521–526 (1990).
- [33] M. Kress, T. Löffler, S. Eden, M. Thomson, and H. G. Roskos, "Terahertz-pulse generation by photoionization of air with laser pulses composed of both fundamental and second-harmonic waves," *Optics Letters* **29**(10), 1120–1122 (2004).
- [34] D. Milosević, G. Paulus, and W. Becker, "High-order above-threshold ionization with few-cycle pulse: a meter of the absolute phase," *Optics Express* **11**(12), 1418–1429 (2003).
- [35] D. B. Milošević, G. G. Paulus, D. Bauer, and W. Becker, "Above-threshold ionization by few-cycle pulses," *Journal of Physics B: Atomic, Molecular and Optical Physics* **39**(14), R203–R262 (2006).
- [36] T. Wittmann, B. Horvath, W. Helml, M. G. Schatzel, X. Gu, a. L. Cavalieri, G. G. Paulus, and R. Kienberger, "Single-shot carrier-envelope phase measurement of few-cycle laser pulses," *Nature Physics* **5**(5), 357–362 (2009).
- [37] K. Y. Kim, A. J. Taylor, J. H. Glowina, and G. Rodriguez, "Coherent control of terahertz supercontinuum generation in ultrafast laser-gas interactions," *Nature Photonics* **2**(10), 605–609 (2008).
- [38] N. Karpowicz and X.-C. Zhang, "Coherent Terahertz Echo of Tunnel Ionization in Gases," *Physical Review Letters* **102**(9), 093,001 (2009).
- [39] Z. Zhou, D. Zhang, Z. Zhao, and J. Yuan, "Terahertz emission of atoms driven by ultrashort laser pulses," *Phys. Rev. A* **79**(6), 063,413 (2009).
- [40] T. Balčiūnas, A. Verhoef, A. Mitrofanov, G. Fan, E. Serebryannikov, M. Ivanov, A. Zheltikov, and A. Baltuška, "Optical and THz signatures of sub-cycle tunneling dynamics," *Chemical Physics* **414**(0), 92–99 (2013).

-
- [41] C. Siders, G. Rodriguez, J. Siders, F. Omenetto, and A. Taylor, “Measurement of Ultrafast Ionization Dynamics of Gases by Multipulse Interferometric Frequency-Resolved Optical Gating,” *Physical Review Letters* **87**(26), 263,002 (2001).
- [42] D. J. Cook and R. M. Hochstrasser, “Intense terahertz pulses by four-wave rectification in air,” *Optics Letters* **25**(16), 1210–1212 (2000).
- [43] T. Balčiūnas, D. Lorenc, M. Ivanov, O. Smirnova, A. Pugžlys, A. M. Zheltikov, D. Dietze, J. Darmo, K. Unterrainer, T. Rathje, G. G. Paulus, and A. Baltuška, “Tunability of THz Emission Originating from Sub-Cycle Electron Bursts in a Laser Induced Plasma,” in *International Conference on Ultrafast Phenomena*, p. PDP4 (Optical Society of America, 2010).
- [44] N. Dudovich, O. Smirnova, J. Levesque, Y. Mairesse, M. Y. Ivanov, D. M. Villeneuve, and P. B. Corkum, “Measuring and controlling the birth of attosecond XUV pulses,” *Nature Physics* **2**(11), 781–786 (2006).
- [45] E. J. Takahashi, P. Lan, O. D. Mücke, Y. Nabekawa, and K. Midorikawa, “Infrared Two-Color Multicycle Laser Field Synthesis for Generating an Intense Attosecond Pulse,” *Physical Review Letters* **104**, 233,901 (2010).
- [46] G. Paulus, F. Grasbon, H. Walther, P. Villoresi, M. Nisoli, S. Stagira, E. Priori, and S. De Silvestri, “Absolute-phase phenomena in photoionization with few-cycle laser pulses,” *Nature* **414**(6860), 182–184 (2001).
- [47] S. Haessler, T. Balčiūnas, G. Fan, G. Andriukaitis, A. Pugžlys, A. Baltuška, T. Witting, R. Squibb, A. Zair, J. W. G. Tisch, J. P. Marangos, and L. E. Chipperfield, “Optimization of Quantum Trajectories Driven by Strong-Field Waveforms,” *Phys. Rev. X* **4**, 021,028 (2014).
- [48] L. E. Chipperfield, J. S. Robinson, J. W. G. Tisch, and J. P. Marangos, “Ideal Waveform to Generate the Maximum Possible Electron Recollision Energy for Any Given Oscillation Period,” *Physical Review Letters* **102**(6), 063,003 (2009).
- [49] O. Smirnova, Y. Mairesse, S. Patchkovskii, N. Dudovich, D. Villeneuve, P. Corkum, and M. Y. Ivanov, “High harmonic interferometry of multi-electron dynamics in molecules.” *Nature* **460**(7258), 972–977 (2009).
- [50] C. Vozzi, F. Calegari, F. Frassetto, L. Poletto, G. Sansone, P. Villoresi, M. Nisoli, S. De Silvestri, and S. Stagira, “Coherent continuum generation above 100 eV driven by an ir parametric source in a two-color scheme,” *Physical Review A* **79**(3), 033,842 (2009).
- [51] S. Haessler, T. Balčiūnas, G. Fan, L. E. Chipperfield, and A. Baltuška, “Enhanced multi-colour gating for the generation of high-power isolated attosecond pulses,” *Scientific reports* **5** (2015).
- [52] S. Haessler, J. Caillat, W. Boutu, C. Giovanetti-Teixeira, T. Ruchon, T. Auguste, Z. Diveki, P. Breger, a. Maquet, B. Carré, R. Taïeb, and P. Salières, “Attosecond imaging of molecular electronic wavepackets,” *Nature Physics* **6**(3), 200–206 (2010).
- [53] D. Shafir, H. Soifer, B. D. Bruner, M. Dagan, Y. Mairesse, S. Patchkovskii, M. Y. Ivanov, O. Smirnova, and N. Dudovich, “Resolving the time when an electron exits a tunnelling barrier,” *Nature* **485**(7398), 343–346 (2012).

- [54] A. L’Huillier, M. Lewenstein, P. Salières, P. Balcou, M. Y. Ivanov, J. Larsson, and C. G. Wahlström, “High-order Harmonic-generation cutoff,” *Phys. Rev. A* **48**(5), R3433–R3436 (1993).
- [55] P. Balcou, P. Salières, A. L’Huillier, and M. Lewenstein, “Generalized phase-matching conditions for high harmonics: The role of field-gradient forces,” *Physical Review A* **55**(4), 3204–3210 (1997).
- [56] M. Ferray, A. L’Huillier, X. F. Li, L. A. Lompre, G. Mainfray, and C. Manus, “Multiple-harmonic conversion of 1064 nm radiation in rare gases,” *Journal of Physics B: Atomic, Molecular and Optical Physics* **21**(3), L31–L35 (1988).
- [57] Z. Chang, A. Rundquist, H. Wang, M. M. Murnane, and H. C. Kapteyn, “Generation of coherent soft X rays at 2.7 nm using high harmonics,” *Physical Review Letters* **79**(16), 2967 (1997).
- [58] S. Kubodera, Y. Nagata, Y. Akiyama, K. Midorikawa, M. Obara, H. Tashiro, and K. Toyoda, “High-order harmonic generation in laser-produced ions,” *Physical Review A* **48**(6), 4576 (1993).
- [59] a. Shiner, C. Trallero-Herrero, N. Kajumba, H.-C. Bandulet, D. Comtois, F. Légaré, M. Giguère, J.-C. Kieffer, P. Corkum, and D. Villeneuve, “Wavelength Scaling of High Harmonic Generation Efficiency,” *Physical Review Letters* **103**(7), 1–4 (2009).
- [60] T. Popmintchev, M.-C. Chen, A. Bahabad, M. Gerrity, P. Sidorenko, O. Cohen, I. P. Christov, M. M. Murnane, and H. C. Kapteyn, “Phase matching of high harmonic generation in the soft and hard X-ray regions of the spectrum,” *Proceedings of the National Academy of Sciences* **106**(26), 10,516–10,521 (2009).
- [61] M. Shapiro and P. Brumer, “Coherent control of atomic, molecular, and electronic processes,” *Advances in Atomic Molecular and Optical Physics* **42**, 287–345 (2000).
- [62] A. Wirth, M. T. Hassan, I. Grguraš, J. Gagnon, A. Moulet, T. T. Luu, S. Pabst, R. Santra, Z. A. Alahmed, A. M. Azzeer, V. S. Yakovlev, V. Pervak, F. Krausz, and E. Goulielmakis, “Synthesized Light Transients,” *Science* **334**(6053), 195–200 (2011).
- [63] S.-W. Huang, G. Cirmi, J. Moses, K.-H. Hong, S. Bhardwaj, J. R. Birge, L.-J. Chen, E. Li, B. J. Eggleton, G. Cerullo, *et al.*, “High-energy pulse synthesis with sub-cycle waveform control for strong-field physics,” *Nature photonics* **5**(8), 475–479 (2011).
- [64] A. Baltuška, T. Udem, M. Uiberacker, M. Hentschel, E. Goulielmakis, C. Gohle, R. Holzwarth, V. Yakovlev, A. Scrinzi, T. Hansch, and F. Krausz, “Attosecond control of electronic processes by intense light fields,” *Nature* **421**(6923), 611–615 (2003).
- [65] A. Baltuška, T. Fuji, and T. Kobayashi, “Controlling the Carrier-Envelope Phase of Ultrashort Light Pulses with Optical Parametric Amplifiers,” *Physical Review Letters* **88**(13), 133,901 (2002).
- [66] A. Pugžlys, G. Andriukaitis, A. Baltuška, L. Su, J. Xu, H. Li, R. Li, W. J. Lai, P. B. Phua, A. Marcinkevičius, M. E. Fermann, L. Giniūnas, R. Danielius, and S. Alšauskas, “Multi-mJ, 200-fs, cw-pumped, cryogenically cooled, Yb,Na:CaF₂ amplifier,” *Optics Letters* **34**(13), 2075–2077 (2009).

- [67] T. Balčiūnas, O. D. Mücke, P. Mišeikis, G. Andriukaitis, A. Pugžlys, L. Giniūnas, R. Danielius, R. Holzwarth, and A. Baltuška, “Carrier envelope phase stabilization of a Yb:KGW laser amplifier,” *Optics Letters* **36**(16), 3242–3244 (2011).
- [68] M. Lewenstein, P. Balcou, M. Y. Ivanov, A. L’Huillier, and P. B. Corkum, “Theory of high-harmonic generation by low-frequency laser fields,” *Phys. Rev. A* **49**(3), 2117–2132 (1994).
- [69] A. Baltuška, M. Uiberacker, E. Goulielmakis, R. Kienberger, V. Yakovlev, T. Udem, T. Hansch, and F. Krausz, “Phase-controlled amplification of few-cycle laser pulses,” *Selected Topics in Quantum Electronics, IEEE Journal of* **9**(4), 972 – 989 (2003).
- [70] A. Pugžlys, G. Andriukaitis, D. Sidorov, A. Irshad, A. Baltuška, W. J. Lai, P. B. Phua, L. Su, J. Xu, H. Li, R. Li, S. Ališauskas, A. Marcinkevicius, M. E. Fermann, L. Giniūnas, and R. Danielius, “Spectroscopy and lasing of cryogenically cooled Yb, Na:CaF₂,” *Appl. Phys. B* **97**(2), 339–350 (2009).
- [71] P. Kubina, P. Adel, F. Adler, G. Grosche, T. Hänsch, R. Holzwarth, A. Leitenstorfer, B. Lipphardt, and H. Schnatz, “Long term comparison of two fiber based frequency comb systems,” *Optics Express* **13**(3), 904–909 (2005).
- [72] S. A. Meyer, J. A. Squier, and S. A. Diddams, “Diode-pumped Yb : KYW femtosecond laser frequency comb with stabilized carrier-envelope offset frequency,” *European Physical Journal D* **48**(1), 19–26 (2008).
- [73] J. McFerran, W. Swann, B. Washburn, and N. Newbury, “Suppression of pump-induced frequency noise in fiber-laser frequency combs leading to sub-radian f_{ceo} phase excursions,” *Applied Physics B: Lasers and Optics* **86**, 219–227 (2007).
- [74] S. T. Cundiff, “Phase stabilization of ultrashort optical pulses,” *Jnl. of Phys. D: Appl. Phys.* **35**(8), R43–R59 (2002).
- [75] X. D. Wang, P. Basséras, R. J. D. Miller, J. Sweetser, and I. A. Walmsley, “Regenerative pulse amplification in the 10-kHz range,” *Optics Letters* **15**(15), 839–841 (1990).
- [76] T. Fuji, J. Rauschenberger, C. Gohle, A. Apolonski, T. Udem, V. S. Yakovlev, G. Tempea, T. W. Hänsch, and F. Krausz, “Attosecond control of optical waveforms,” *New Jnl. of Phys.* **7**, 116 (2005).
- [77] B. Borchers, S. Koke, A. Husakou, J. Herrmann, and G. Steinmeyer, “Carrier-envelope phase stabilization with sub-10 as residual timing jitter,” *Optics Letters* **36**(21), 4146–4148 (2011).
- [78] F. Lücking, A. Assion, A. Apolonski, F. Krausz, and G. Steinmeyer, “Long-term carrier-envelope-phase-stable few-cycle pulses by use of the feed-forward method,” *Optics Letters* **37**(11), 2076–2078 (2012).
- [79] G. Gademann, F. Plé, P. M. Paul, and M. J. J. Vrakking, “Carrier-envelope phase stabilization of a terawatt level chirped pulse amplifier for generation of intense isolated attosecond pulses,” *Optics Express* **19**(25), 24,922–24,923 (2011).
- [80] C. Gohle, J. Rauschenberger, T. Fuji, T. Udem, A. Apolonski, F. Krausz, and T. W. Hänsch, “Carrier envelope phase noise in stabilized amplifier systems,” *Optics Letters* **30**(18), 2487–2489 (2005).

- [81] O. Pronin, J. Brons, C. Grasse, V. Pervak, G. Boehm, M. C. Amann, V. L. Kalashnikov, A. Apolonski, and F. Krausz, “High-power 200 fs Kerr-lens mode-locked Yb:YAG thin-disk oscillator,” *Optics Letters* **36**(24), 4746–4748 (2011).
- [82] C. J. Saraceno, F. Emaury, O. H. Heckl, C. R. E. Baer, M. Hoffmann, C. Schriber, M. Golling, T. Südmeyer, and U. Keller, “275 W average output power from a femtosecond thin disk oscillator operated in a vacuum environment,” *Optics Express* **20**(21), 23,535–23,541 (2012).
- [83] S. Koke, C. Grebing, B. Manschwetus, and G. Steinmeyer, “Fast f-to-2f interferometer for a direct measurement of the carrier-envelope phase drift of ultrashort amplified laser pulses,” *Optics Letters* **33**(21), 2545–2547 (2008).
- [84] S. Koke, C. Grebing, H. Frei, A. Anderson, A. Assion, and G. Steinmeyer, “Direct frequency comb synthesis with arbitrary offset and shot-noise-limited phase noise,” *Nat. Photonics* **4**(7), 462–465 (2010).
- [85] M. Kakehata, H. Takada, Y. Kobayashi, K. Torizuka, Y. Fujihira, T. Homma, and H. Takahashi, “Single-shot measurement of carrier-envelope phase changes by spectral interferometry,” *Optics Letters* **26**(18), 1436–1438 (2001).
- [86] H. R. Telle, G. Steinmeyer, A. E. Dunlop, J. Stenger, D. H. Sutter, and U. Keller, “Carrier-envelope offset phase control: A novel concept for absolute optical frequency measurement and ultrashort pulse generation,” *Appl. Phys. B* **69**(4), 327–332 (1999).
- [87] M. Pawłowska, F. Ozimek, P. Fita, and C. Radzewicz, “Collinear interferometer with variable delay for carrier-envelope offset frequency measurement,” *Rev. Scient. Instr.* **80**(8), 083,101 (2009).
- [88] B. Borchers, A. Anderson, and G. Steinmeyer, “On the role of shot noise in carrier-envelope phase stabilization,” *Laser & Photonics Reviews* **8**(2), 303–315 (2014).
- [89] A. Dubietis, R. Butkus, and A. P. Piskarskas, “Trends in chirped pulse optical parametric amplification,” *IEEE J Sel Top Quant Electron* **12**(2), 163–172 (2006).
- [90] G. Andriukaitis, T. Balčiūnas, S. Ališauskas, A. Pugžlys, A. Baltuška, T. Popmintchev, M.-C. Chen, M. M. Murnane, and H. C. Kapteyn, “90 GW peak power few-cycle mid-infrared pulses from an optical parametric amplifier,” *Optics Letters* **36**(15), 2755–2757 (2011).
- [91] J. A. Hoffnagle and C. M. Jefferson, “Design and performance of a refractive optical system that converts a Gaussian to a flattop beam,” *Appl. Opt.* **39**(30), 5488–5499 (2000).
- [92] L. J. Waxer, V. Bagnoud, I. A. Begishev, M. J. Guardalben, J. Puth, and J. D. Zuegel, “High-conversion-efficiency optical parametric chirped-pulse amplification system using spatiotemporally shaped pump pulses,” *Optics Letters* **28**(14), 1245–1247 (2003).
- [93] J. A. Fülöp, Z. Major, B. Horváth, F. Tavella, A. Baltuška, and F. Krausz, “Shaping of picosecond pulses for pumping optical parametric amplification,” *Appl. Phys. B* **87**(1), 79–84 (2006).
- [94] M. Siebold, M. Hornung, R. Boedefeld, S. Podleska, S. Klingebiel, C. Wandt, F. Krausz, S. Karsch, R. Uecker, A. Jochmann, J. Hein, and M. C. Kaluza, “Terawatt diode-pumped Yb:CaF₂ laser,” *Optics Letters* **33**(23), 2770–2772 (2008).

- [95] F. Verluise, V. Laude, Z. Cheng, C. Spielmann, and P. Tournois, “Amplitude and phase control of ultrashort pulses by use of an acousto-optic programmable dispersive filter: pulse compression and shaping,” *Optics Letters* **25**(8), 575 (2000).
- [96] S. Bonora, D. Brida, P. Villoresi, and G. Cerullo, “Ultrabroadband pulse shaping with a push-pull deformable mirror,” *Optics Express* **18**(22), 23,147–23,152 (2010).
- [97] K. Osvay and I. N. Ross, “Broadband sum-frequency generation by chirp-assisted group-velocity matching,” *Journal of the Optical Society of America B* **13**(7), 1431–1438 (1996).
- [98] M. Bradler, P. Baum, and E. Riedle, “Femtosecond continuum generation in bulk laser host materials with sub- μ J pump pulses,” *Appl. Phys. B* **97**(3), 561–574 (2009).
- [99] T. Kampfrath, K. Tanaka, and K. A. Nelson, “Resonant and nonresonant control over matter and light by intense terahertz transients,” *Nature Photonics* **7**(9), 680–690 (2013).
- [100] C. Vicario, C. Ruchert, F. Ardana-Lamas, P. M. Derlet, B. Tudu, J. Luning, and C. P. Hauri, “Off-resonant magnetization dynamics phase-locked to an intense phase-stable terahertz transient,” *Nature Photonics* **7**(9), 720–723 (2013).
- [101] M. Tonouchi, “Cutting-edge terahertz technology,” *Nat. Phot.* **1**, 97–105 (2007).
- [102] A. Houard, Y. Liu, B. Prade, and A. Mysyrowicz, “Polarization analysis of terahertz radiation generated by four-wave mixing in air,” *Opt. Lett.* **33**(11), 1195–1197 (2008).
- [103] M. Kress, T. Löffler, M. Thomson, R. Dorner, H. Gimpel, K. Zrost, T. Ergler, R. Moshhammer, U. Morgner, J. Ullrich, and H. Roskos, “Determination of the carrier-envelope phase of few-cycle laser pulses with terahertz-emission spectroscopy,” *Nature Physics* **2**(5), 327–331 (2006).
- [104] I. Babushkin, S. Skupin, A. Husakou, C. Köhler, E. Cabrera-Granado, L. Bergé, and J. Herrmann, “Tailoring terahertz radiation by controlling tunnel photoionization events in gases,” *New J. Phys.* **13**(12), 123,029 (2011).
- [105] M. D. Thomson, V. Blank, and H. G. Roskos, “Terahertz white-light pulses from an air plasma photo-induced by incommensurate two-color optical fields,” *Optics Express* **18**(22), 23,173–23,182 (2010).
- [106] N. V. Vvedenskii, A. I. Korytin, V. A. Kostin, A. A. Murzanev, A. A. Silaev, and A. N. Stepanov, “Two-Color Laser-Plasma Generation of Terahertz Radiation Using a Frequency-Tunable Half Harmonic of a Femtosecond Pulse,” *Physical Review Letters* **112**(5), 055,004 (2014).
- [107] M. Clerici, M. Peccianti, B. E. Schmidt, L. Caspani, M. Shalaby, M. Giguère, A. Lotti, A. Couairon, F. Légaré, T. Ozaki, D. Faccio, and R. Morandotti, “Wavelength Scaling of Terahertz Generation by Gas Ionization,” *Physical Review Letters* **110**(25), 253,901 (2013).
- [108] O. Smirnova, M. Spanner, and M. Ivanov, “Analytical solutions for strong field-driven atomic and molecular one- and two-electron continua and applications to strong-field problems,” *Phys. Rev. A* **77**(3), 033,407 (2008).
- [109] P. Russell, “Photonic Crystal Fibers,” *Science* **299**(5605), 358–362 (2003).

- [110] M. Nisoli, S. D. Silvestri, O. Svelto, R. Szipöcs, K. Ferencz, C. Spielmann, S. Sartania, and F. Krausz, “Compression of high-energy laser pulses below 5 fs,” *Optics Letters* **22**(8), 522–524 (1997).
- [111] R. Cregan, B. Mangan, J. Knight, T. Birks, P. S. J. Russell, P. Roberts, and D. Allan, “Single-mode photonic band gap guidance of light in air,” *Science* **285**(5433), 1537–1539 (1999).
- [112] Y. Y. Wang, N. V. Wheeler, F. Couny, P. J. Roberts, and F. Benabid, “Low loss broadband transmission in hypocycloid-core Kagome hollow-core photonic crystal fiber,” *Optics Letters* **36**(5), 669–671 (2011).
- [113] Y. Y. Wang, X. Peng, M. Alharbi, C. F. Duttin, T. D. Bradley, F. Gérôme, M. Mielke, T. Booth, and F. Benabid, “Design and fabrication of hollow-core photonic crystal fibers for high-power ultrashort pulse transportation and pulse compression,” *Opt Lett* **37**(15), 3111–3 (2012).
- [114] O. Heckl, C. Saraceno, C. Baer, T. Südmeyer, Y. Wang, Y. Cheng, F. Benabid, and U. Keller, “Temporal pulse compression in a xenon-filled Kagome-type hollow-core photonic crystal fiber at high average power,” *Optics Express* **19**(20), 19,142–19,149 (2011).
- [115] J. Travers, W. Chang, J. Nold, N. Joly, and P. Russell, “Ultrafast nonlinear optics in gas-filled hollow-core photonic crystal fibers [Invited],” *J. Opt. Soc. Am. B* **28**(12), A11–A26 (2011).
- [116] T. Balčiūnas, C. Fourcade-Duttin, G. Fan, T. Witting, A. Voronin, A. Zheltikov, F. Gerome, G. Paulus, A. Baltuška, and F. Benabid, “A strong-field driver in the single-cycle regime based on self-compression in a kagome fibre,” *Nature communications* **6**, 6117 (2015).
- [117] D. G. Ouzounov, F. R. Ahmad, D. Muller, N. Venkataraman, M. T. Gallagher, M. G. Thomas, J. Silcox, K. W. Koch, and A. L. Gaeta, “Generation of Megawatt Optical Solitons in Hollow-Core Photonic Band-Gap Fibers,” *Science* **301**(5640), 1702–1704 (2003).
- [118] L. F. Mollenauer, R. H. Stolen, and J. P. Gordon, “Experimental Observation of Picosecond Pulse Narrowing and Solitons in Optical Fibers,” *Physical Review Letters* **45**(13), 1095–1098 (1980).
- [119] A. A. Amorim, M. V. Tognetti, P. Oliveira, J. L. Silva, L. M. Bernardo, F. X. Kärtner, and H. M. Crespo, “Sub-two-cycle pulses by soliton self-compression in highly nonlinear photonic crystal fibers,” *Optics Letters* **34**(24), 3851–3853 (2009).
- [120] P. Colman, C. Husko, S. Combrie, I. Sagnes, C. W. Wong, and A. De Rossi, “Temporal solitons and pulse compression in photonic crystal waveguides,” *Nature Photonics* **4**(12) (2010).
- [121] C. M. Smith, N. Venkataraman, M. T. Gallagher, D. Müller, J. A. West, N. F. Borrelli, D. C. Allan, and K. W. Koch, “Low-loss hollow-core silica/air photonic bandgap fibre,” *Nature* **424**(6949), 657–9 (2003).
- [122] F. Couny, F. Benabid, P. J. Roberts, P. S. Light, and M. G. Raymer, “Generation and photonic guidance of multi-octave optical-frequency combs,” *Science* **318**(5853), 1118–21 (2007).

-
- [123] F. Benabid, J. C. Knight, G. Antonopoulos, and P. S. J. Russell, “Stimulated Raman scattering in hydrogen-filled hollow-core photonic crystal fiber,” *Science* **298**(5592), 399–402 (2002).
- [124] P. Hölzer, W. Chang, J. C. Travers, A. Nazarkin, J. Nold, N. Y. Joly, M. F. Saleh, F. Biancalana, and P. S. J. Russell, “Femtosecond nonlinear fiber optics in the ionization regime,” *Phys Rev Lett* **107**(20), 203,901 (2011).
- [125] A. Nazarkin and G. Korn, “Pulse Self-Compression in the Subcarrier Cycle Regime,” *Physical Review Letters* **83**(23), 4748–4751 (1999).
- [126] A. Voronin and A. Zheltikov, “Soliton-number analysis of soliton-effect pulse compression to single-cycle pulse widths,” *Physical Review A* **78**(6), 063,834 (2008).
- [127] T. Witting, F. Frank, C. A. Arrell, W. A. Okell, J. P. Marangos, and J. W. Tisch, “Characterization of high-intensity sub-4-fs laser pulses using spatially encoded spectral shearing interferometry,” *Optics Letters* **36**(9), 1680–1682 (2011).
- [128] M. Bellini and T. W. Hänsch, “Phase-locked white-light continuum pulses: toward a universal optical frequency-comb synthesizer,” *Optics Letters* **25**(14), 1049–1051 (2000).
- [129] O. D. Mücke, D. Sidorov, P. Dombi, A. Pugžlys, A. Baltuška, S. Ališauskas, V. Smilgevičius, J. Pocius, L. Giniūnas, R. Danielius, and N. Forget, “Scalable Yb-MOPA-driven carrier-envelope phase-stable few-cycle parametric amplifier at 1.5 μm ,” *Optics Letters* **34**(2), 118–120 (2009).
- [130] T. Fuji, N. Ishii, C. Y. Teisset, X. Gu, T. Metzger, A. Baltuska, N. Forget, D. Kaplan, A. Galvanauskas, and F. Krausz, “Parametric amplification of few-cycle carrier-envelope phase-stable pulses at 2.1 μm ,” *Opt. Lett.* **31**(8), 1103–1105 (2006).
- [131] A. Couairon and A. Mysyrowicz, “Femtosecond filamentation in transparent media,” *Physics Reports* **441**(2-4), 47 – 189 (2007).
- [132] C. A. Haworth, L. E. Chipperfield, J. S. Robinson, P. L. Knight, J. P. Marangos, and J. W. G. Tisch, “Half-cycle cutoffs in harmonic spectra and robust carrier-envelope phase retrieval,” *Nature Physics* **3**(1), 52–57 (2006).
- [133] B. Debord, M. Alharbi, L. Vincetti, A. Husakou, C. Fourcade-Dutin, C. Hönniger, E. Mottay, F. Gérôme, and F. Benabid, “Multi-meter fiber-delivery and pulse self-compression of milli-Joule femtosecond laser and fiber-aided laser-micromachining,” *Optics Express* **22**(9), 10,735–10,746 (2014).
- [134] L. Bergé, S. Skupin, and G. Steinmeyer, “Temporal self-restoration of compressed optical filaments,” *Physical review letters* **101**(21), 213,901 (2008).
- [135] O. D. Mücke, S. Ališauskas, A. J. Verhoef, A. Pugžlys, A. Baltuška, V. Smilgevičius, J. Pocius, L. Giniūnas, R. Danielius, and N. Forget, “Self-compression of millijoule 1.5 μm pulses,” *Optics Letters* **34**(16), 2498–2500 (2009).
- [136] M. Nurhuda, A. Suda, K. Midorikawa, M. Hatayama, and K. Nagasaka, “Propagation dynamics of femtosecond laser pulses in a hollow fiber filled with argon: constant gas pressure versus differential gas pressure,” *JOSA B* **20**(9), 2002–2011 (2003).
- [137] B. E. Schmidt, A. D. Shiner, P. Lassonde, J.-C. Kieffer, P. B. Corkum, D. M. Villeneuve, and F. Légaré, “CEP stable 1.6 cycle laser pulses at 1.8 μm ,” *Optics Express* **19**(7), 6858–6864 (2011).

-
- [138] D. Steingrube, E. Schulz, T. Binhammer, M. Gaarde, A. Couairon, U. Morgner, and M. Kovačev, “High-order harmonic generation directly from a filament,” *New Journal of Physics* **13**(4), 043,022 (2011).